OCS Study
BOEM 2018-018

Development of a Very High-Resolution Regional Circulation Model of Beaufort Sea Nearshore Areas

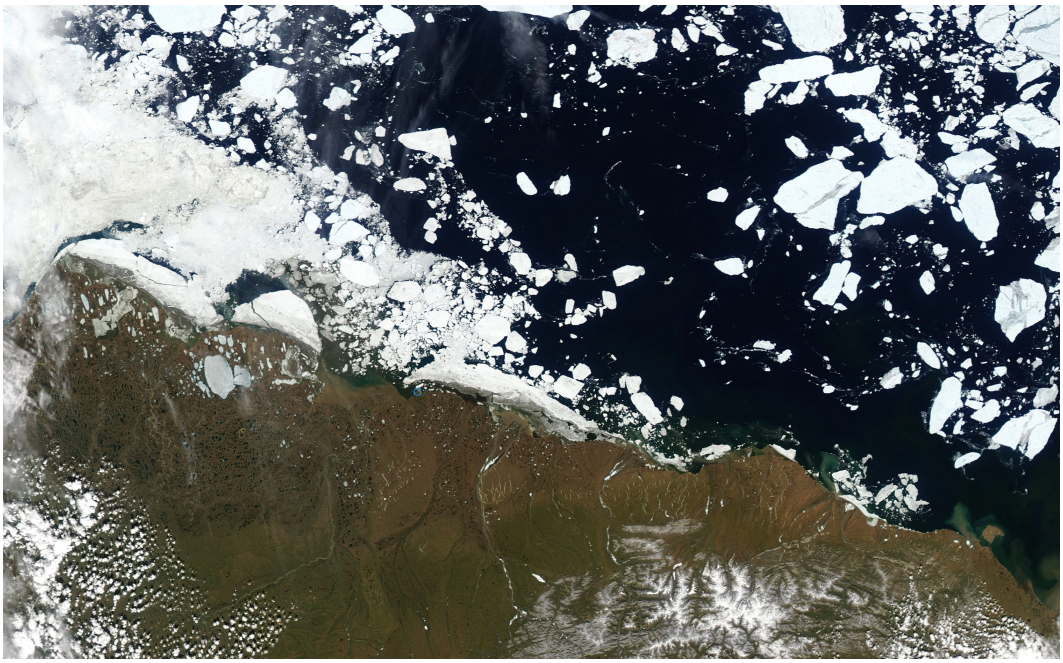

U.S. Department of the Interior
Bureau of Ocean Energy Management
Headquarters, Sterling, VA
www.boem.gov

Development of a Very High-Resolution Regional Circulation Model of Beaufort Sea Nearshore Areas

Enrique N. Curchitser, Rutgers University, New Brunswick, NJ
Kate Hedstrom, University of Alaska, Fairbanks, AK
Seth Danielson, University of Alaska, Fairbanks, AK
Jeremy Kasper, University of Alaska, Fairbanks, AK

Prepared under BOEM Cooperative Agreement M15AC00011
by
Rutgers University
14 College Farm Road
New Brunswick, NJ 08901

Published by
U.S. Department of the Interior
Bureau of Ocean Energy Management
Headquarters, Environmental Studies Program
Sterling, VA
May, 2018

DISCLAIMER

REPORT AVAILABILITY

To download a PDF file of this Environmental Studies Program report, go to the U.S. Department of the Interior, Bureau of Ocean Energy Management, Environmental Studies Program Information System website (https://www.boem.gov/espis/) and search on OCS Study BOEM 2018-018. Or contact the BOEM Alaska OCS Region office at the address listed below.

Bureau of Ocean Energy Management
Environmental Sciences Management Section
3801 Centerpoint Drive, Suite 500
Anchorage, AK 99503
Phone: (907) 334-5200
Email: alaska.studies@boem.gov

l

CITATION

Curchitser, E.N., K. Hedstrom, S. Danielson and J. Kasper. 2017. Development of a Very High-Resolution Regional Circulation Model of Beaufort Sea Nearshore Areas. U.S. Dept. of the Interior, Bureau of Ocean Energy Management, Alaska OCS Region, Anchorage, AK. OCS Study BOEM 2018-018. 81 pp.

About the cover: Beaufort Shelf on June 23, 2016. LANCE-MODIS image from https://lance-modis.eosdis.nasa.gov/imagery/subsets/?area=global. We acknowledge the use of Rapid Response imagery from the Land, Atmosphere Near real-time Capability for EOS (LANCE) system operated by the NASA/GSFC/Earth Science Data and Information System (ESDIS) with funding provided by NASA/HQ.

Abstract

This document is the final report for the U.S. Department of the Interior, Bureau of Ocean Energy Management (BOEM) Cooperative Agreement M15AC00011, Development of a Very High-Resolution Regional Circulation Model of Beaufort Sea Nearshore Areas. The primary aim of the work done under this award was to use a state-of-the-science coupled circulation sea ice numerical ocean model to simulate at least a decade of the currents sea ice and winds in the Beaufort Seas nearshore areas, which can be used as inputs to oil-spill models. This document reviews the basic oceanography of the region of interest, describes the relevant details of the circulation and ice models and their implementation for this particular problem, and describes the numerical model-data comparisons that have been performed as part of this current award.

Contents

List of Figures

List of Tables

Acronyms and abbreviations

ARDAT	Arctic River Discharge and Temperature data set
BOEM	Bureau of Ocean Energy Management
CICE	Community Ice Model
COOPS	Center for Operational Oceanographic Products and Services
EVP	Elastic Viscous Plastic [a rheology]
GLORYS	Global Ocean Reanalysis
GLS	Generic Length Scale
HYCOM	Hybrid Coordinate Ocean Model
KE	Kinetic Energy
MEKE	Mean Eddy Kinetic Energy
MERRA	Modern Era Reanalysis
MKE	Mean Kinetic Energy
MKS	Meter, Kilogram, Second
MPI	Message Passing Interface
NetCDF	Network Common Data Format
NOAA	National Oceanographic and Atmospheric Administration
NSIDC	National Snow and Ice Data Center
PA	Principal Axis
RCM	Rotary Current Meter
RMSE	Root Mean Square Error
ROMS	Regional Ocean Modeling System
S	Salinity
SSH	Sea Surface Height
SODA	Simple Ocean Data Assimilation
SSM/I	Special Sensor Microwave/Imager
STD	Standard Deviation
Sv	Sverdrup ($10^6 m^3/s$)
T	Temperature
°T	degrees True. Degrees clockwise from due North
UAF	University of Alaska Fairbanks
UW	University of Washington
U	Zonal velocity
Ur	Along-shelf velocity; aligns with the principal axis of variation
V	Meridional velocity
Vr	Cross-shelf velocity; orthogonal to the principal axis of variation
θ	Principal axis orientation

1 Introduction

1.1 Background: The Beaufort Sea

Beaufort Sea Oceanography

The Alaskan Beaufort Sea shelf (Figure 1) extends approximately 500 km eastward from Point Barrow to the Canadian border, abutting the Mackenzie. The shelf width is approximately 80 km as measured from the coast to the 200 m isobath. Shelf depths grade smoothly offshore with bottom slopes typically being about 10^{-3} inshore of the 100 m isobath. Sea ice can cover the shelf year-round, although more typically the inner shelf (and in recent years the entire shelf) is ice-free during the summer months. Landfast ice begins to form in October and extends 20-40 km offshore through mid-June so that it covers nearly 25% of the shelf area (Barnes et al. [1984]) through most of the year although lockup events can extend far past the shelf break for as long as ten or twenty days (Mahoney et al. [2014]). The duration of the landfast ice season has decreased in the Beaufort Sea by up to two months since the 1970s (Mahoney et al. [2014]). The landfast ice is relatively smooth adjacent to the coast, but is increasingly deformed offshore. Currents under the landfast ice are small and uncorrelated with the local winds whereas currents in the presence of freely drifting ice during breakup and open water (summer-fall months) are highly coherent with the winds (Weingartner et al. [2009, 2017]).

The Beaufort's oceanic circulation and ice deformation are related to the seasonally varying winds. These we summarized in the form of monthly statistics using the archived National Weather Service wind record in Barrow from 1949–2005. The alongshore component of the winds accounts for most of the variance in the winds and are primarily responsible for forcing shelf circulations. In general, winds blowing from the northeast prevail throughout the year. On a monthly basis the majority of the alongshore winds are westward (upwelling favorable) and westward winds are, on average, stronger than eastward (downwelling-favorable) winds. There are, however, substantial seasonal differences. Westward winds are strongest in late fall and early winter and occur most frequently in October, November, and March. Westward winds are only slightly more frequent than eastward winds in July and August, although westward winds are stronger in these months. Thus, on average, upwelling favorable conditions prevail throughout the year. Although the alongshelf wind stress component is important in the ocean circulation, the north-south component plays an important role in ice dynamics. In particular, winter winds are primarily onshore (southward) and thus force pack ice onshore and deform the landfast ice edge. Less frequent offshore winds can result in detachment of the landfast ice (breakouts). These seasonal variations are primarily related to the deep high pressure cell centered over the Arctic Ocean in winter. However, the high pressure system weakens in summer and fall, when low-pressure systems invade the Beaufort Sea from the North Pacific (Maslanik et al. [1999]).

Seasonally varying mesoscale winds may substantially alter the synoptic wind field in the nearshore zone. For example, a persistent summer sea breeze results in mean westward

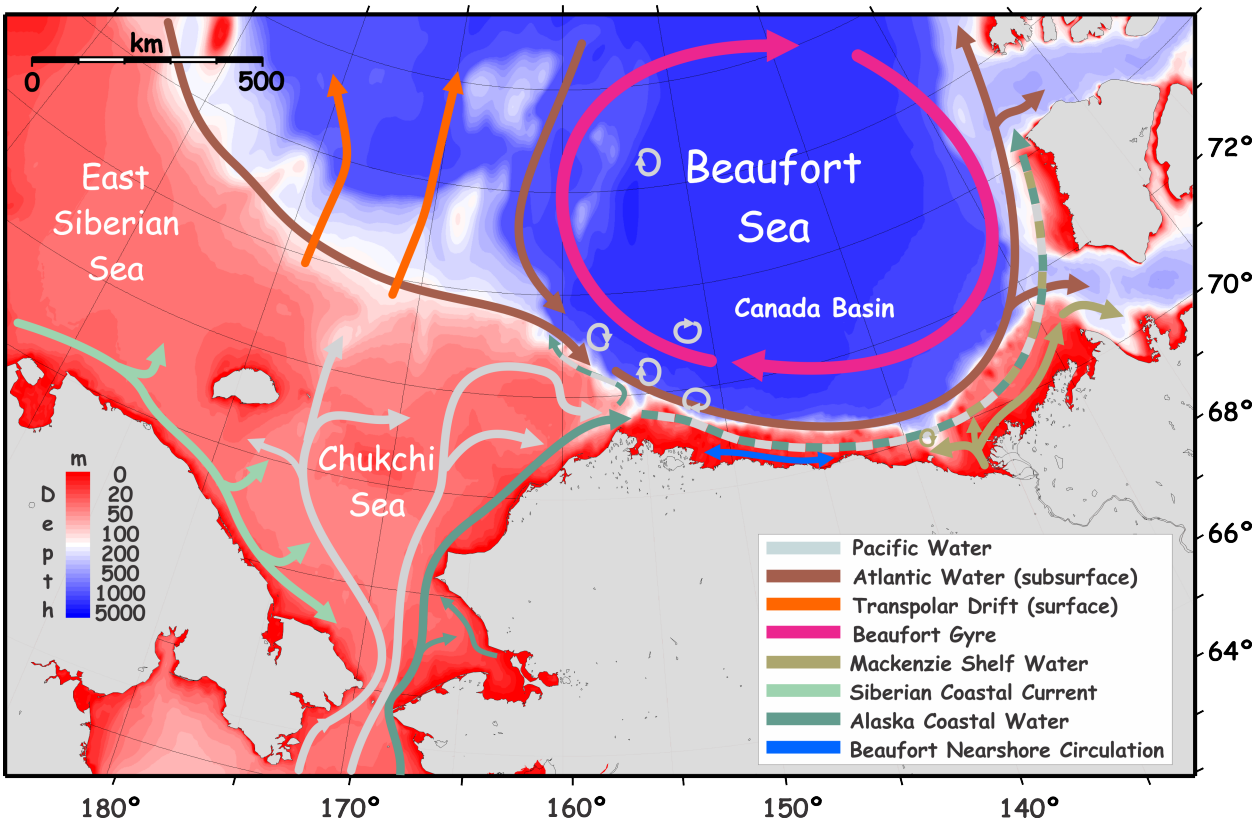

Figure 1: Idealized schematic of the circulation in the Chukchi and Beaufort seas. Nominal flow pathways are colored based on water properties, origin and/or function.

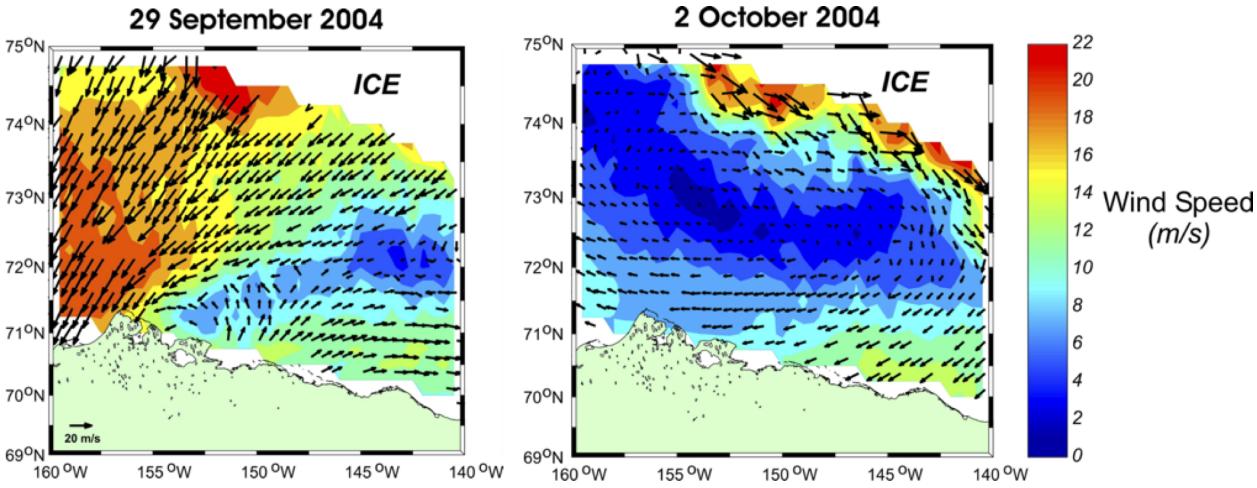

Figure 2: Wind speed and directions as measured by the QuickScat satellite on 29 September (left) and 2 October (right) 2004. The images show mesoscale wind field shears and divergences that can affect the ocean circulation.

winds within 25 km of the coast (Kozo [1982a,b]). Small-scale structure in the wind field can be discerned from satellite-derived winds (Figure 2). During the landfast ice period from October through April mountain barrier baroclinicity (Kozo [1980, 1984]) can produce along-shore divergence in the wind field. This effect occurs when the southward flow of low-level cold air from the Arctic Ocean is blocked along the northern flank of the Brooks Range. The resulting isopycnal slopes induce eastward surface winds of about 15 m/s over a horizontal width scale of 200–300 km. The western Beaufort coast is rarely influenced by the mountain barrier effect because it lies more than 300 km north of the Brooks Range, but the eastern Beaufort coast lies within 60 km of the mountains. Consequently, winds can be westward over the western Beaufort coast but eastward along the eastern coast. Kozo [1984] estimated that the mountain barrier baroclinicity effect occurs approximately 20% of the time during winter.

Three distinct oceanic regimes bound the Alaskan Beaufort Sea. To the west, variability in Barrow Canyon outflow is large, especially in fall and winter, and mainly due to fluctuations in the regional winds (Weingartner et al. [1998]; Weingartner et al. [2005]; Woodgate et al. [2005]). Some of the Barrow Canyon outflow continues eastward as a subsurface current (or slope undercurrent) along the Beaufort shelfbreak and slope where it forms the upper halocline waters of the Canada Basin (Mountain et al. [1976]; Aagaard [1984]; Pickart [2004]; Pickart et al. [2005]; Nikolopoulos et al. [2009]). Under weak westward winds or eastward winds some of the water exiting Barrow Canyon rounds Pt. Barrow and continues onto the inner portion of the western Beaufort shelf (Okkonen, pers. comm.).

The outer shelf and continental slope provide the offshore boundary for the Alaskan Beaufort Sea. In the upper 50 m or so the flow is westward and part of the southern limb of the wind-driven Beaufort Gyre. This flow can occasionally be reversed by strong eastward winds and/or by occasional shelfbreak upwelling that advects eastward momentum from the

slope undercurrent onto the shelf at least as far inshore as the 50 m isobath (Aagaard [1984]; Pickart [2004]; Nikolopoulos et al. [2009]).

The Mackenzie shelf joins the Alaskan Beaufort shelf to the east and likely the year-round discharge from the Mackenzie River influences the eastern Beaufort shelf (Carmack et al. [1989]; Macdonald et al. [1989]; Macdonald and Carmack [1991]). Mackenzie shelf water has been detected throughout much of the Canada basin, including the continental slope of the Chukchi and western Beaufort Sea as far as 160W longitude (Guay and Falkner [1998]; Macdonald et al. [1999]). Conceivably, wind-driven currents transport Mackenzie shelf waters onto the Alaskan Beaufort shelf as well; observations of satellite imagery suggest that the summer melt in the Alaskan Beaufort is strongly dependent upon the Mackenzie River plume (Weingartner et al. [2009]). In addition to the Mackenzie River, a large number of smaller rivers discharge into the Alaskan Beaufort Sea. These are asymmetrically distributed with most of them discharging into the central and eastern portions of the shelf.

2 Scientific and technical approaches

In this section, we describe the modeling framework, its components, and the details of the specific model implementations for this project, forcing, boundary conditions, and the various model integrations performed. Further details on the numerics of coupled circulation-sea ice model are given in the manual provided as part of this project (Hedstrom [2018]).

2.1 The coupled ocean-sea ice model

The main research tool used for this work is a state-of-the-science coupled ocean/sea ice model based on the Regional Ocean Modeling System (ROMS) (Shchepetkin and McWilliams [2005]). ROMS is a free-surface, hydrostatic primitive equation ocean circulation model whose core was developed at Rutgers University and University of California, Los Angeles with significant contributions from a large community of users. ROMS is a terrain-following, finite volume (Arakawa C-grid) model with the following advanced features: extensive restructuring for sustained performance on multi-processor computing platforms (using MPI); high-order, weakly dissipative algorithms for tracer advection; a unified treatment of surface and bottom boundary layers (e.g., K-Profile Parameterization; Large et al. [1994]), atmosphere-ocean flux computations based on the ocean model prognostic variables using bulk-formulae (Fairall et al. [2003] or Large and Yeager [2009]) and an integrated set of procedures for data assimilation (e.g., optimal interpolation and adjoint-based methods; Moore et al. [2004]). ROMS also has an integrated float tracking capability. The vertical discretization is based on a terrain-following coordinate system with the ability to increase the resolution near the surface and bottom boundary layers.

ROMS has been coupled to a sea-ice model (Budgell [2005]) consisting of the elastic-

viscous-plastic (EVP) rheology (Hunke and Dukowicz [1997], Hunke [2001]) and the Mellor and Kantha [1989] thermodynamics. It is fully explicit and implemented on the ROMS Arakawa C-grid and is therefore fully parallel using MPI, just as ROMS is. The sea ice model also includes frazil ice growth in the ocean being passed to the ice (Steele et al. [1989]). It currently follows a single thermodynamic ice category, which exhibits accurate results in a marginal ice zone such as the Bering Sea (Danielson et al. [2011]).

The principal attributes of the ocean and sea ice models are:

1. General
   (a) Primitive equations with potential temperature, salinity, and an equation of state.
   (b) Hydrostatic and Boussinesq approximations.
   (c) Optional third-order upwind advection scheme.
   (d) Optional Smolarkiewicz advection scheme for tracers (potential temperature, salinity, etc.).
   (e) Optional Lagrangian floats.
   (f) Option for point sources and sinks.
2. Horizontal
   (a) Orthogonal-curvilinear coordinates.
   (b) Arakawa C grid.
   (c) Choice of closed, periodic, prescribed, radiation, and gradient open boundary conditions.
   (d) Masking of land areas.
3. Vertical
   (a) sigma (terrain-following) coordinate.
   (b) Free surface.
   (c) Tridiagonal solver with implicit treatment of vertical viscosity and diffusivity.
4. Ice
   (a) Hunke and Dukowicz elastic-viscous-plastic dynamics.
   (b) Mellor-Kantha thermodynamics.
   (c) Orthogonal-curvilinear coordinates.
   (d) Arakawa C grid.
   (e) Smolarkiewicz advection of tracers.
   (f) Lemieux landfast ice parameterization.

5. Mixing options
   (a) Horizontal Laplacian and biharmonic diffusion along constant s, z or density surfaces.
   (b) Horizontal Laplacian and biharmonic viscosity along constant s or z surfaces.
   (c) Optional Smagorinsky horizontal viscosity and diffusion (but not recommended for diffusion).
   (d) Horizontal free-slip or no-slip boundaries.
   (e) Vertical harmonic viscosity and diffusion with a spatially variable coefficient, with options to compute the coefficients with Large et al. [1994], Mellor-Yamada, or generic length scale (GLS) mixing schemes.
6. Implementation
   (a) Dimensional in meter, kilogram, second (MKS) units.
   (b) Fortran 90.
   (c) Runs under UNIX, requires the C preprocessor, gnu make, and Perl.
   (d) All input and output is done in NetCDF (Network Common Data Format), requires the NetCDF library.
   (e) Options include serial, parallel with MPI, and parallel with OpenMP.

The above list, describing the dynamical core, hasn't evolved significantly over the fifteen years since the early development of ROMS. However, many of the numerical details have changed a great deal. Examples include consistent temporal averaging of the barotropic mode to guarantee both exact conservation and constancy preservation properties for tracers; redefined barotropic pressure-gradient terms to account for local variations in the density field; vertical interpolation performed using conservative parabolic splines; and higher-order, quasi-monotone advection algorithms. In addition, many capabilities have been added to the basic model including data assimilation (both 4DVar and Ensemble Kalman Filter), several biogeochemical models, and on- and off-line particle tracking.

Of particular importance to this project is a new implementation of landfast ice in the coupled ocean-sea ice model. The Arctic ocean has many shallow shelves, the Beaufort being one of them, on which landfast ice can form every winter. For this project, we implemented the parameterization described in Lemieux et al. [2015]. Basal stress terms τ_b are added to sea ice momentum equations representing a bottom drag applied to the deepest ice keels. Included is a parameterization of the ice thickness distribution so that even a single ice-category model can use the landfast ice option. Figure 3 shows a cartoon of an ice floe with a keel.

Exhaustive details of the landfast ice implementation, the coupled circulation/sea ice model, timestepping and parameterization scheme, boundary conditions and more are provided in the accompanying manual which is part of the deliverables for this cooperative agreement (Hedstrom [2018]).

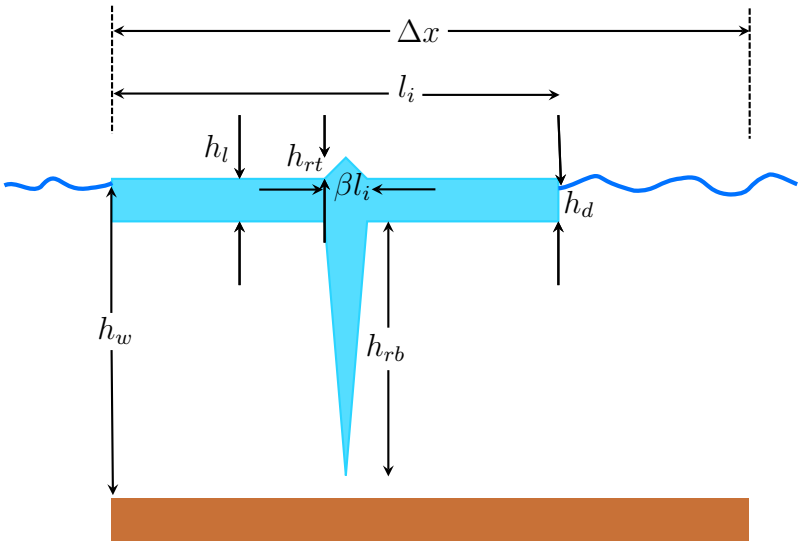

Figure 3: Cartoon of an ice floe with a deep keel. Variables are defined in table 2

Variable	Value	Description
h_w		water depth
h_{rt}		ridge height above level ice
h_{rb}		draft of keels below level ice bottom
h_d		draft of ice below sea surface
l_i		length of ice floe within grid cell
Δx		x-dimension of grid cell
β	O(0.01)	ridged fraction of floe
k_1	8.0	tunable parameter
k_2	15.0	tunable parameter
u_0	5.0×10^{-5}	small velocity
C_b	20	ice strength parameter

Table 2: Variables used in the landfast ice parameterization (see Fig. 3).

3 Model Implementation

One of the main challenges of this project was to be able to run a very high-resolution model of the Beaufort shelf for at least a decade. The main difficulty is in generating ocean-ice boundary conditions to drive the regional coastal domains. Indeed, few examples exist of this type of implementation. A full treatment of the limited-area boundary condition problem in ocean models is beyond the scope of this report. After significant experimentation, we settled on a three-domain nested solution. Our implementation begins with a moderate resolution Pan-Arctic domain, where no sea-ice traverses the boundaries. We then downscale

this solution to a Chukchi-Beaufort Sea higher resolution domain. Finally, this solution is further downscaled to a sub-kilometer resolution Beaufort shelf model. By closely controlling the downscaling of boundary information from the Pan-Arctic to the Beaufort domain, we were able to run the very high-resolution Beaufort model for the period of January 1999 to September 2015, exceeding the period required by the project. Some implementation details are common to the three domains.

3.1 Pan-Arctic Implementation

We developed a Pan-arctic domain that focuses the resolution down to roughly 6 km over the Chukchi and Beaufort seas and coarsens away from the region of interest. Figure 4 shows the bathymetry and the extent of this domain. The grid is non-uniform, having more resolution close to Alaska—a measure of grid spacing is shown in Figure 5. The bathymetry came from ETOPO1 with a cutoff of 10 m depth (the next generation Arctic runs will have a better bathymetry as well as wider passages through the Canadian Archipelago).

The overall model extent was determined after extensive testing of the coupled ocean-sea ice model. Though we have extensive experience with open boundary conditions for multi-decadal integrations of regional ocean models, the open sea ice boundaries proved to be challenging. The final configuration was chosen so as to minimize errors in both the circulation and the sea ice distributions in the region of interest, while allowing us to maintain high resolution there.

3.1.1 Atmospheric forcing

We are using the MERRA forcing [Rienecker et al., 2011] and computing the momentum, heat and salt fluxes from the atmospheric conditions and the each model's surface temperature. The turbulent fluxes are computed using bulk flux formulae. We have Python scripts for downloading MERRA so that the MERRA files can be used as is, on their native grid, then interpolated by ROMS internally to the domain at hand. Because of the mis-match in resolution between the MERRA and ROMS grids, we take particular care to only interpolate atmospheric values over the ocean to the ROMS grid. We achieve this with a careful pre-processing of the atmospheric fields before they are read by the ROMS code.

3.1.2 Fresh water fluxes

For fresh water input from land, we have the ARDAT fields for the Arctic ocean [Whitefield et al., 2015], which includes monthly river temperature. These are applied as point sources to include the effects of bringing in warm water into the Pan-Arctic model domain. For the rest of the domain, we are applying Dai et al. [2009] as the RUNOFF field.

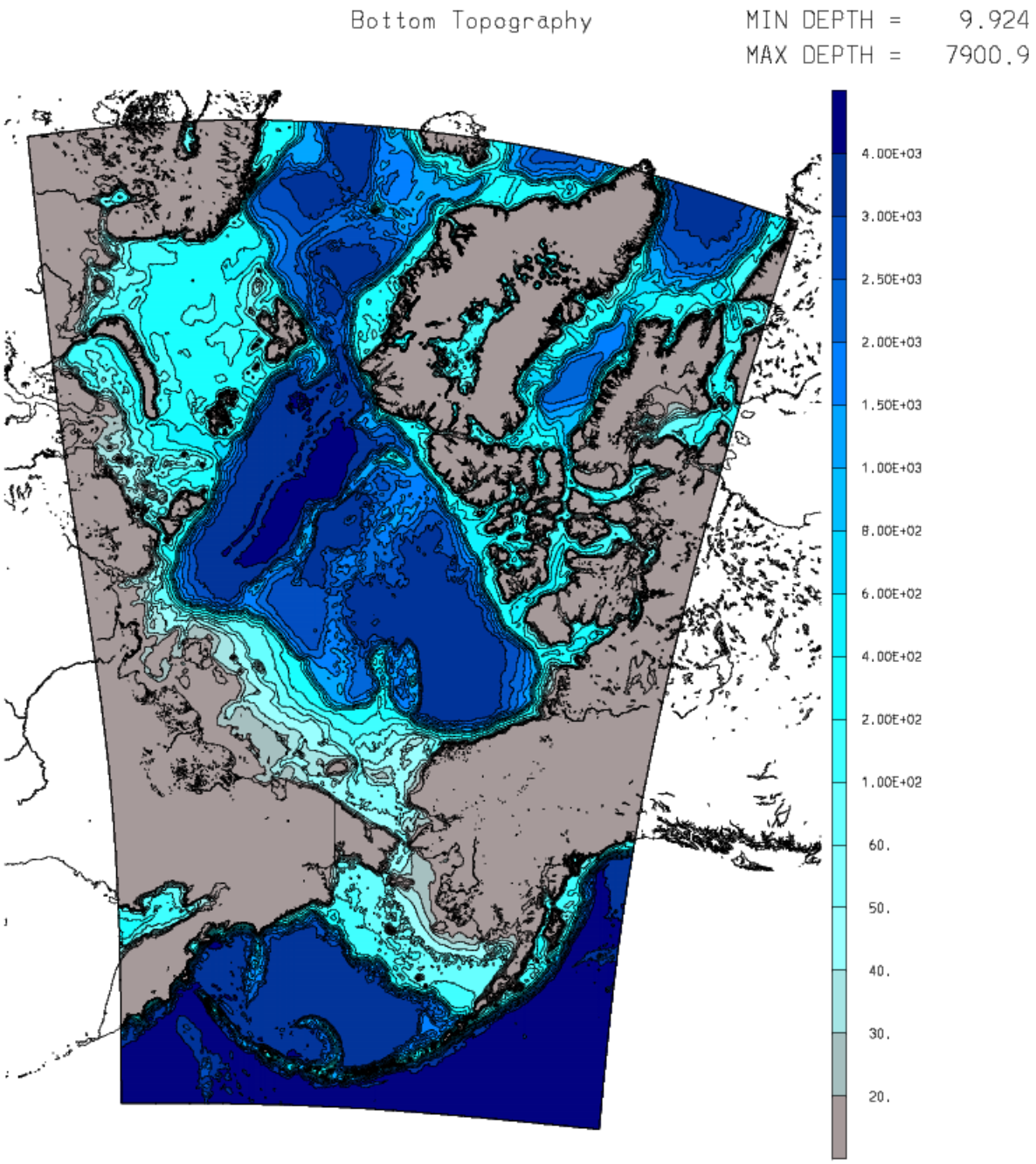

Figure 4: Bathymetry (meters) of the Pan-Arctic domain.

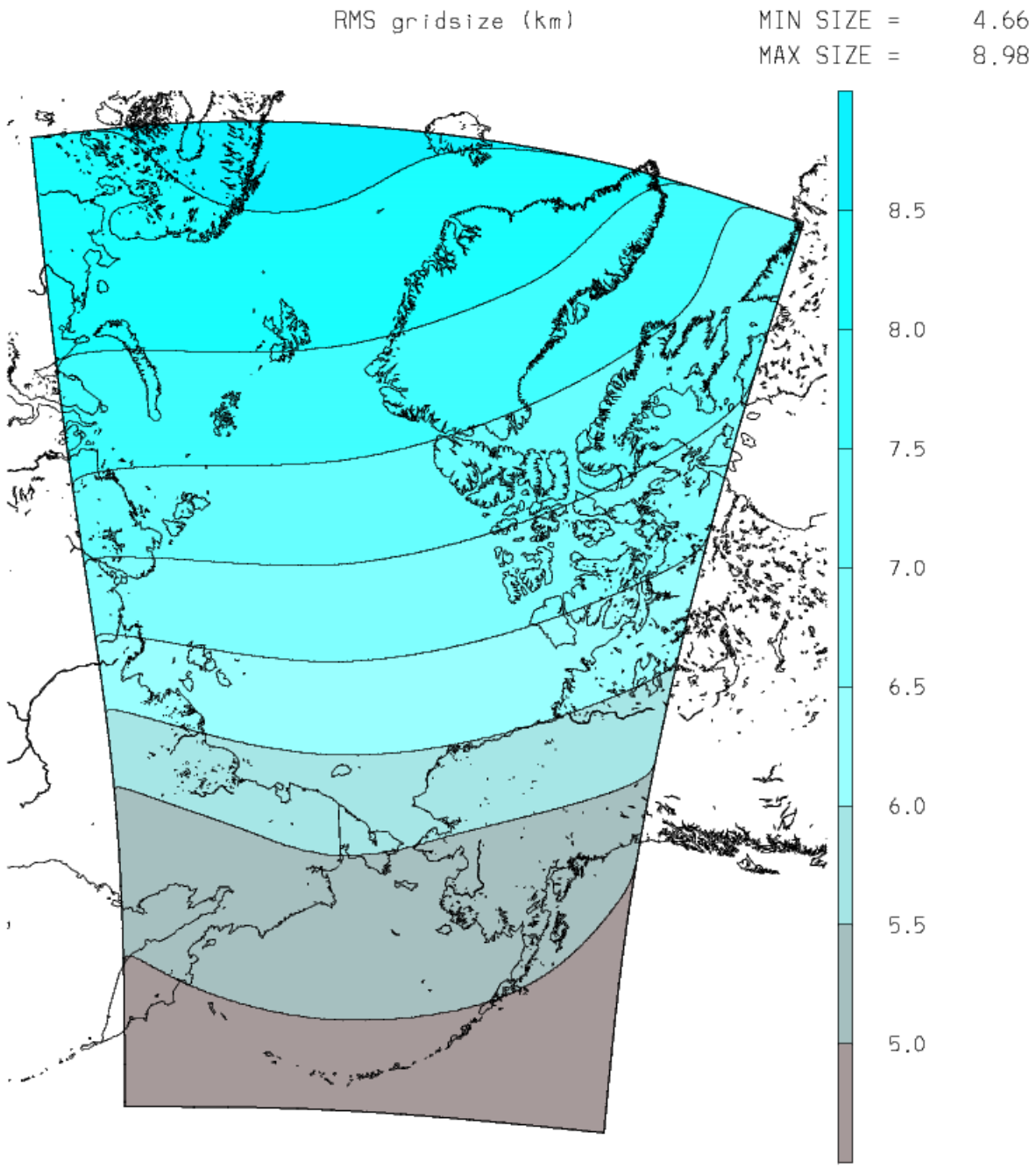

Figure 5: Grid spacing (km) of the Pan-Arctic domain.

3.1.3 Initial and boundary conditions

Initial and boundary conditions were derived from the Simple Ocean Data Assimilation (SODA), a reanalysis by Carton et al. [2005]. SODA fields are available through 2008. There are global HYCOM fields for the latter years. There are Python scripts to create initial, climatology and boundary conditions forcing fields from the SODA and HYCOM files. Ice initial thickness and concentration are extracted from a GLORYS simulation while the other initial ice conditions are set to uniform values where the SST is cold, zero otherwise. Ice boundary conditions are assumed to be not needed with the boundaries so far from the pack ice.

The side known as "South" is across the North Pacific ocean. The sides known as "East" and "West" are open on the Pacific sides, in the Gulf of Alaska and near Kamchatka, respectively. The northern Hudson Bay is masked out in this version. The last boundary is "North", on the Atlantic side. All use a combination of radiation and nudging as suggested by Marchesiello et al. [2001]. The nudging timescales are 3 days on inflow, 360 days on outflow, values we have found to be well-behaved in prior simulations. The idea is that on outflow, the boundary conditions should be dominated by a radiation condition, allowing signals to exit the domain. On inflow, the boundary conditions should be more strongly influenced by conditions from the global model.

3.1.4 Climatology

Other forcing includes a 360-day nudging to a monthly sea surface salinity climatology. There's an option to turn this off under the sea ice, which we have done.

Finally, there's a nudging to 2-d (for ice) and 3-d (for the ocean) climatology. This last comes from SODA/HYCOM for the ocean and includes interannual variability, but has been compiled monthly instead of more frequently as used by the boundary conditions. This nudging is applied in a band of 20 grid points around all open boundaries, ramping up from zero in the interior to a timescale of 30 days right on the boundary. The ice nudging is turned off in the Arctic, but was needed for the Beaufort domains, with an even shorter timescale, while the ocean nudging was not needed for the Beaufort domains.

3.1.5 Albedo

The default ice albedo is chosen based on the presence or absence of snow and on the surface temperature. Temperatures below -1° C are assumed to be dry while temperatures between -1° C and 0° C are a linear combination of the wet and dry albedoes shown in Table 3. The ocean albedo is assumed to depend on latitude θ as:

$$1.0 - [0.069 - 0.11\cos(2\theta)] \tag{1}$$

Table 3: Snow and ice albedo values.

Wet ice	0.60	Snow is absent, temperature is at 0.0 C
Dry ice	0.65	Snow is absent, temperature is below -1.0 C
Wet snow	0.72	Snow is present, temperature is at 0.0 C
Dry snow	0.85	Snow is present, temperature is below -1.0 C

3.1.6 Other model details

Tidal forcing is implemented through the boundaries using the eight dominant diurnal and semi-diurnal components derived from the Oregon State TOPEX/Poseidon Global Inverse Solution (TPXO) (Egbert and Erofeeva [2002]) (`http://www.coas.oregonstate.edu/research/po/research/tide/global.html`). For landfast ice, we use the parameterization from Lemieux et al. [2015].

Some choices are made via C preprocessor flags when compiling ROMS. These choices include masking, salinity, sea ice and the non-linear equation of state. We also use Laplacian viscosity on σ-surfaces, diffusion along constant z-surfaces and the full non-linear, curvilinear momentum equations. We are applying the tides, including the forcing provided by the tidal potential. The linear bottom drag coefficient varies spatially and is prescribed as a function of the water depth. The circulation model was unstable with the GLS vertical mixing scheme (Umlauf and Burchard [2003] and Warner et al. [2005]), so we switched back to the k-profile parameterization vertical mixing (Large et al. [1994]) which proved to be more well-behaved once a bug was fixed.

In the rest of this section, we describe the particular implementation of each of the model domains.

3.2 Beaufort shelf models

The Beaufort Sea domains are set up much like the Arctic, described above. We implemented two domains, a roughly 3 km curvilinear domain (Beaufort2), and a rectangular domain with uniform 0.5 km resolution over the coastal Beaufort (Beaufort3), as shown in Fig. 6–7.

The bathymetry is from the Alaska Regional Digital Elevation Model (ARDEM) version 2 [Danielson et al., 2016], which in the region of the Beaufort Sea is derived from the International Bathymetric Chart of the Arctic Ocean (IBCAO; Jakobsson et al. [2012]). The bathymetry was clipped to 3 m and 2 m depth for the two domains, respectively. The wetting and drying algorithm was turned on later for the small domain after an enclosed bay became unstable several years into the run.

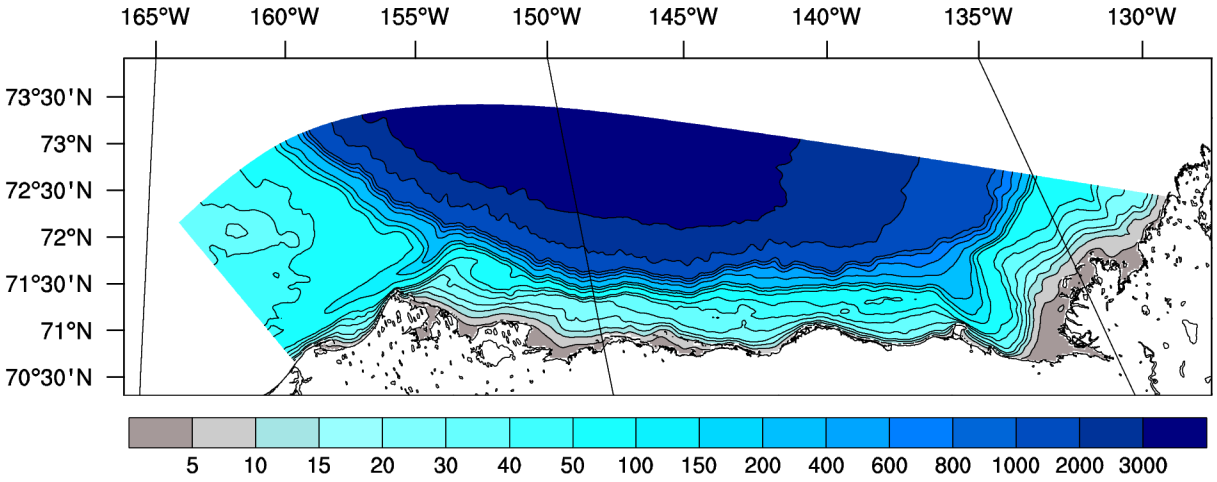

Figure 6: Bathymetry (meters) of the larger Beaufort Sea domain.

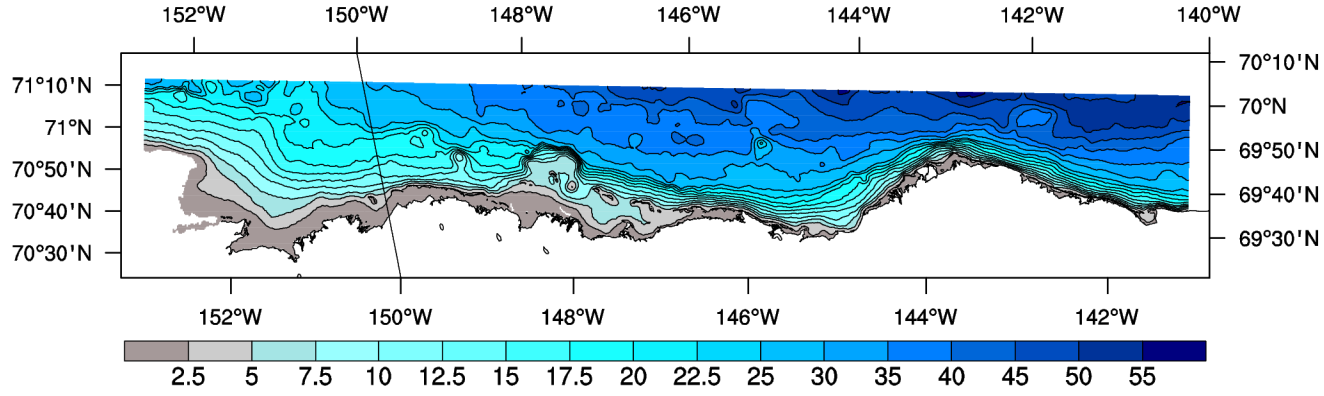

Figure 7: Bathymetry (meters) of the smaller Beaufort Sea domain.

3.3 The model runs

3.3.1 Pan-Arctic

The Pan-Arctic model simulation delivered to BOEM are:

- **PAN-ARCTIC**:
  - Pan-Arctic domain at 6–9 km resolution
  - Three-hourly Modern-Era Retrospective Analysis for Research and Applications (MERRA) atmospheric fields and radiation forcing
  - Boundary conditions and climatology from SODA and HYCOM
  - Albedo as described in §3.1.5
  - Years simulated: 1999–2015

3.3.2 Beaufort Shelf

The two simulations on the Beaufort shelf delivered to BOEM are:

- **BEAUFORT2**:
  - Chukchi-Beaufort domain at 3 km resolution.
  - Three-hourly Modern-Era Retrospective Analysis for Research and Applications (MERRA) atmospheric fields and radiation forcing
  - Ocean and ice boundary conditions and climatologies coming from the Pan-Arctic model simulation
  - Albedo as described in §3.1.5
  - Years simulated: 1999–2015
- **BEAUFORT3**:
  - Beaufort shelf domain at 0.5 km resolution.
  - Three-hourly Modern-Era Retrospective Analysis for Research and Applications (MERRA) atmospheric fields and radiation forcing.
  - Ocean and ice boundary conditions and climatologies coming from the BEAUFORT2 model simulation
  - Albedo as described in §3.1.5
  - Years simulated: 1999–2015

4 Model Evaluation

4.1 The data

4.1.1 Background

Publicly available in situ and remotely sensed datasets comprise the basis for model evaluation and validation. The moored records come from the University of Alaska Fairbanks (UAF) and University of Washington (UW) field campaigns during 1999-2006 in the Beaufort Sea and Bering Strait (Figure 8). These data are described in agency reports (see http://psc.apl.washington.edu/HLD/Bstrait/bstrait.html and http://www.ims.uaf.edu/beaufort/) and peer review publications including (Weingartner et al. [2017]; Woodgate [2017]).

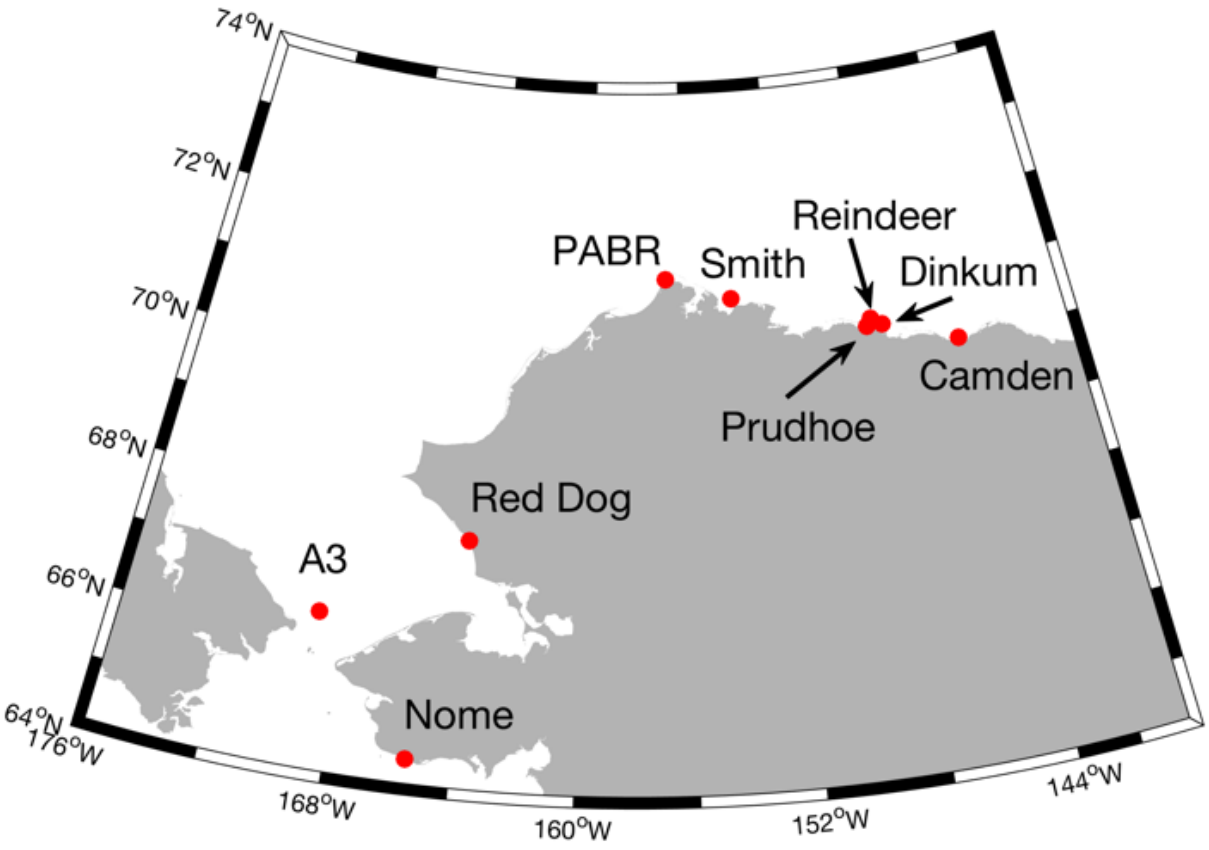

Figure 8: Tide gauges, current meter and temperature/salinity time series mooring sites selected for comparisons. Description of corresponding data is given in table 4.

Tide gauge data from Nome, the dock at Red Dog mine and Prudhoe Bay were downloaded from the National Oceanographic and Atmospheric Administration's (NOAA's) Cen-

Station Name	Station Type	Latitude (°N)	Longitude (°W)	Date Range
A3	Oceanographic Mooring	66.33	168.95	01/2005–12/2006
Camden	Oceanographic Mooring	70.03	144.94	09/2004–10/2006
Dinkum	Oceanographic Mooring	70.41	147.89	09/2004–10/2006
Reindeer	Oceanographic Mooring	70.51	148.32	08/2005–08/2006
Smith	Oceanographic Mooring	70.99	154.03	08/2004–17/2005
Prudhoe	Tide Gauge	70.41	148.53	10/2004–11/2004
Red Dog	Tide Gauge	67.58	164.06	10/2004–11/2004
Nome	Tide Gauge	64.49	165.44	10/2004–11/2004
PABR	Airport Weather Station	71.28	156.77	01/1940–12/2014

Table 4: Tide gauges, current meter and temperature/salinity time series mooring sites selected for comparisons with model output.

ter for Operational Oceanographic Products and Services (CO-OPS) Tides and Current web archive https://tidesandcurrents.noaa.gov/. Tide gauge data are used to evaluate the model's response to wind-driven sea level setup and setdown.

Summary meteorological data that represent the regional wind and temperature fields come from the long-term weather station PABR located at the Utqiaġvik Airport (formerly Barrow Airport), and were downloaded from NOAA's National Centers for Environmental Information (NCEI) at https://www.ncdc.noaa.gov/, formerly the National Climate Data Center (NCDC). These we summarized in the form of monthly statistics using the archived National Weather Service wind record in Barrow from 1940-2014 (Figure 9).

Remotely sensed ice concentration data comes from the National Snow and Ice Data Center (NSIDC) archives of the passive microwave SSM/I satellite measurements and is available on a daily or bi-daily basis for the entire model integration period. Data were collected by the Nimbus-7 Scanning Multichannel Microwave Radiometer (SMMR), the Defense Meteorological Satellite Program (DMSP) -F8, -F11 and -F13 Special Sensor Microwave/Imagers (SSM/Is), and the DMSP-F17 Special Sensor Microwave Imager/Sounder (SSMIS). We use data processed with the Goddard Flight Space Center's NASA team algorithm, version 1.1, downloaded January 2018. We note that ice area is a computation that scales each grid cell's area by its fractional ice cover, with resulting units of km^2. Ice area differs from the other common satellite-based ice cover metric, ice extent, which computes the total area bounded by the ice edge contour, also reported with units of km^2. The latter metric ignores leads and features of partial ice cover that lie within the greater ice pack. The ice area metric provides a more realistic measure of the fraction of ocean that is covered by ice and consequently may provide a better measure of the amount of surface that can be characterized by high and low albedos that are associated with ice and ocean surfaces, respectively. However, the satellite data is known to be sensitive to ice and snow conditions and interpretation of the data must be done with care.

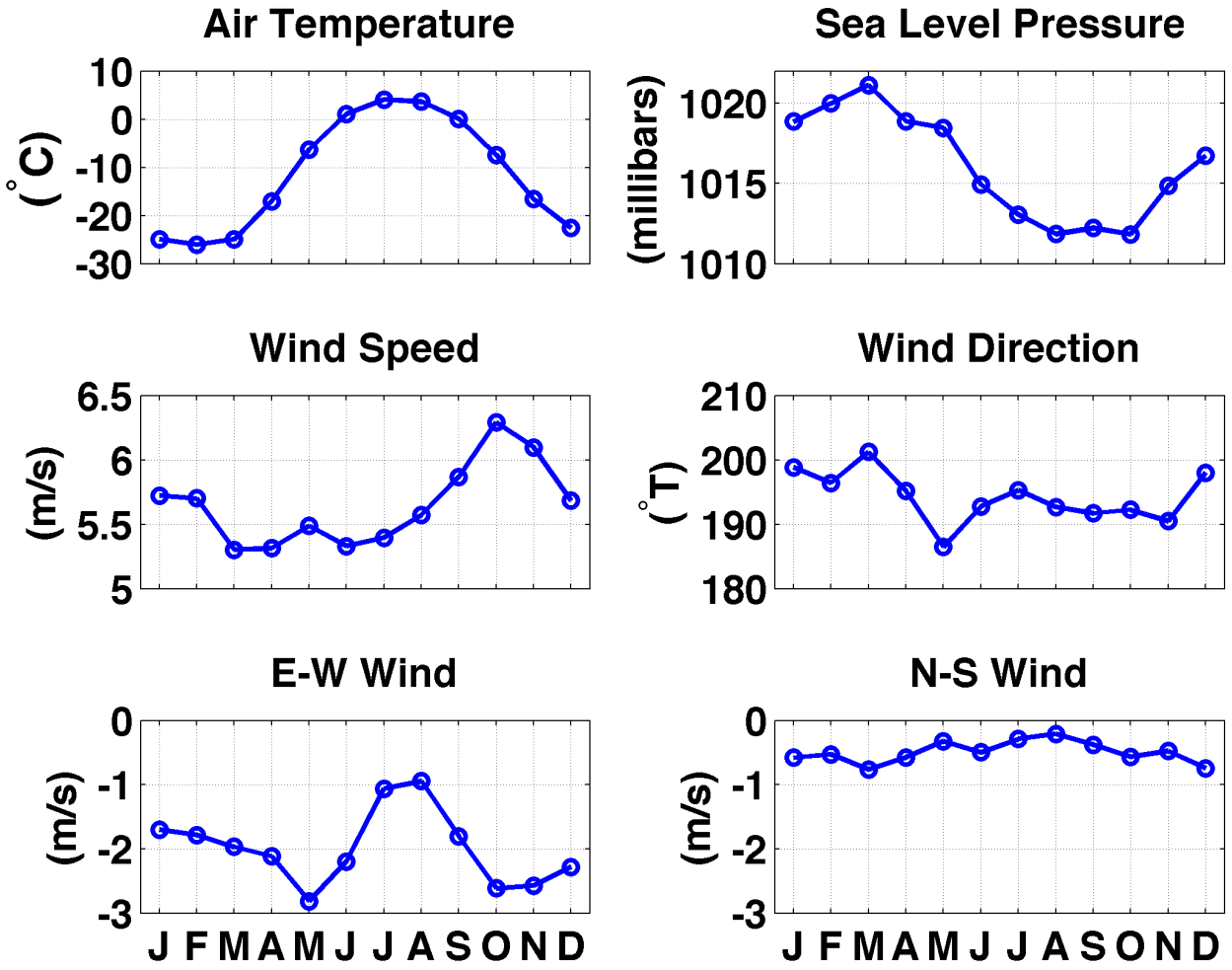

Figure 9: Monthly climatology from Utqiaġvik (formerly Barrow) of hourly meteorological data over 1940-2014. Top row: air temperature and sea level pressure. Middle row: wind speed magnitude and direction to which the wind blows. Bottom row: U (east-west) and V (north-south) wind vector components.

4.1.2 Model evaluation overview

To show the seasonal progression of the various models' behavior for surface thermal and ice fields over the full dynamic range of conditions, we graph summary monthly mean model fields from April, June, September, and December in Figures 10 through 21. These include temperature from the Pan-Arctic model (Figure 10), the Beaufort 2 model (Figure 11) and the Beaufort 3 model (Figure 12).

We save the ocean and sea ice fields for the duration of the model simulation. All output is in NetCDF format. Restart, daily averages, three-hourly averaged surface fields, stations and floats. The three-hourly surface data was delivered to BOEM as required. We present here a series of figures of climatological values of sea surface temperature, ice extent, ice thickness and ice velocity (as a proxy for land-fast ice) for four different months, for each of the three model simulations described above.

Sea surface temperature climatology for the three runs is shown in Figures 10–12. Areas covered by sea ice are colder than $-1°C$, including the central Arctic all year round. Waters on the Pacific and Atlantic sides of the Arctic show a clear annual cycle of summer warming and winter cooling. The open boundaries appear to be well-behaved except possibly to the east of Greenland, where cold outflow from the Arctic meets a warm band of water being nudged to SODA fields. For the Beaufort Sea domains, the SST remains cool year-round except in the location of warm river inflows.

The ice concentration climatology for the three domains is shown in Figures 13–15. The ice extent is at a minimum in September, when it retreats completely from the Beaufort3 domain. Quick comparisons with the satellite ice extent show that we've got a reasonable seasonal cycle, better than in previous iterations of the Pan-Arctic model. A more quantitative comparison will follow. The nested domains show very little boundary effects from the nesting, though the Beaufort3 domain shows some artifacts from mismatch with the values being nudged to on the western part of the boundary, especially in April and June.

The ice thickness climatology for the three domains is shown in Figures 16–18. There is less thickness than ice concentration data for model evaluation. Typically, the model ice tends to be thinner than observations. The bias could be due to having a single ice category in our model. Experiments with the Community Ice Model (CICE) coupled to ROMS develop a thicker ice climatology using five ice thickness categories.

The Beaufort2 domain shows no obvious boundary effects in the thickness fields, while the Beaufort3 domain shows hints of disagreement with the nudging from the Beaufort2 grid along the western boundary, especially in April and June. The sea ice is quite dynamic on the outer boundary of the Beaufort3 domain; perhaps this wasn't the wisest location for a grid open boundary.

Figures 19–21 show the ice speed, with the 5×10^{-4} m/s contour showing the edge of the landfast ice. The Pan-Arctic domain has landfast ice in April and June in the Canadian

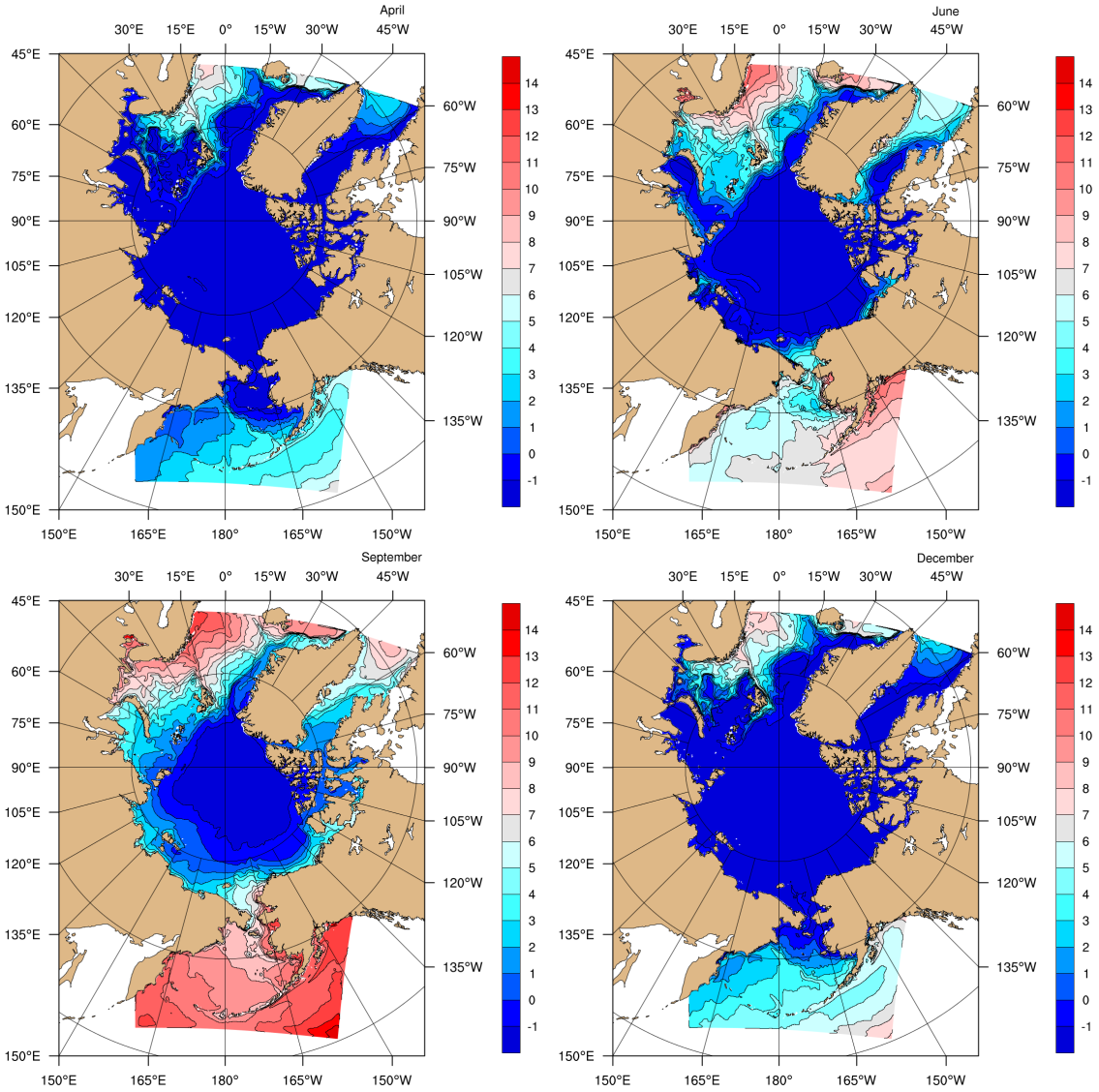

Figure 10: Pan-Arctic model climatological sea surface temperature (^oC) for April, June, September and December.

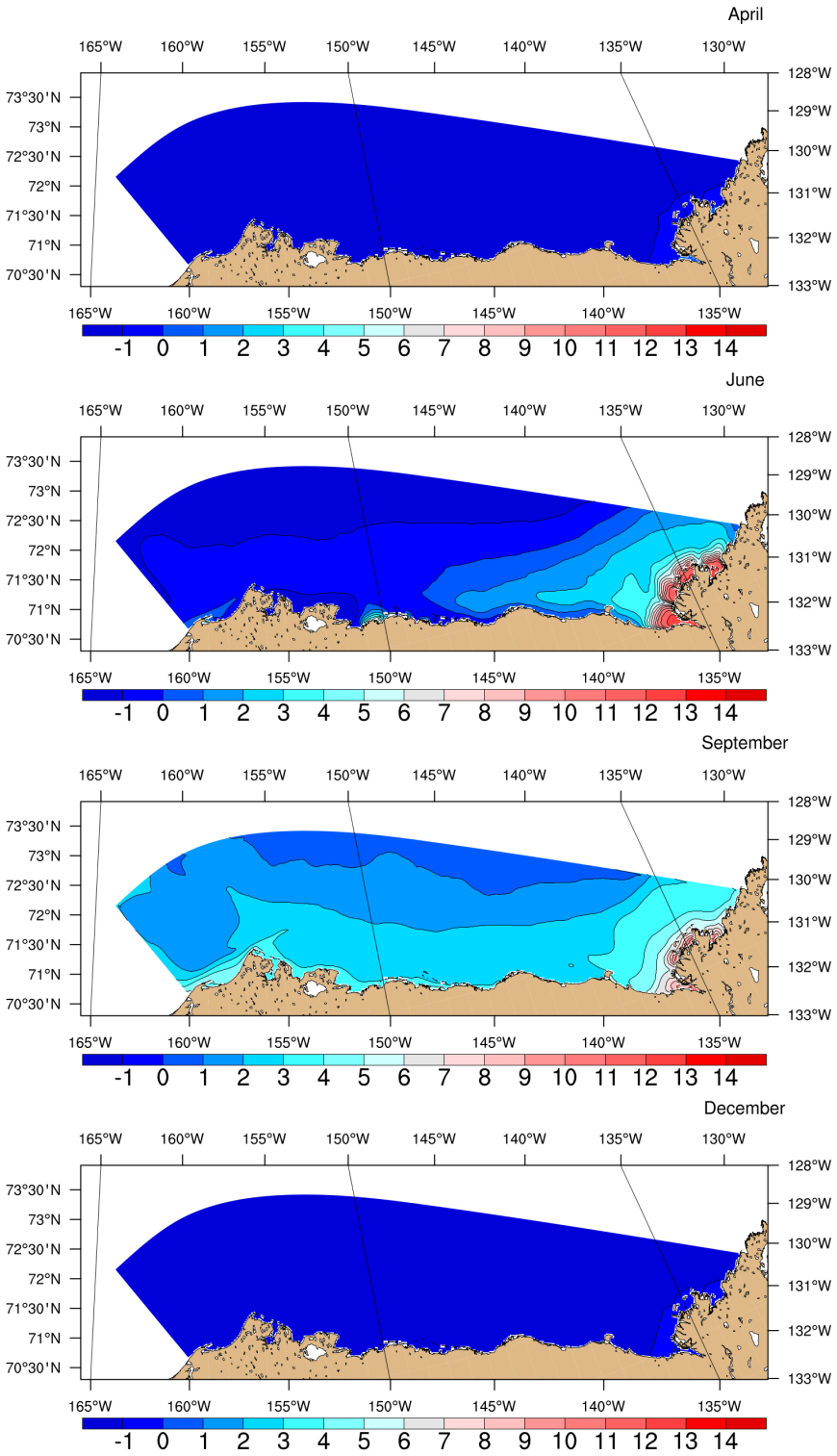

Figure 11: Beaufort 2 model climatological sea surface temperature (^oC) for April, June, September and December.

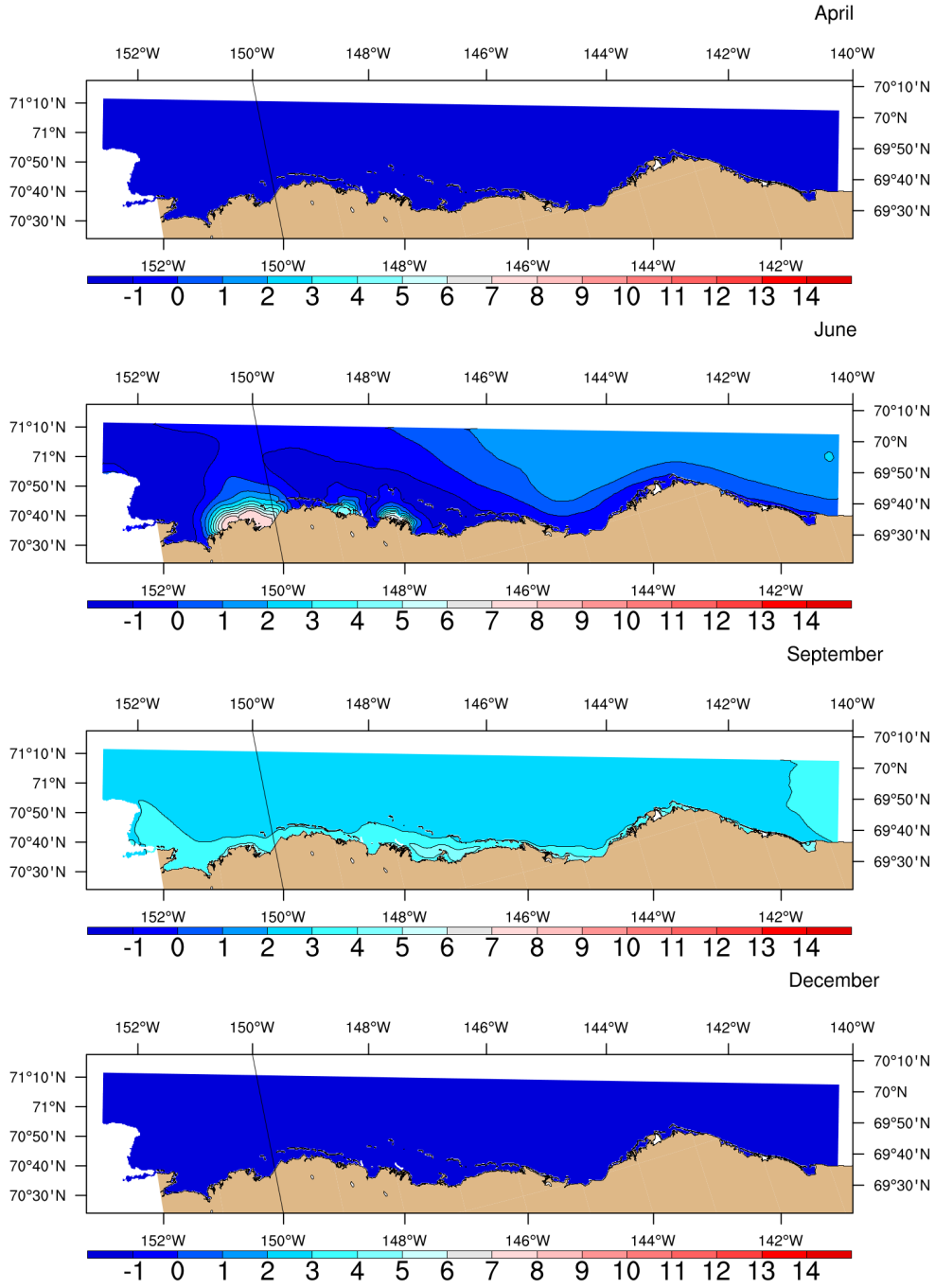

Figure 12: Beaufort 3 model climatological sea surface temperature (^oC) for April, June, September and December.

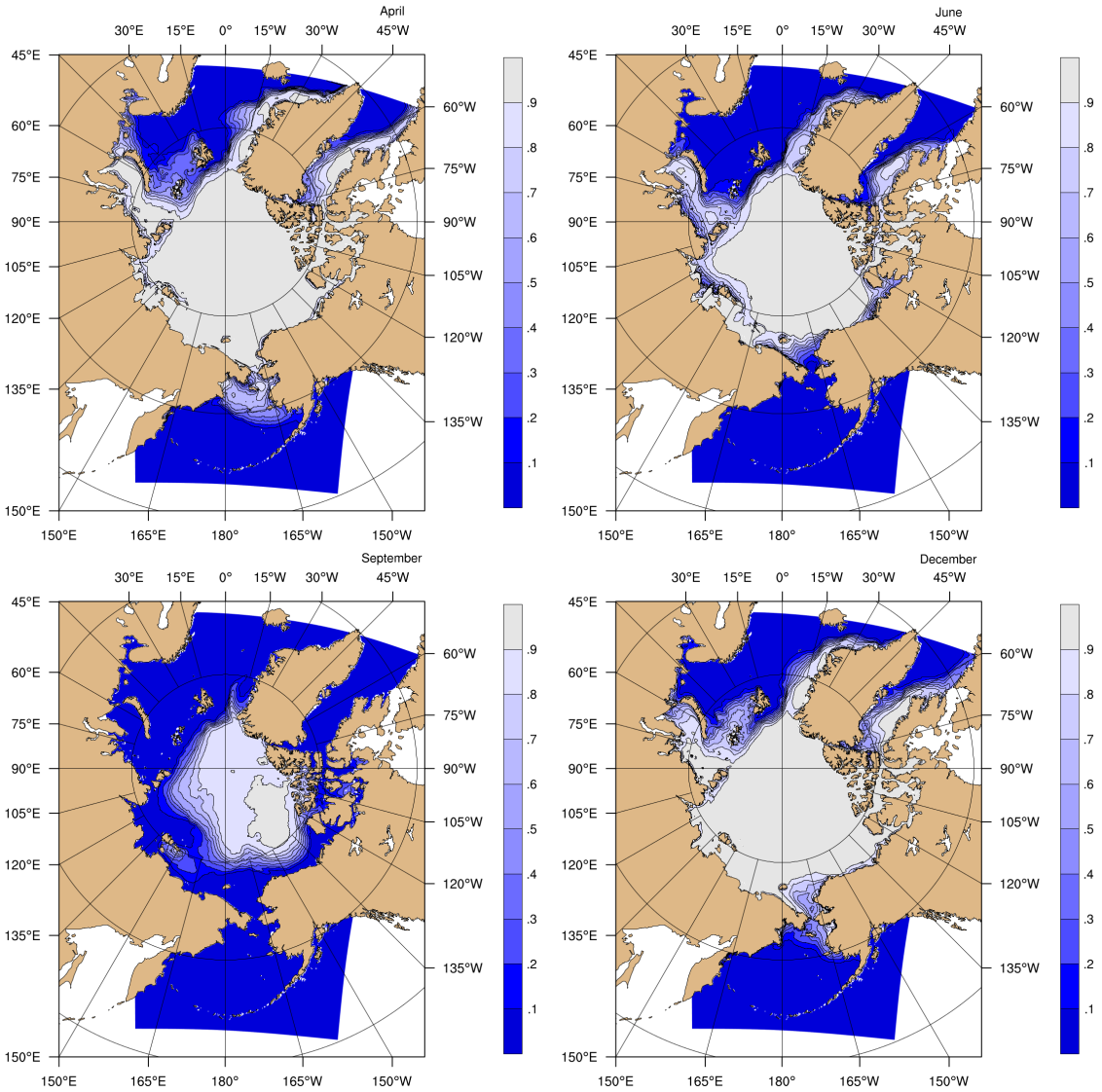

Figure 13: Pan-Arctic model climatological ice extent for April, June, September and December.

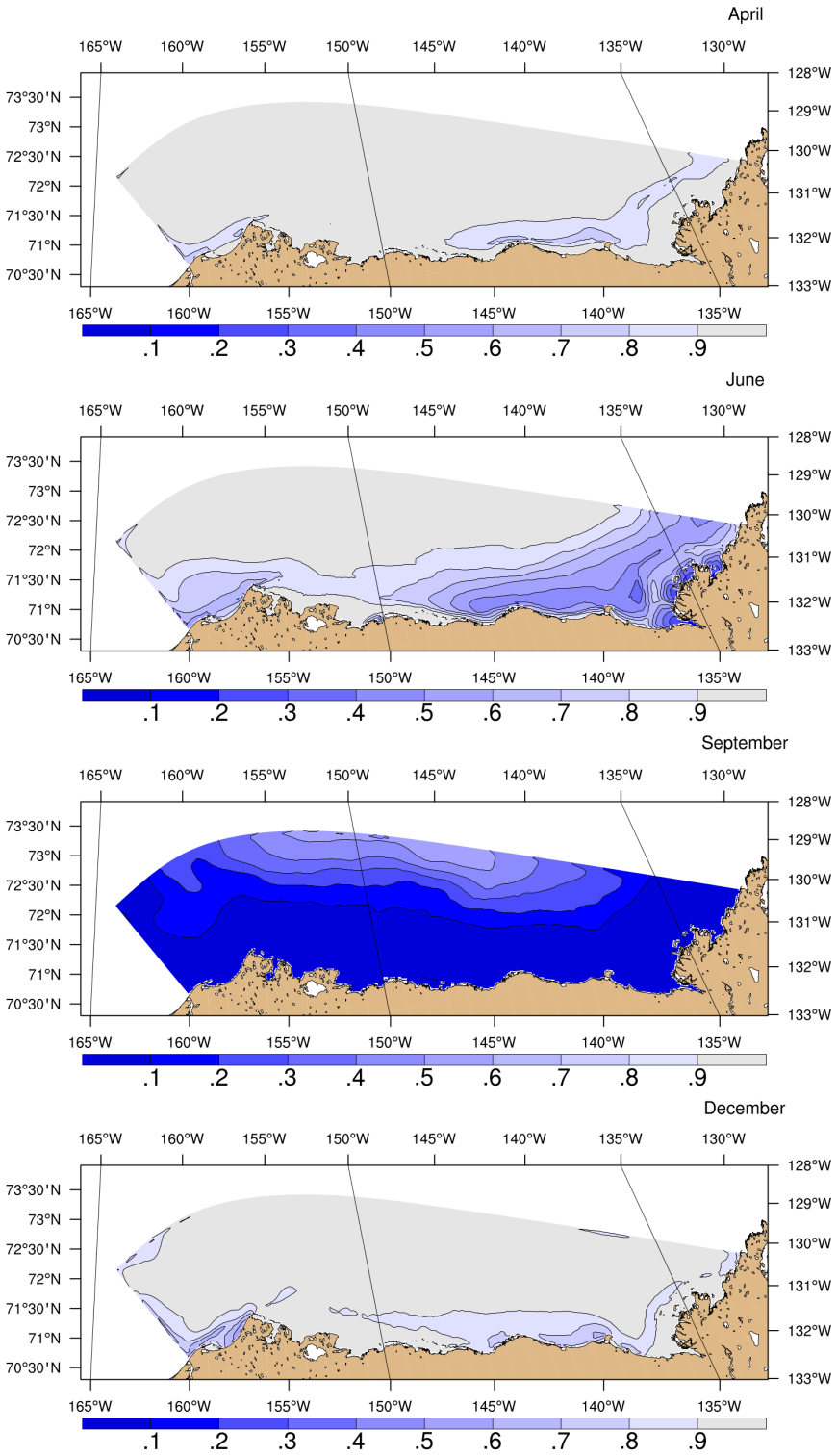

Figure 14: Beaufort 2 model climatological ice extent for April, June, September and December.

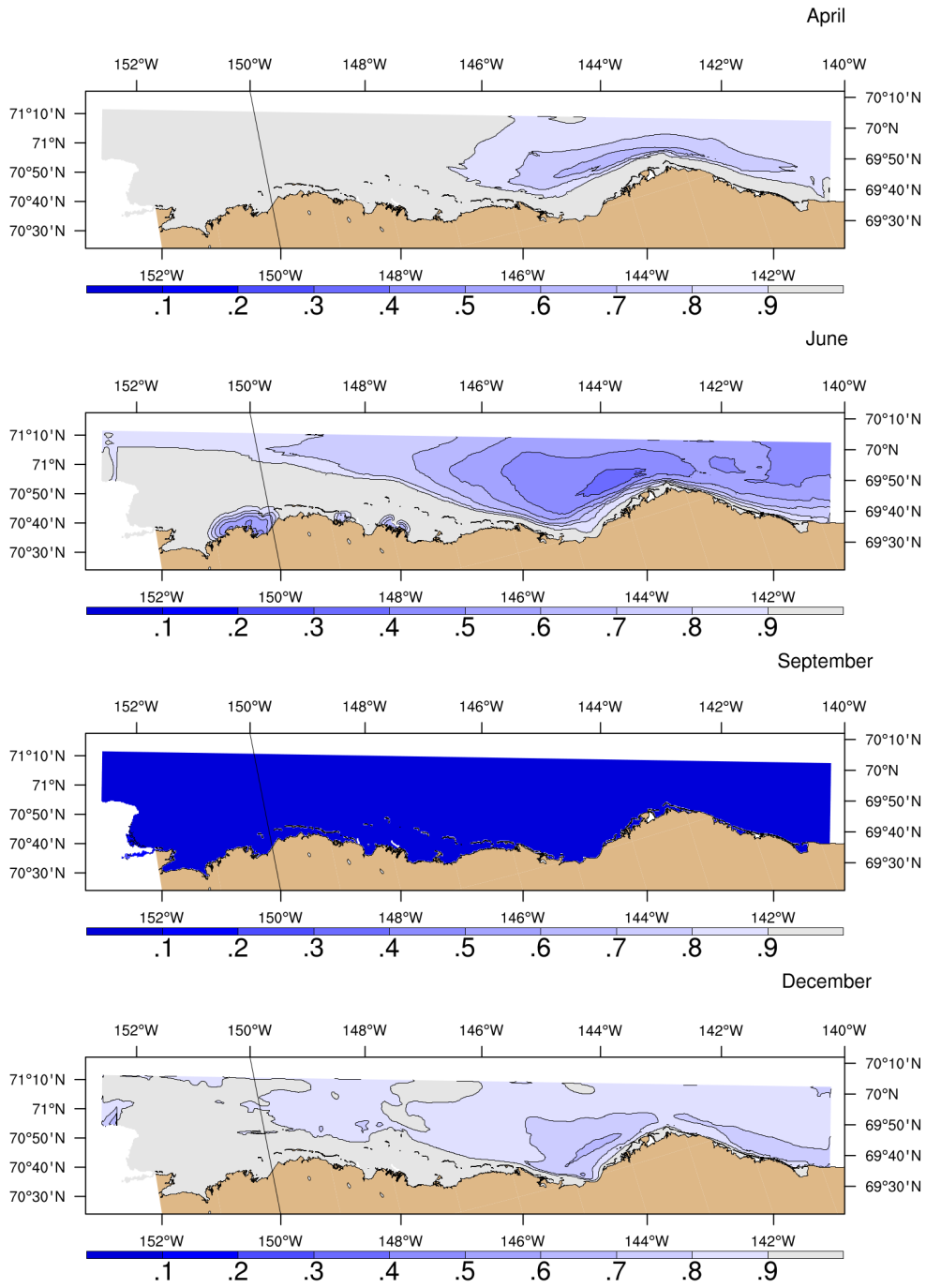

Figure 15: Beaufort 3 model climatological ice extent for April, June, September and December.

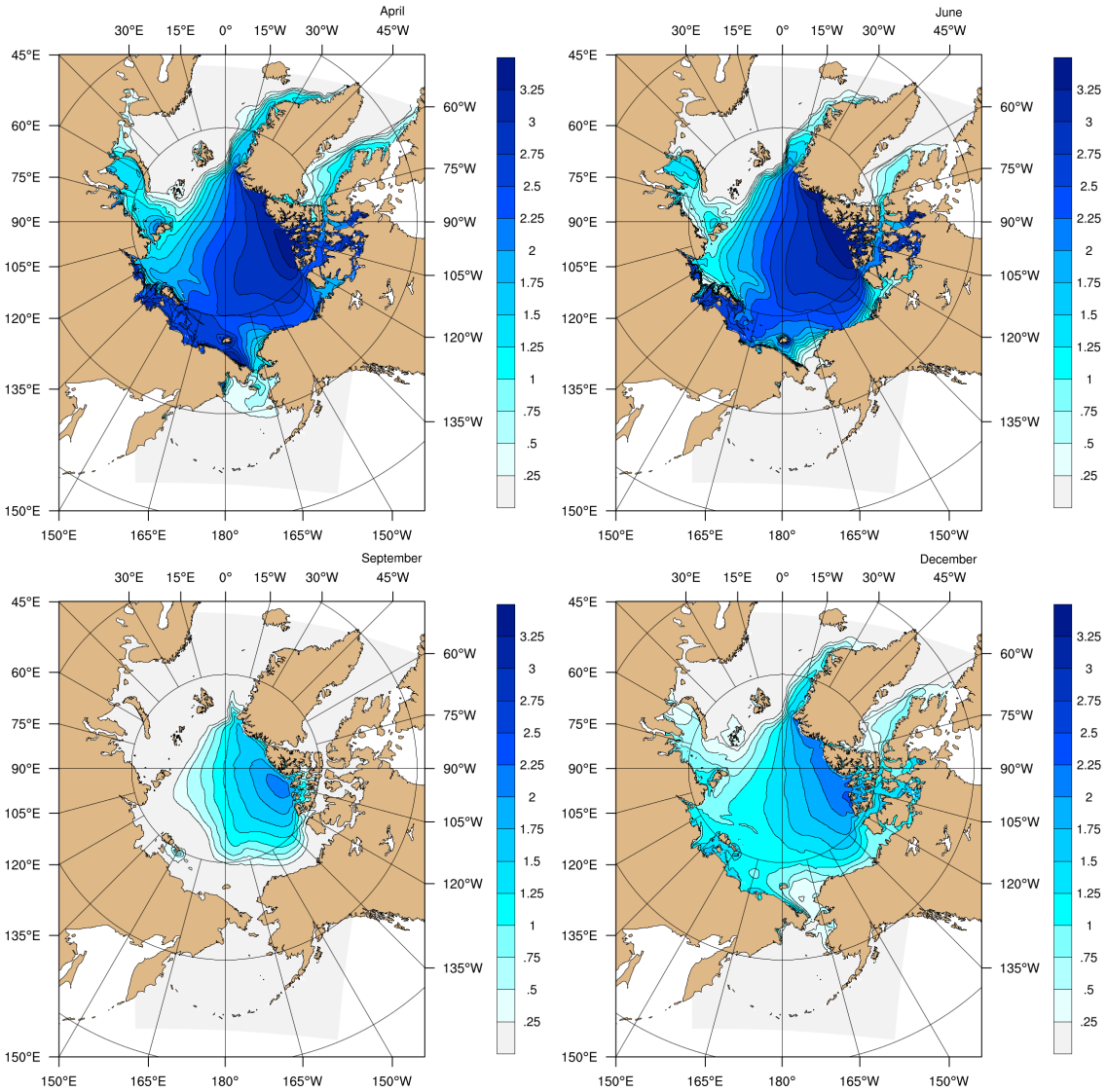

Figure 16: Pan-Arctic model climatological ice thickness (meters) for April, June, September and December.

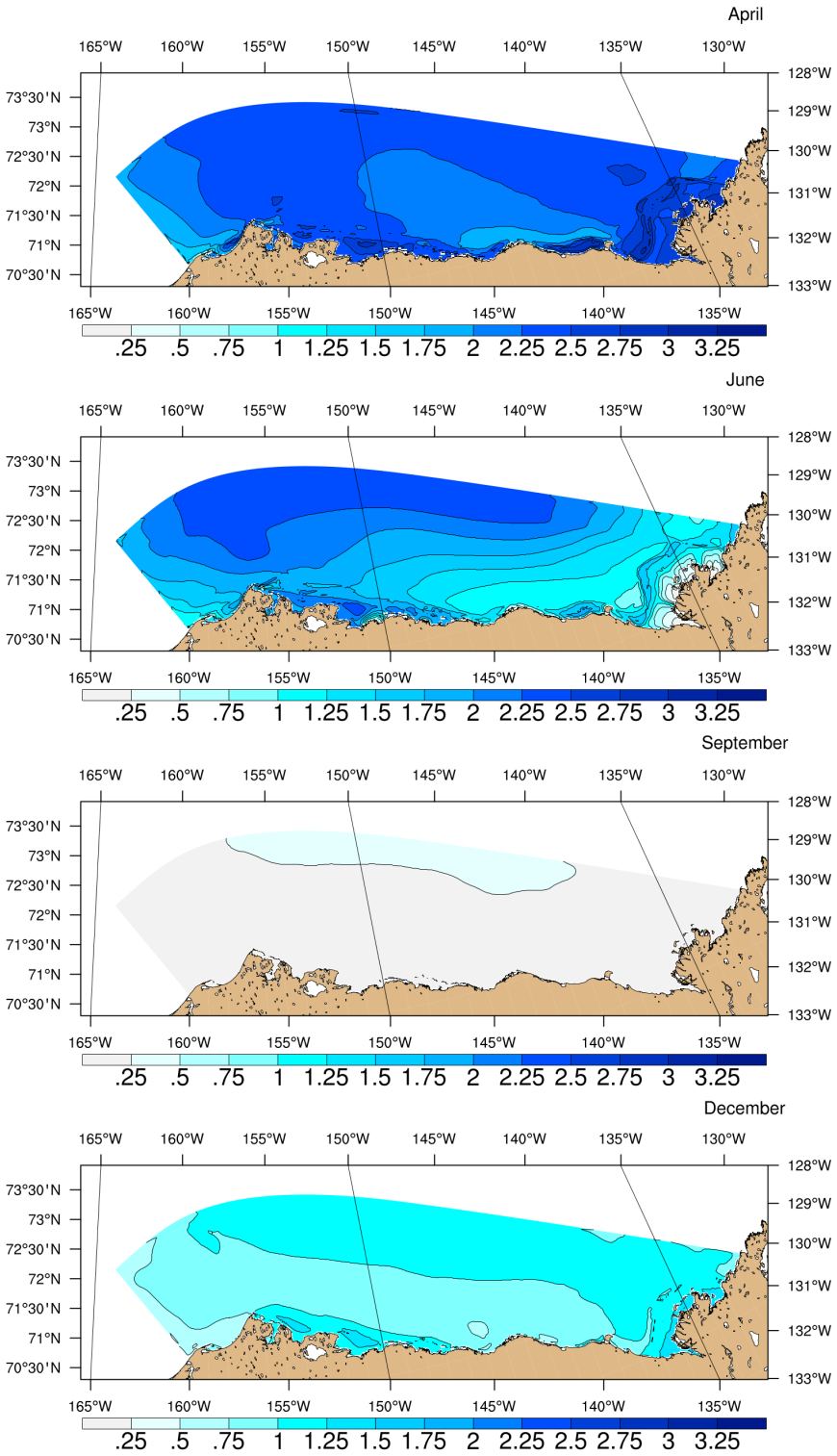

Figure 17: Beaufort 2 model climatological ice thickness (meters) for April, June, September and December.

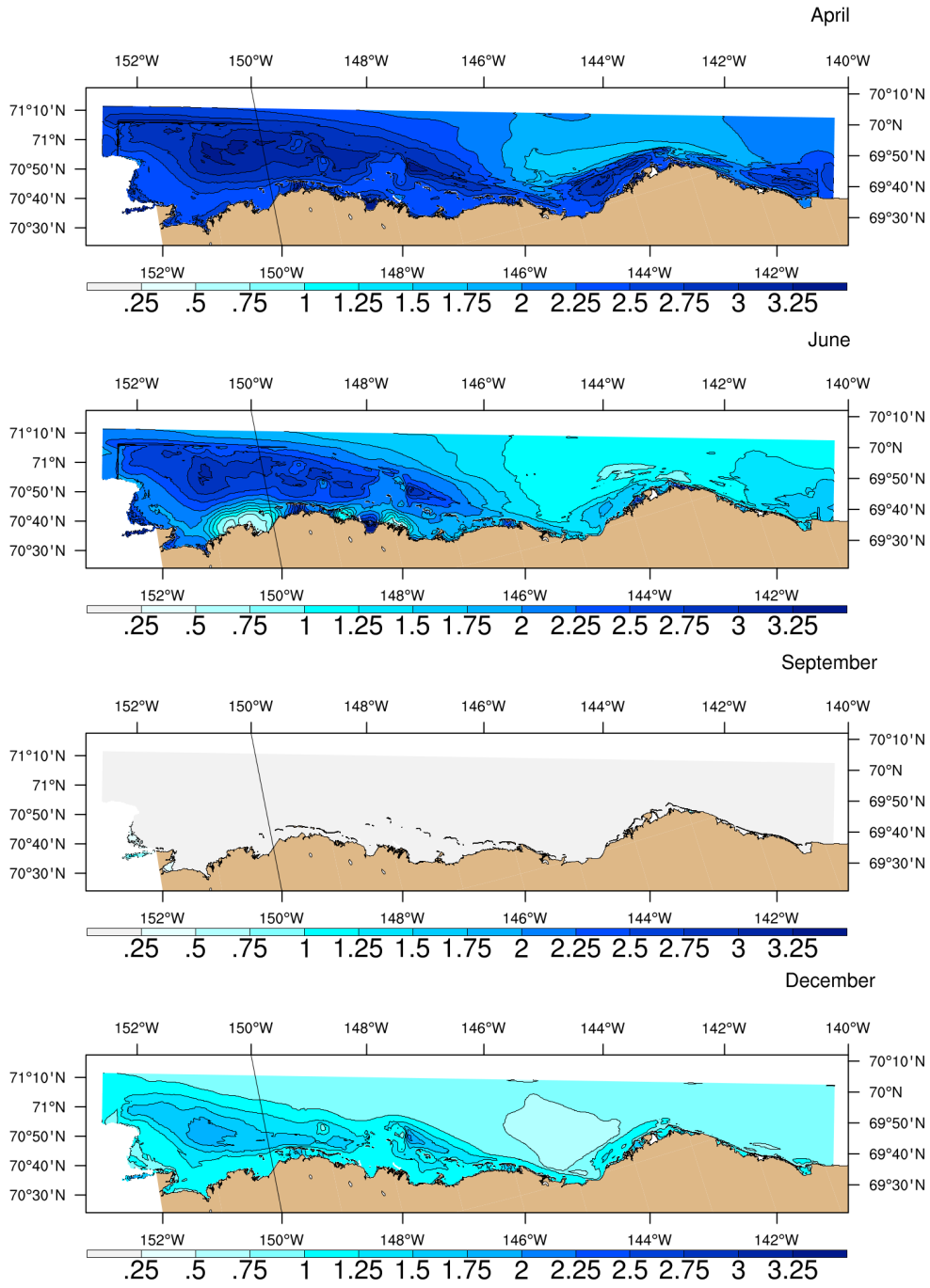

Figure 18: Beaufort 3 model climatological ice thickness (meters) for April, June, September and December.

Archipelago as well as along the Siberian coast. This version of the landfast ice parameterization is only active in shallow water. Lemieux (personal communication) has since adjusted the sea-ice rheology to allow for better agreement with landfast ice observations, which he tested in the Kara Sea. In particular, the new formulation allows for some small tensile strength in the ice that helps the representation of the landfast ice.

The Beaufort 2 and Beaufort 3 domains give a better view of where the model is developing landfast ice. It is at the maximum in April, where it develops along much of the Beaufort coast. It extends farthest offshore at the Mackenzie delta, where the water is shallow. It also extends to the boundary nudging band in the Beaufort3 domain on the western edge. It is clear from these figures that we turned off the fastice parameterization within the boundary nudging band in order to avoid excessive ice locking there.

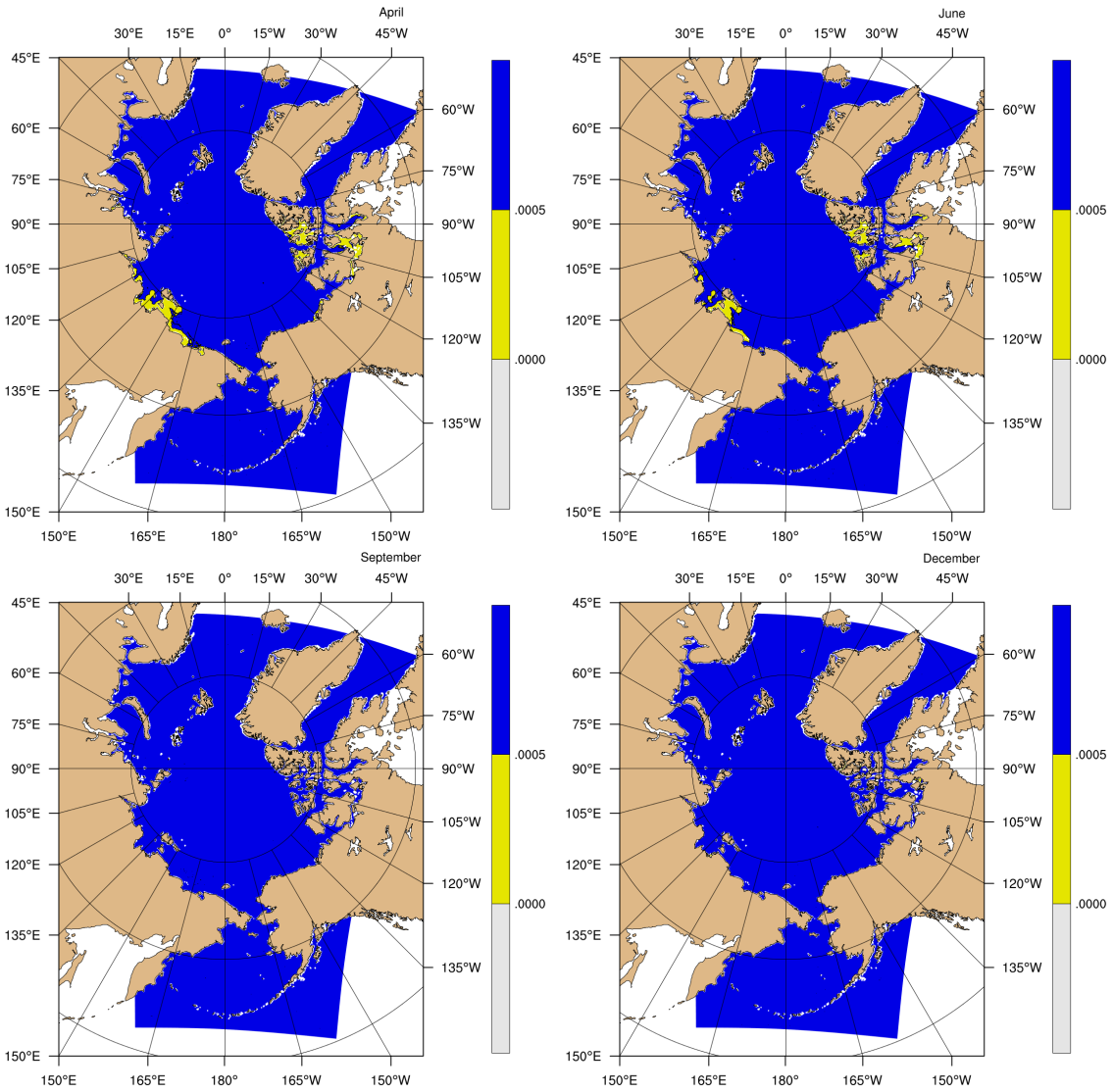

Figure 19: Pan-Arctic model climatological ice speed for April, June, September and December. Contour level (0.0005 m/s) chosen to identify the landfast ice.

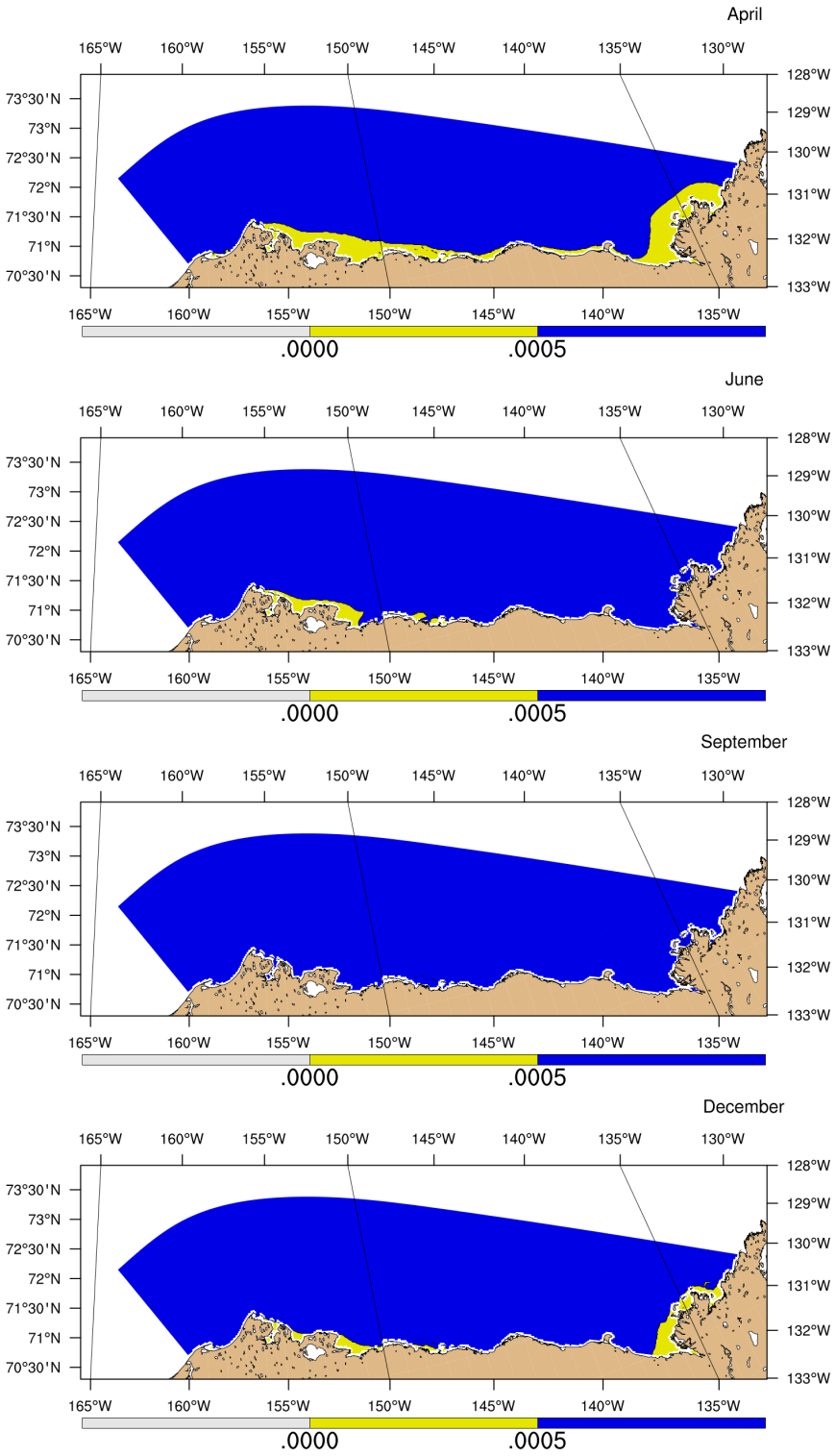

Figure 20: Beaufort 2 model climatological ice speed for April, June, September and December. Contour level (0.0005 m/s) chosen to identify the land-fast ice.

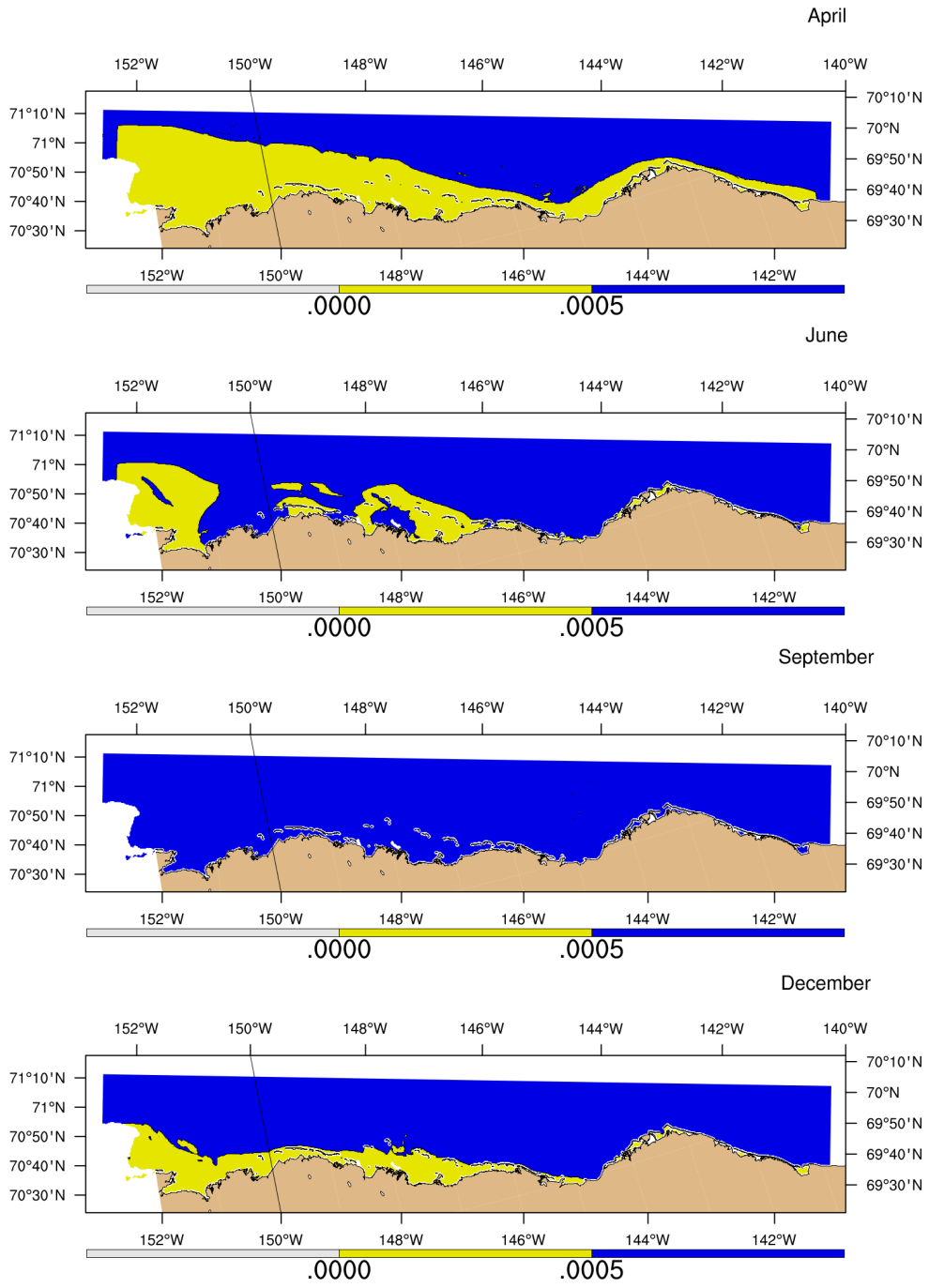

Figure 21: Beaufort 3 model climatological ice speed for April, June, September and December. Contour level (0.0005 m/s) chosen to identify the land-fast ice.

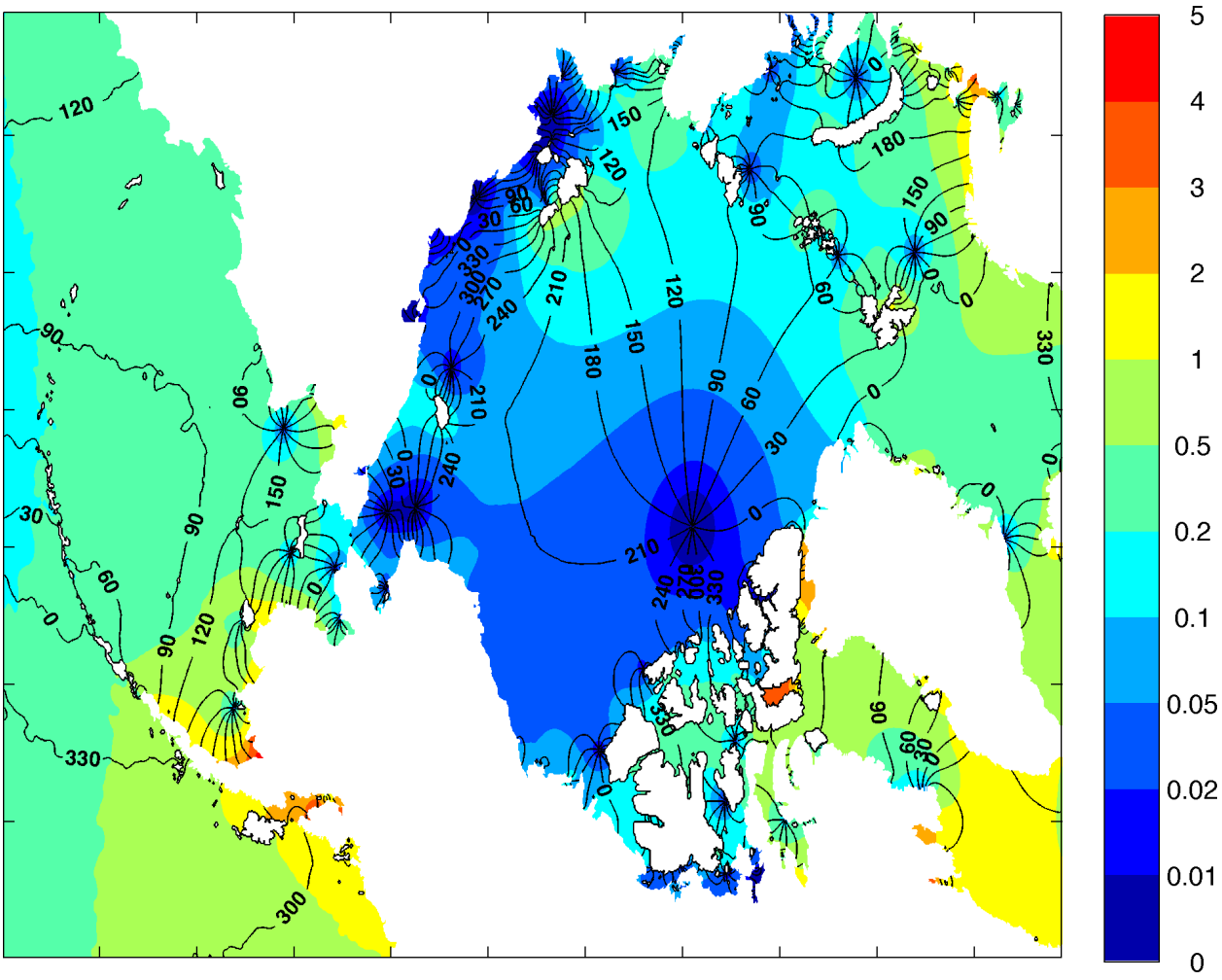

Figure 22: Coamplitude elevation in meters (color shading) and cophase in degrees (black line) contours for semidiurnal tidal constituent M2.

4.2 Model-data comparisons

Figures 22–25 are cotidal charts for the Arctic2 model semidiurnal constituents M2 and S2 and the diurnal constituents K1 and O2, respectively. The location of amphridromes and the magnitude of the elevations compare favorably with tidal models of the Bering Sea, Gulf of Alaska, and Arctic Ocean tides (e.g., Kowalik and Proshutinsky, 1993; Padman and Erofeeva, 2004). Achieving phasing that matches the phase of the observed tides is somewhat more difficult than achieving proper harmonic amplitudes as the tidal phase can change under different stratification and ice cover conditions. For the case of the tidal analyses shown here, the analysis was based on one month of mid-winter (full ice cover and seasonally low stratification) model results.

Sea surface height (SSH) fluctuations are surface adjustments to oceanic flows, which can be driven by winds, tides, and other surface and internal forces. SSH fluctuations

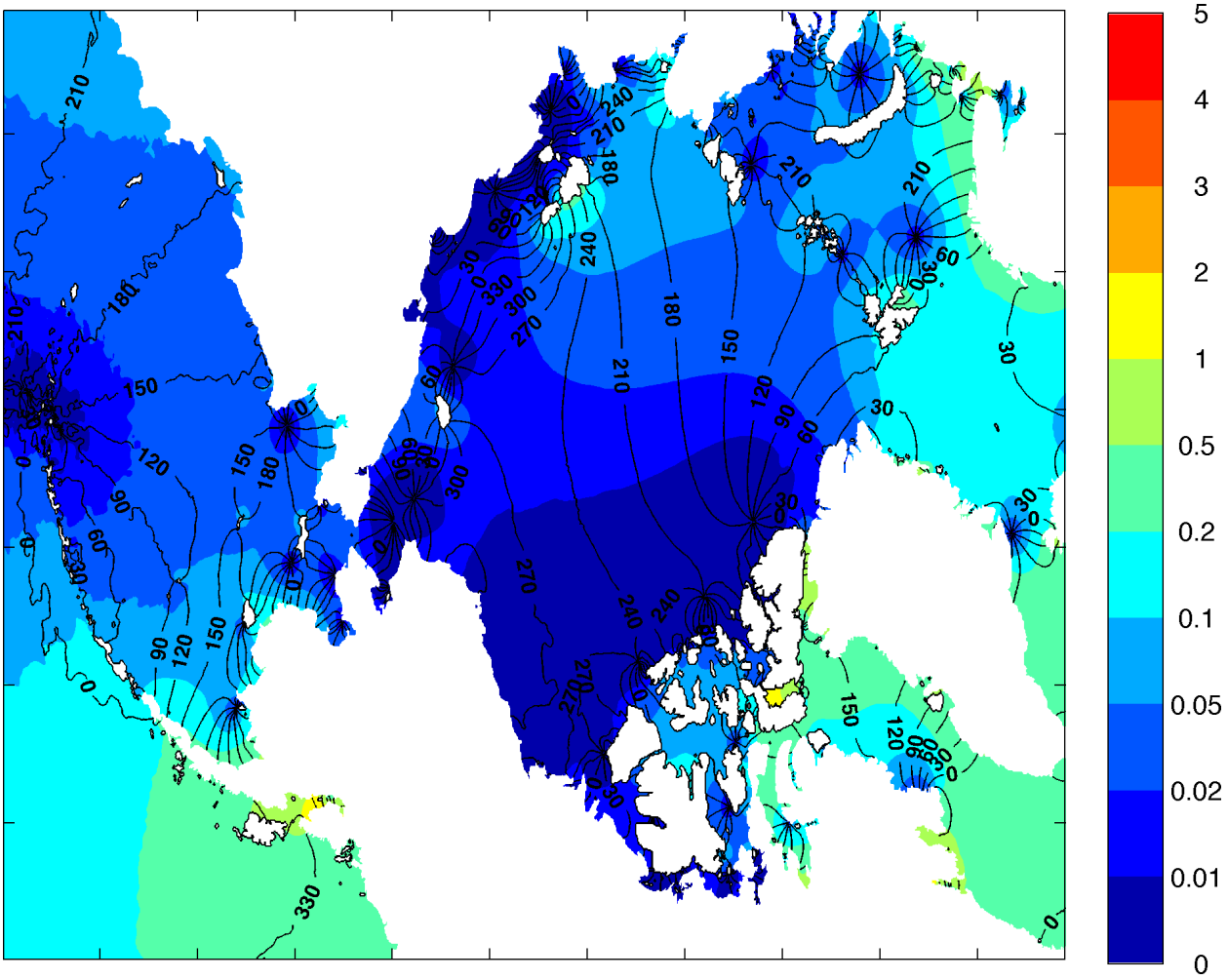

Figure 23: Coamplitude elevation in meters (color shading) and cophase in degrees (black line) contours for semidiurnal tidal constituent S2.

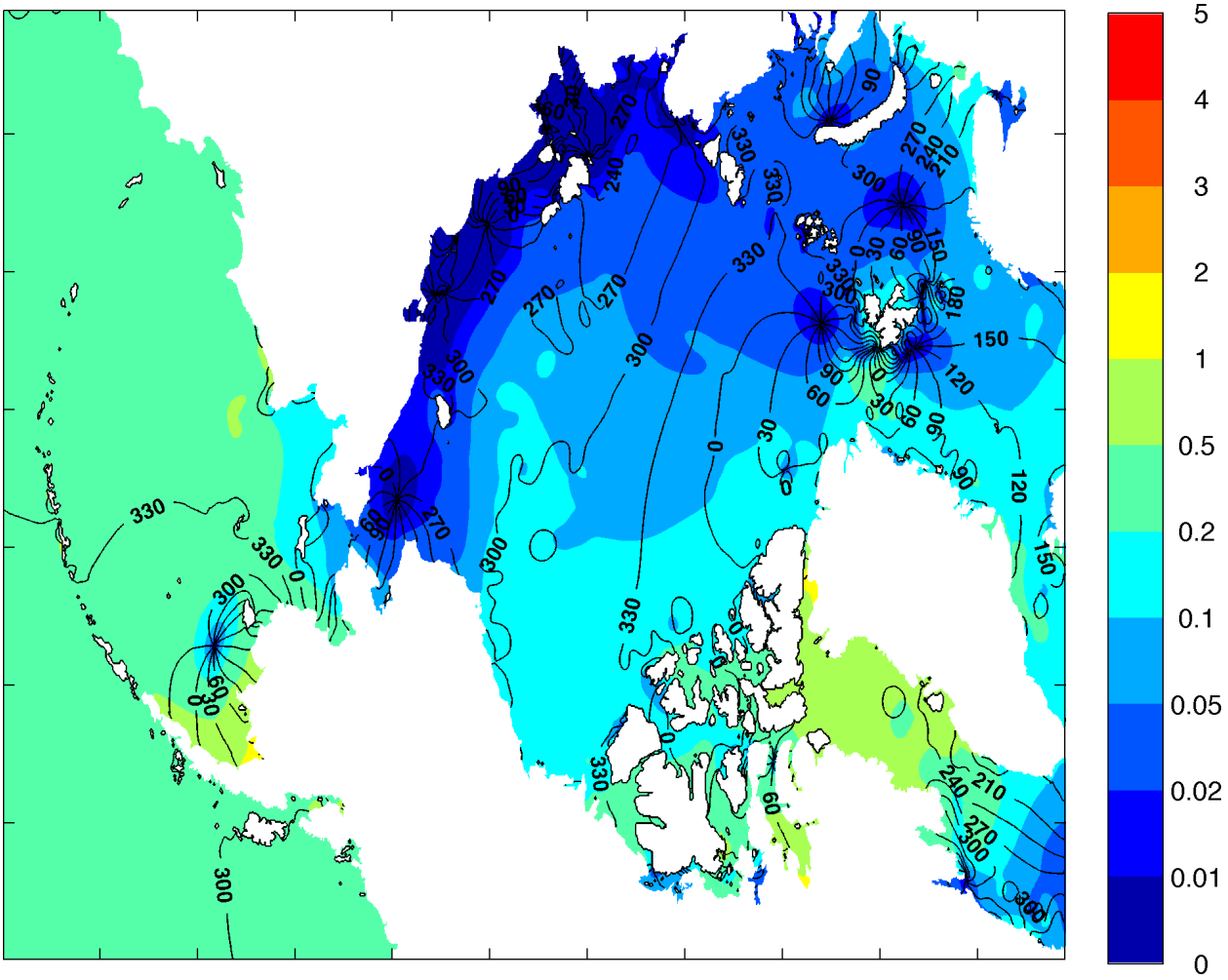

Figure 24: Coamplitude elevation in meters (color shading) and cophase in degrees (black line) contours for diurnal tidal constituent K1.

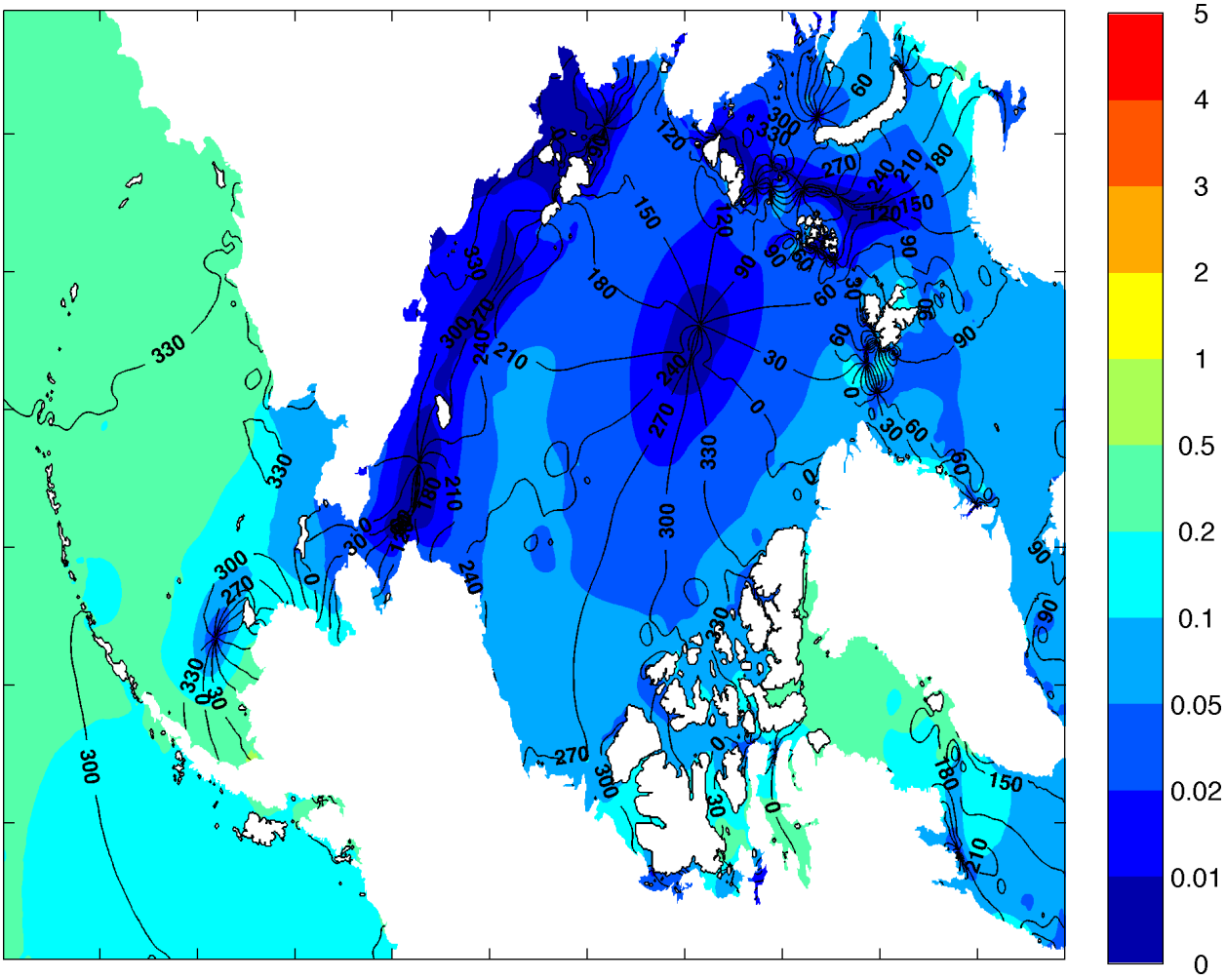

Figure 25: Coamplitude elevation in meters (color shading) and cophase in degrees (black line) contours for diurnal tidal constituent O1.

can be the result of local forcing, such as wind stress directly applied to the local ocean surface, or the result of disturbances that propagate into a region from a distance, such as progressive tides or continental shelf waves. Tidally filtered SSH fields from the Arctic2 version of the PAROMS model and from coastal tide gauge stations observations at Nome, Red Dog and Prudhoe Bay (Figure 8) are similar in character, although the model slightly underestimates the magnitude of the fluctuations at Prudhoe slightly more than for the other two stations (Figure 26). The two Beaufort sea nested models exhibit greater fidelity to the observations (Figure 27), suggesting that the PAROMS ETOPO digital elevation model bathymetry in the Beaufort region is markedly inferior to the IBCAO bathymetry that comprises the Beaufort2 and Beaufort3 models. Deviations of the nested grid model results from the observed elevations hint at inadequacies in the surface wind field. Lack of weather stations across the Arctic as a whole limit the ability of atmospheric reanalysis and hindcast models to reproduce high-latitude atmospheric pressure and wind systems with the fidelity achieved in lower latitudes.

Along-shelf pressure gradients that drive shelf flows can be assessed by computing the along-shelf SSH gradient between adjacent stations. This computation shows that the model tends to slightly underestimate the SSH gradient (Figure 28), suggesting that the model will also tend to underestimate the current velocity magnitude. We examine shelf currents in detail in the sections below.

Bering Strait is the single choke-point for flows connecting the North Pacific and Arctic Oceans. Hindcasting a realistic flow field here is critical for accurate reproductions of the entire Chukchi shelf flow field. In turn, the Chukchi flow field helps drive communication between the Chukchi and Beaufort seas. The Beaufort2 nested model grid encapsulates the northeast Chukchi Sea and Barrow Canyon, and this region directly communicates with the western Beaufort. Hence, the long-term monitoring sites in Bering Strait (e.g., Woodgate et al., 2005; Woodgate et al., 2012) provide an important comparison opportunity against observational data for evaluation of the model's performance outside of the Beaufort Sea focus domain. Observations made at Bering Strait's long-term monitoring station A3 in 2005 and 2006 show that the model captures the majority of the principal axis variance observed at A3 and with similar magnitude (Figure 29). On an annual basis (Figure 30), the volume transport (r= 0.68), heat transport (r = 0.83), fresh water transport (r= 0.63) and ice transport of the model is consistent with the values as reported by Woodgate et al. [2012]. These correlations are all significant at the 95% confidence level and explain 46%, 69% and 40% of the observed variance, respectively.

Figures 31 through 44 show comparisons of model-predicted along-shelf (Ur) and cross-shelf (Vr) velocities, temperature, and salinity for moorings at the Smith, Reindeer, Dinkum, and Camden sites. The length of valid salinity records from the Smith and Reindeer moorings was quite short (approximately one month long) and so we do not show those records here.

The salinity comparisons (Figures 31 and 35) show that the Beaufort2 and Beaufort3 nested models reproduce the observed annual cycle with approximately the right phasing and amplitude. Some individual events are not well reproduced; we believe that many

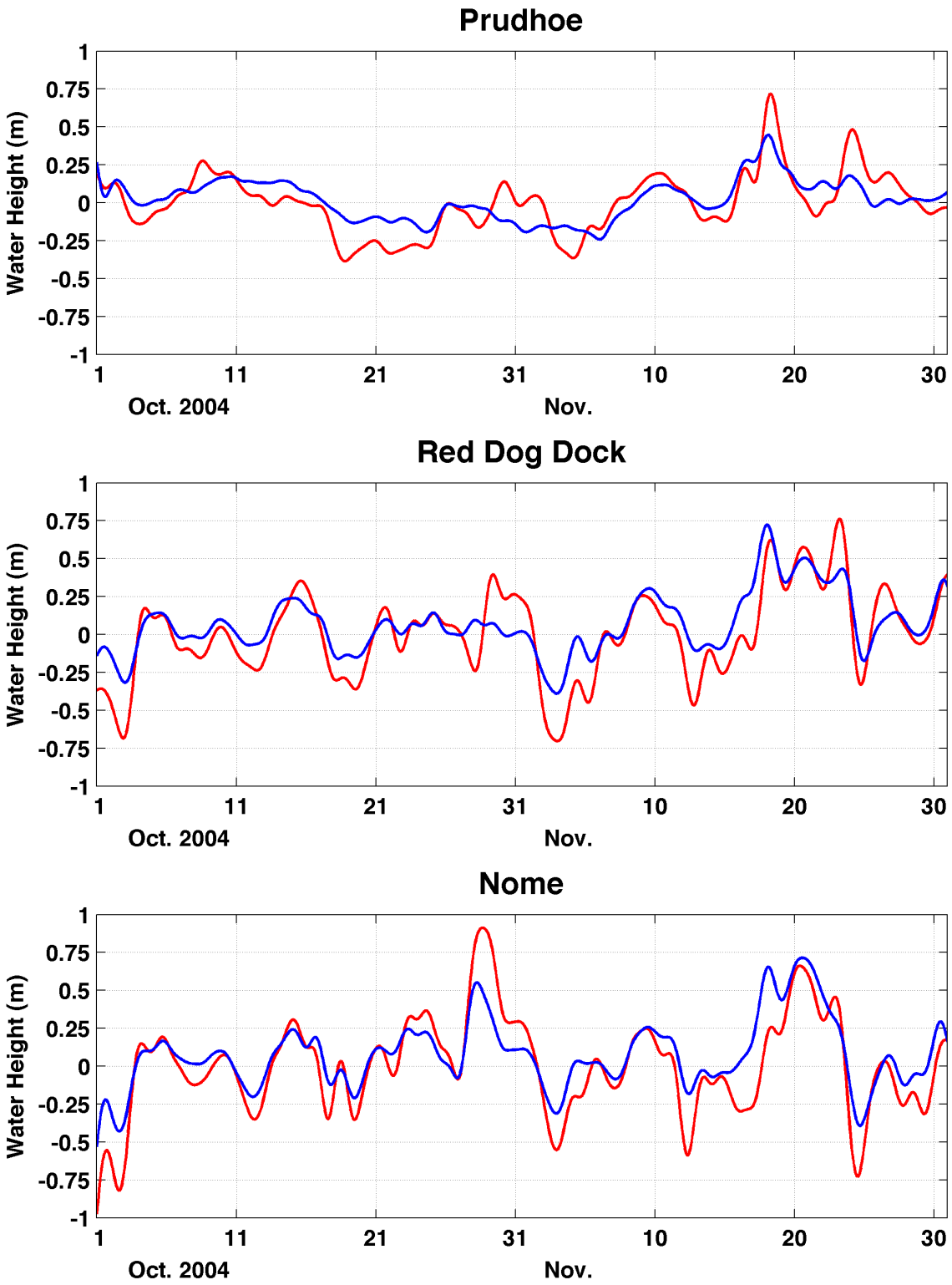

Figure 26: Observed (red) and modeled (blue) sea surface elevations for the NOAA-COOPS tidal station in Prudhoe Bay (top), Red Dog Dock (middle) and Nome (bottom). All fields have been smoothed with a 35-hour low-pass Butterworth filter to remove tides and other high-frequency fluctuations. All model fields are from the Arctic2 model.

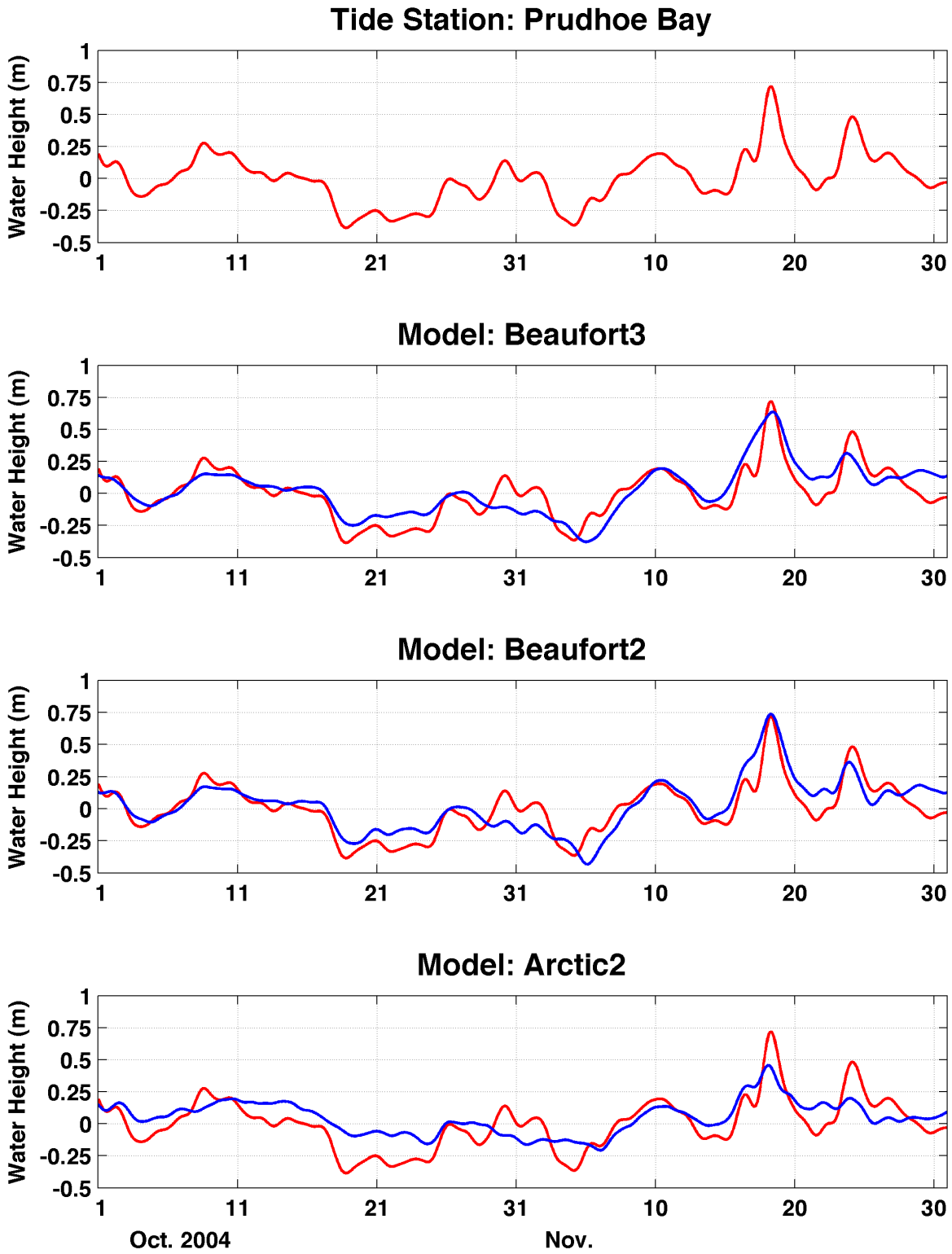

Figure 27: Comparison of observed sea level fluctuations in Prudhoe Bay (top row and all red traces) to modeled sea level fluctuations (blue) for the Beaufort2 (second row), Beaufort3 (third row) and Arctic2 (bottom row) models. All fields have been smoothed with a 35-hour low-pass Butterworth filter to remove tides and other high-frequency fluctuations.

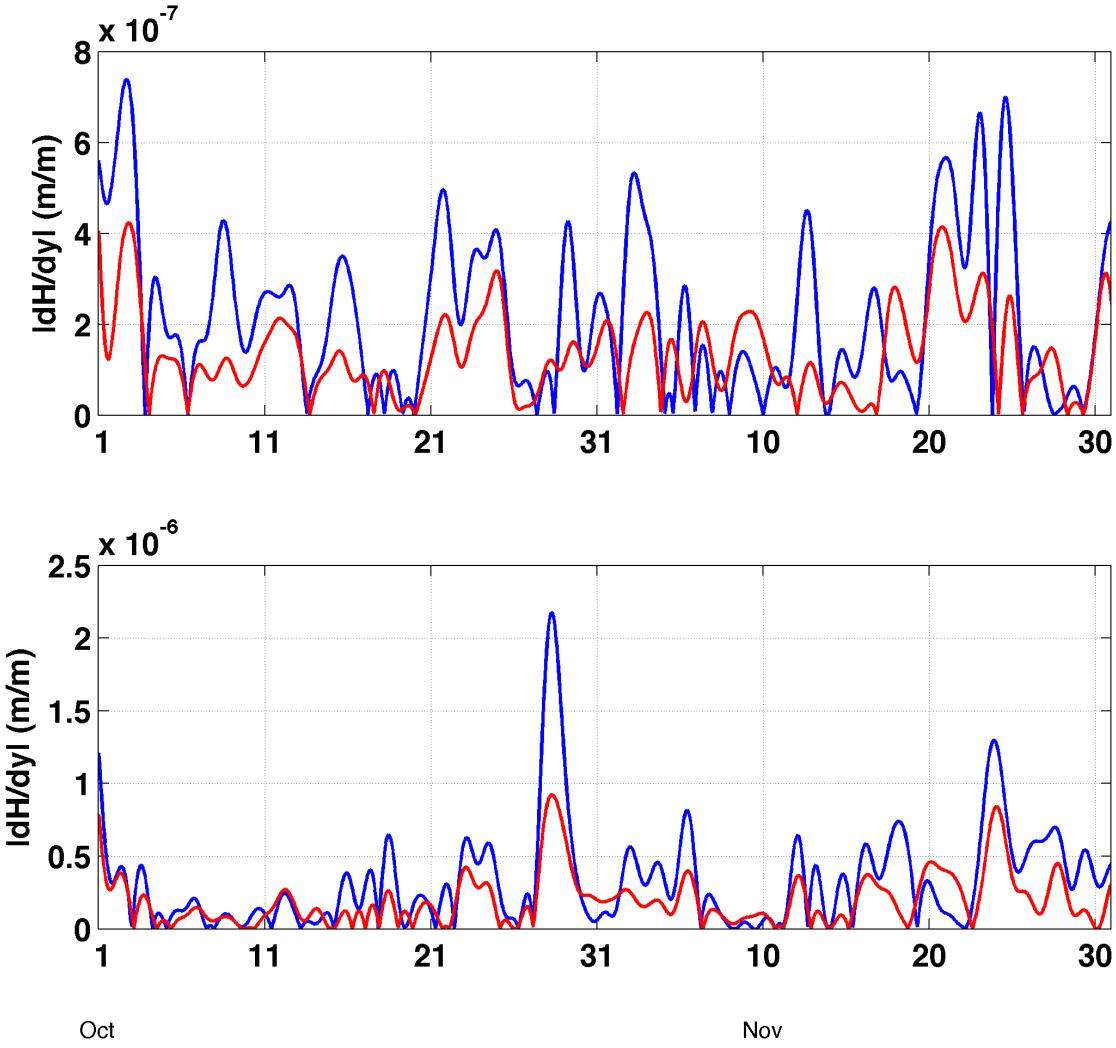

Figure 28: Comparison of the observed (blue) and modeled (red) along-coast sea surface elevation gradient magnitude between Nome and Red Dog Dock (top) and between Red Dog Dock and Prudhoe Bay (bottom). All fields have been smoothed with a 35-hour low-pass Butterworth filter to remove tides and other high-frequency fluctuations.

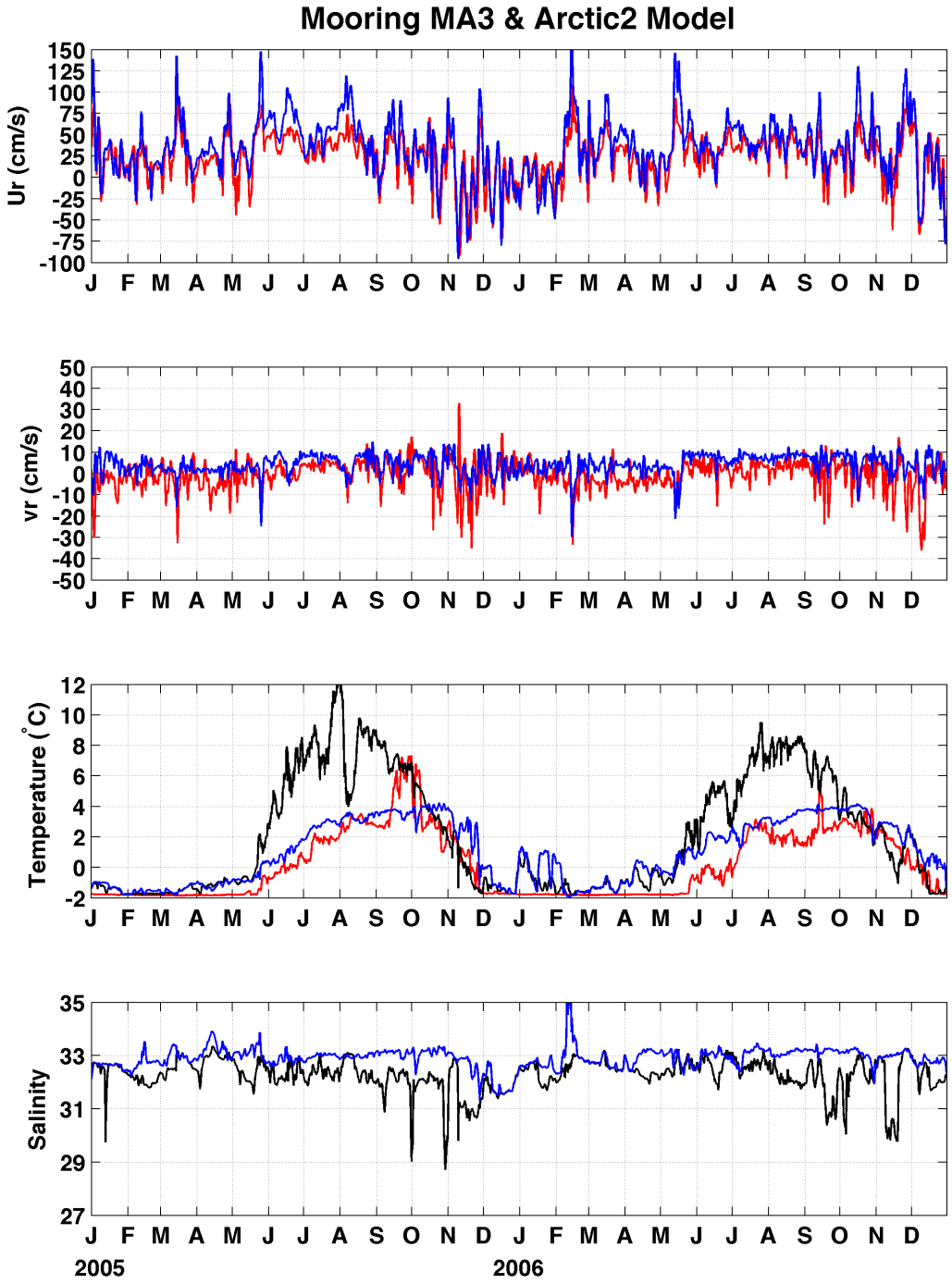

Figure 29: Subtidal comparison of the Arctic2 model with observations in Bering Strait. The top row shows the along-strait velocity (positive nominally northward), the second row show the cross-strait velocity (positive nominally eastward), the third row is temperature and the bottom panel shows modeled salinity. The observed fields are shown with red lines (data collected approximately 10 m above the seafloor). The modeled fields are shown at the surface (black) and at the seafloor (blue). All fields have been smoothed with a 35-hour low-pass Butterworth filter to remove tides and other high-frequency fluctuations.

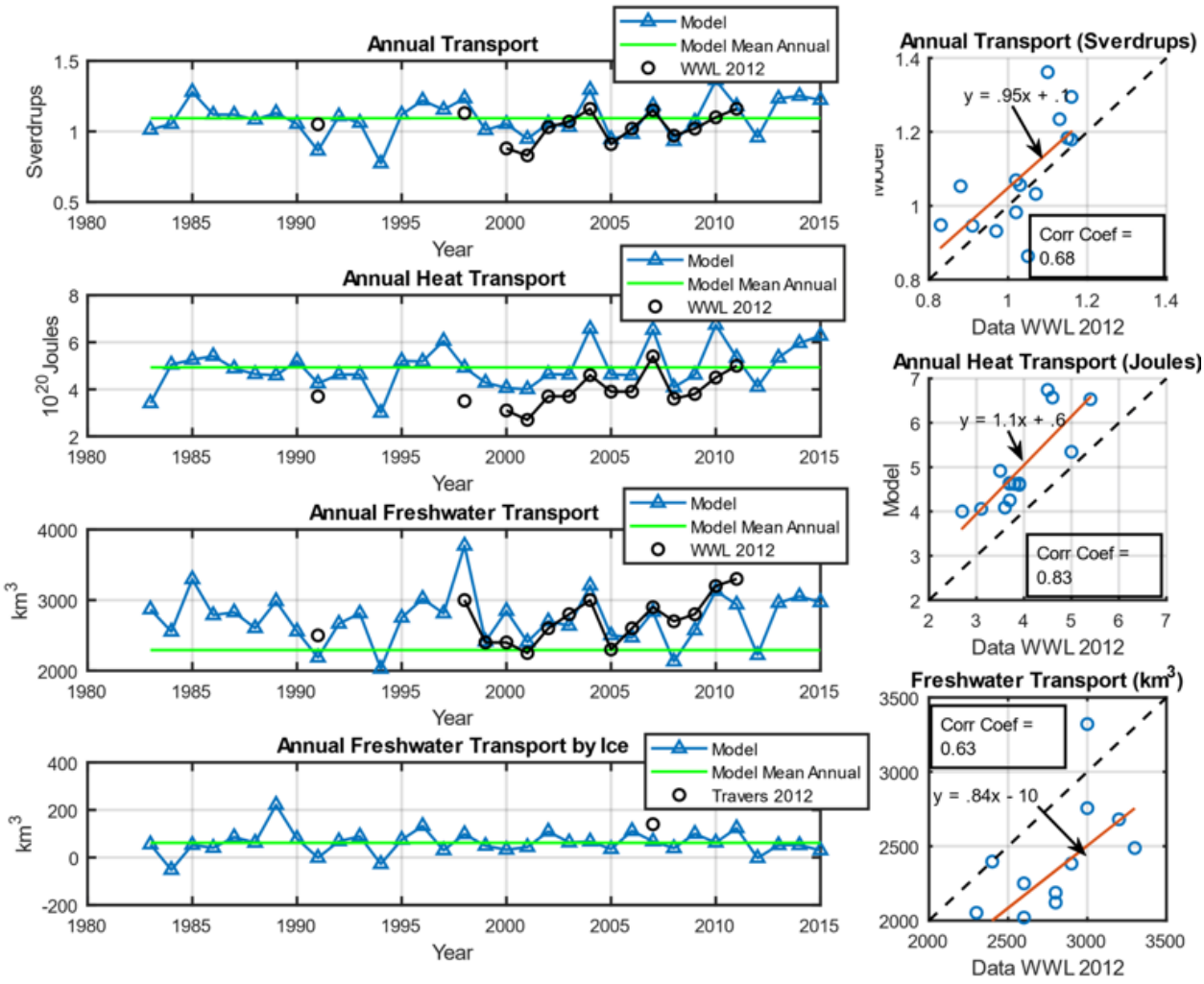

Figure 30: Comparison of annually averaged volume, heat, fresh water and ice freshwater transports (ordered from top to bottom, respectively) as depicted by the PAROMS model and observations. Time series are shown at the left over 1983-2015; scatterplots of the volume, heat and fresh water transports are shown in the right-hand column along with the regression equations and correlation coefficients. Abbreviation: WWL 2012 refers to Woodgate et al. [2012].

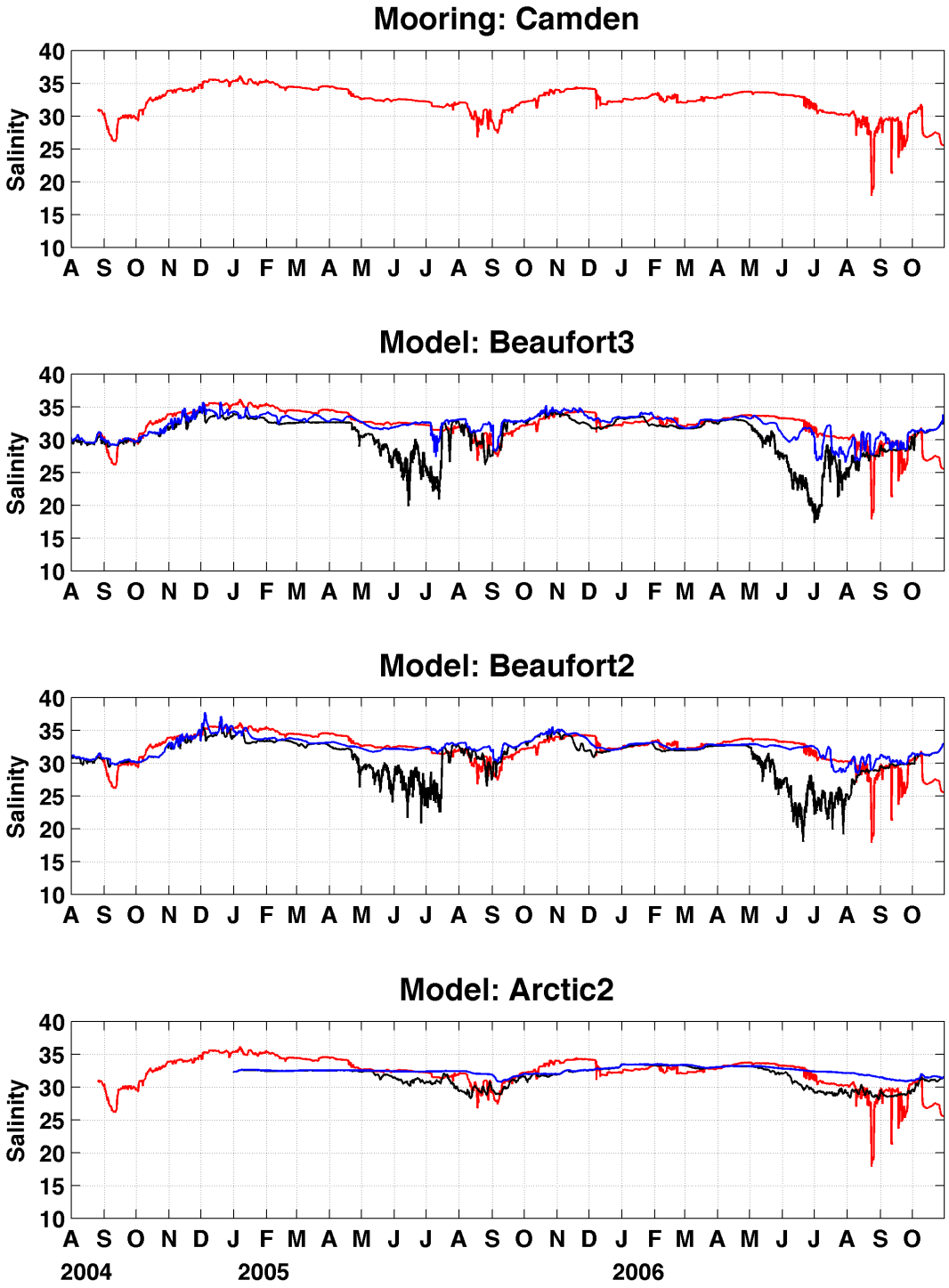

Figure 31: Comparison of observed (red, all rows) and modeled salinity at the Camden Bay mooring site. Model traces show salinity at the sea surface (black) and at the seafloor (blue). The observed salinity is measured within one meter of the seafloor. All fields have been smoothed with a 35-hour low-pass Butterworth filter to remove tides and other high-frequency fluctuations.

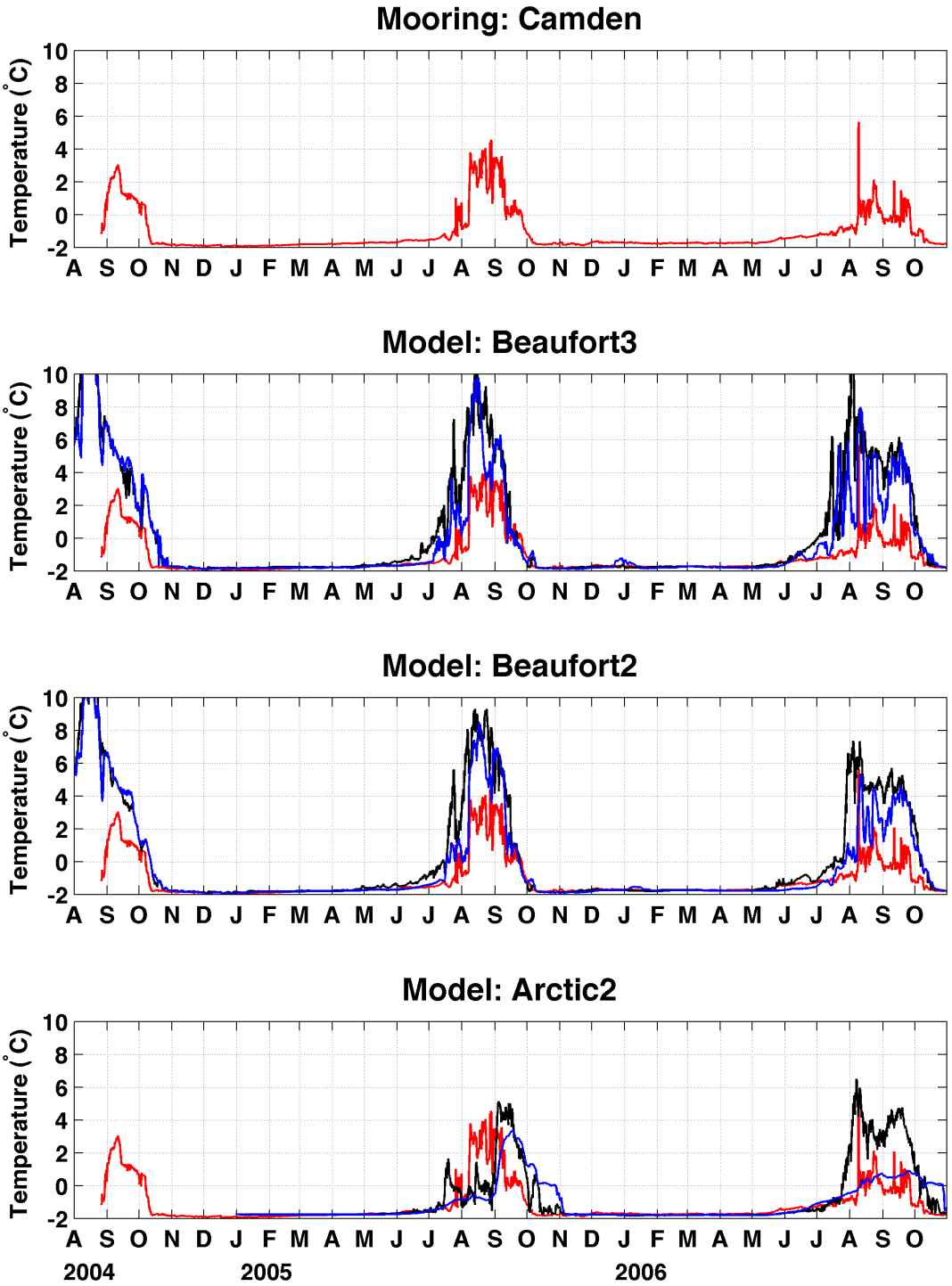

Figure 32: Comparison of observed (red, all rows) and modeled temperature at the Camden Bay mooring site. Model traces show temperature at the sea surface (black) and at the seafloor (blue) for the Beaufort2 (second row), Beaufort3 (third row) and Arctic2 (bottom row) models. The observed temperature is measured within one meter of the seafloor. All fields have been smoothed with a 35-hour low-pass Butterworth filter to remove tides and other high-frequency fluctuations.

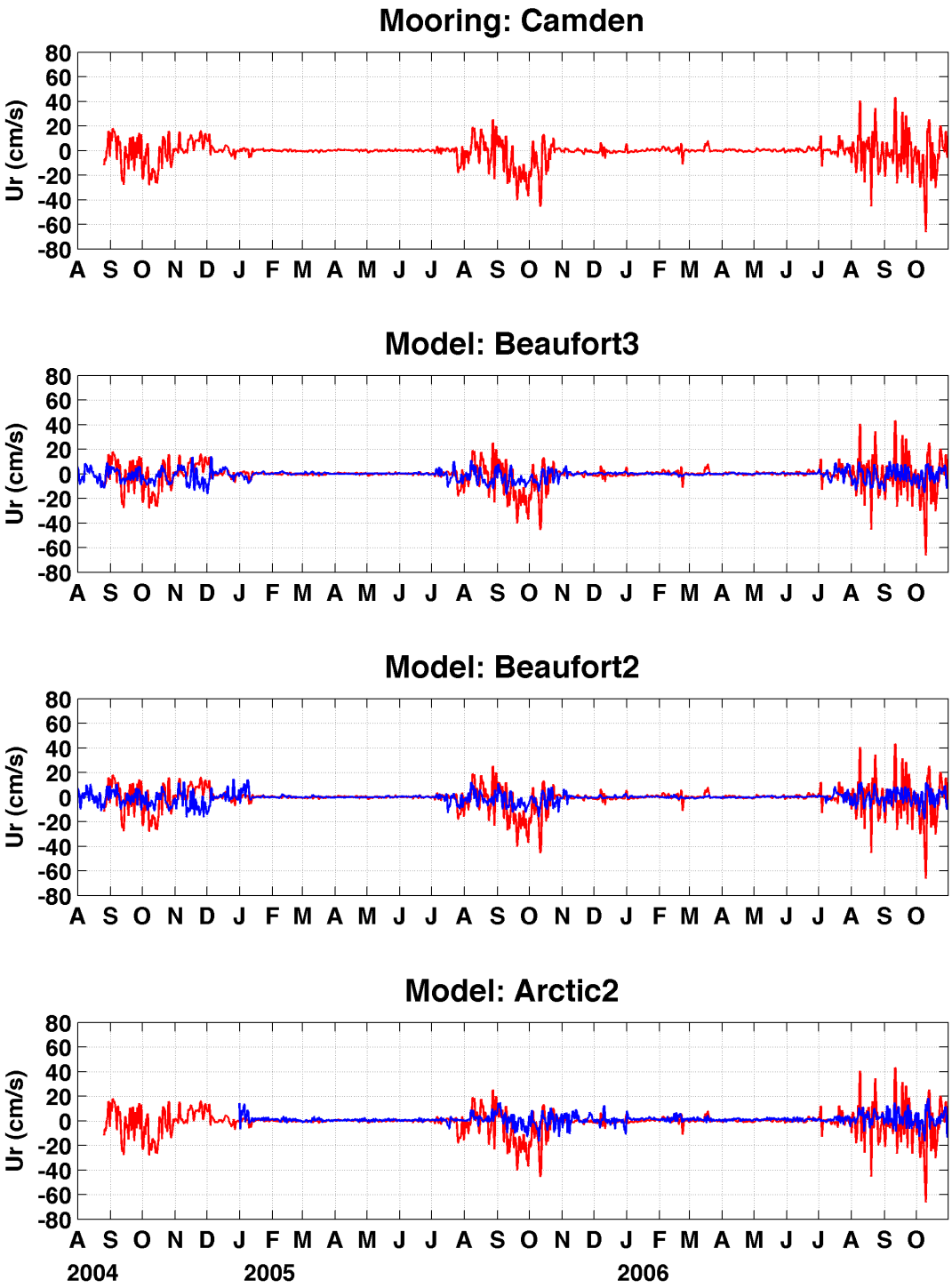

Figure 33: Comparison of observed (red, all rows) and modeled (blue) water column averaged along-shelf currents at the Camden Bay mooring site for the Beaufort2 (second row), Beaufort3 (third row) and Arctic2 (bottom row) models. All fields have been smoothed with a 35-hour low-pass Butterworth filter to remove tides and other high-frequency fluctuations.

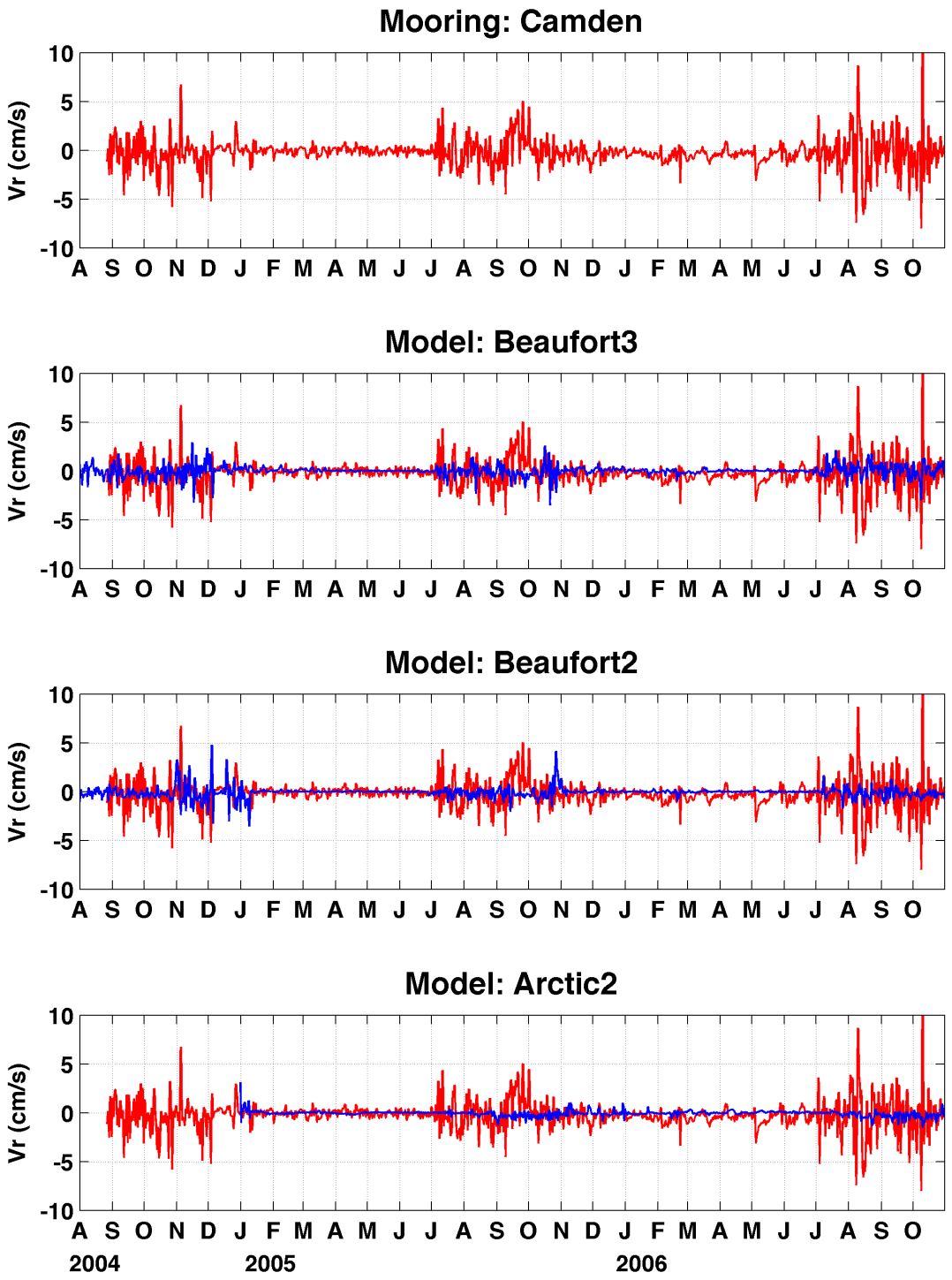

Figure 34: Comparison of observed (red, all rows) and modeled (blue) water column averaged cross-shelf currents at the Camden Bay mooring site for the Beaufort2 (second row), Beaufort3 (third row) and Arctic2 (bottom row) models. All fields have been smoothed with a 35-hour low-pass Butterworth filter to remove tides and other high-frequency fluctuations.

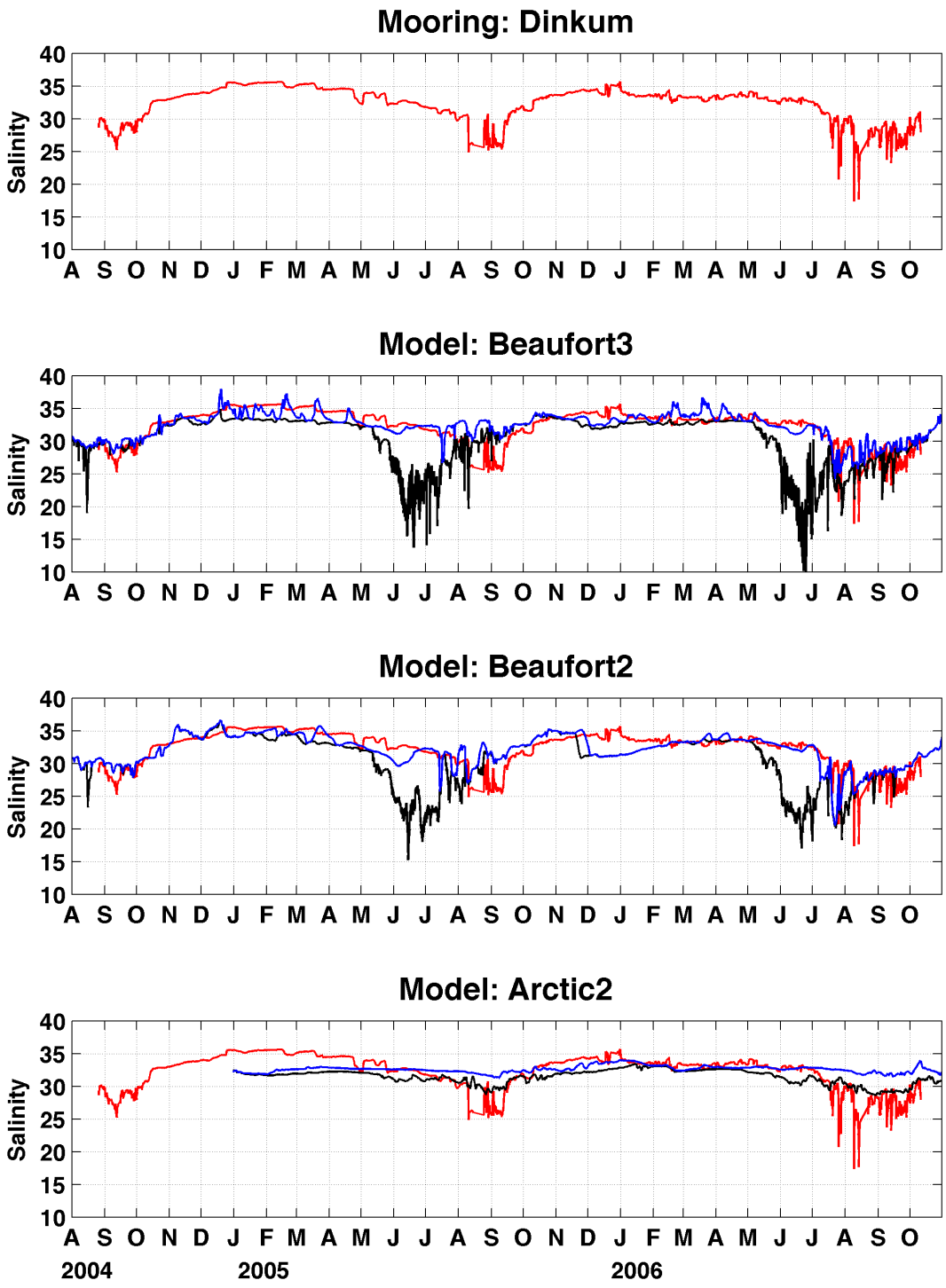

Figure 35: Comparison of observed (red, all rows) and modeled salinity at the Dinkum mooring site. Model traces show salinity at the sea surface (black) and at the seafloor (blue). The observed salinity is measured within one meter of the seafloor. All fields have been smoothed with a 35-hour low-pass Butterworth filter to remove tides and other high-frequency fluctuations.

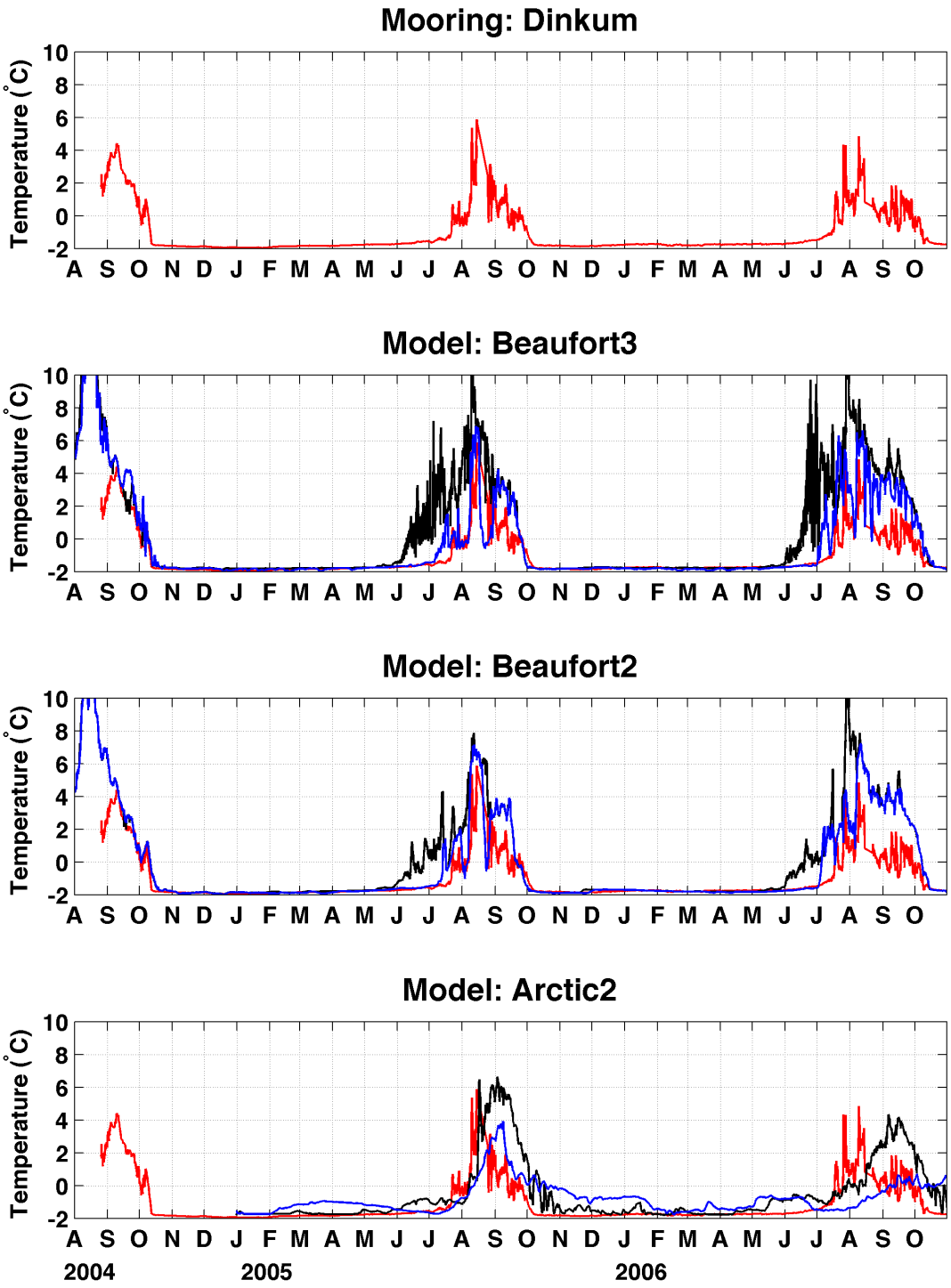

Figure 36: Comparison of observed (red, all rows) and modeled temperature at the Dinkum mooring site. Model traces show temperature at the sea surface (black) and at the seafloor (blue) for the Beaufort2 (second row), Beaufort3 (third row) and Arctic2 (bottom row) models. The observed temperature is measured within one meter of the seafloor. All fields have been smoothed with a 35-hour low-pass Butterworth filter to remove tides and other high-frequency fluctuations.

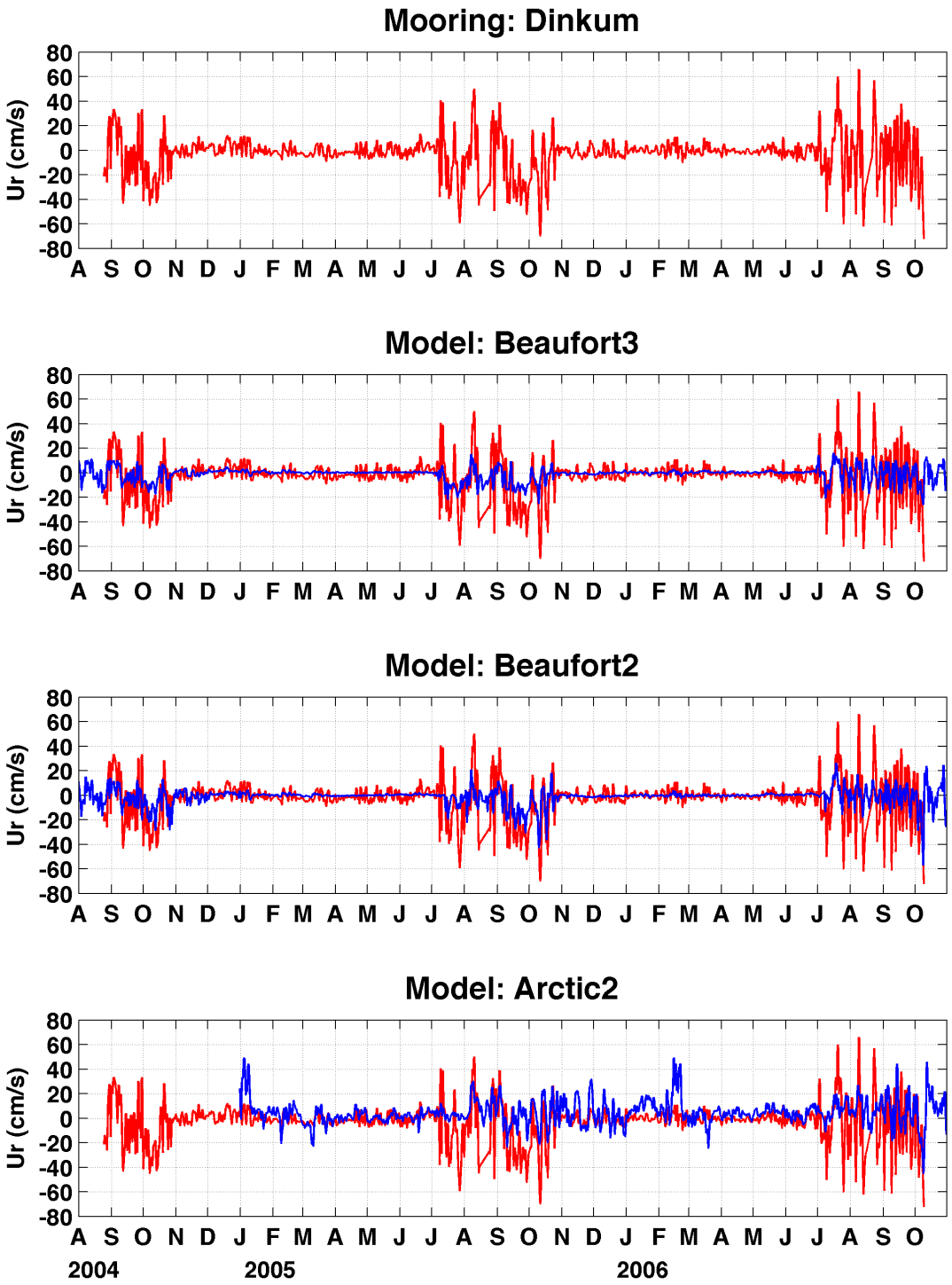

Figure 37: Comparison of observed (red, all rows) and modeled (blue) water column averaged along-shelf currents at the Dinkum mooring site for the Beaufort2 (second row), Beaufort3 (third row) and Arctic2 (bottom row) models. All fields have been smoothed with a 35-hour low-pass Butterworth filter to remove tides and other high-frequency fluctuations.

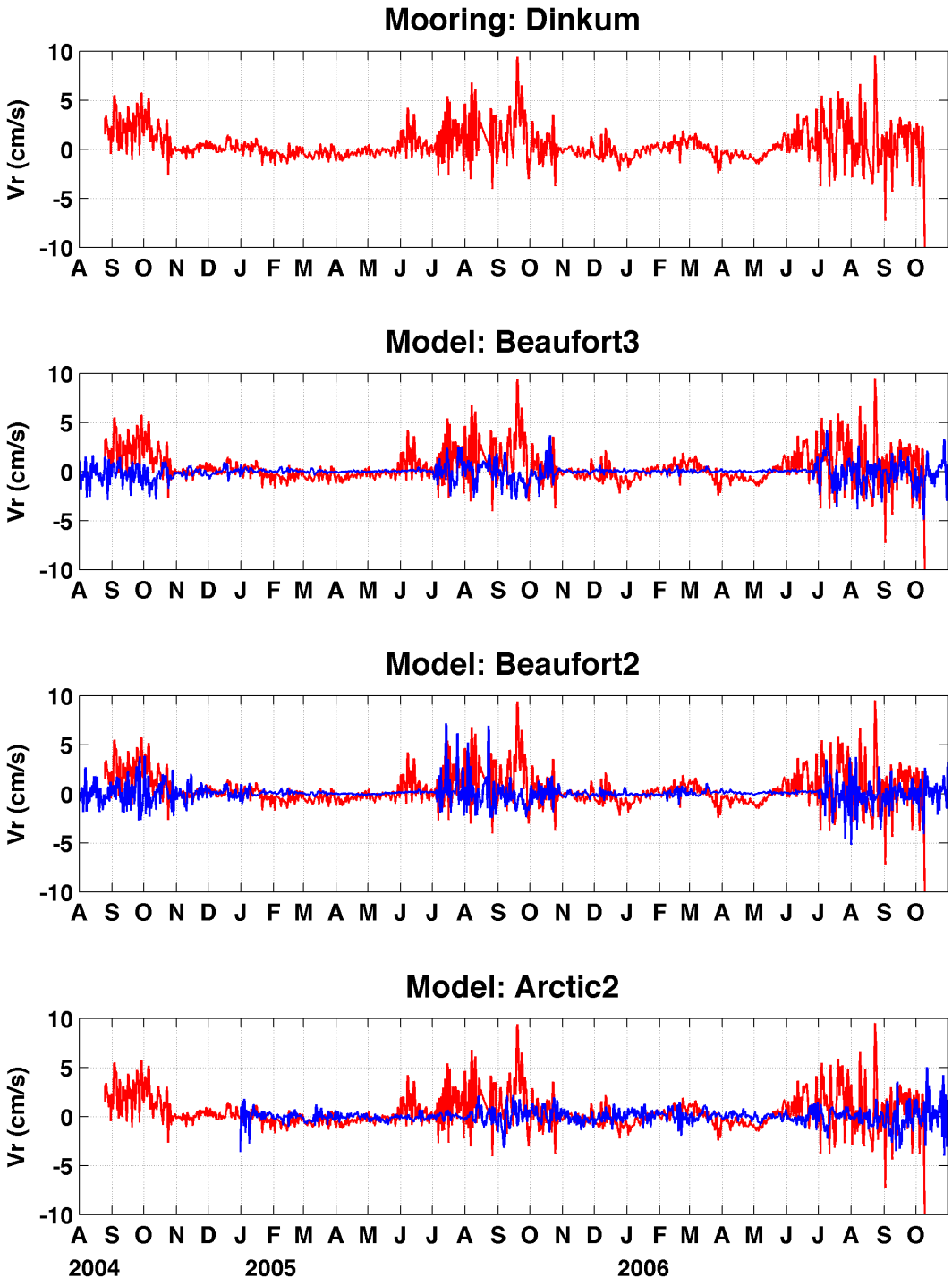

Figure 38: Comparison of observed (red, all rows) and modeled (blue) water column averaged cross-shelf currents at the Dinkum mooring site for the Beaufort2 (second row), Beaufort3 (third row) and Arctic2 (bottom row) models. All fields have been smoothed with a 35-hour low-pass Butterworth filter to remove tides and other high-frequency fluctuations.

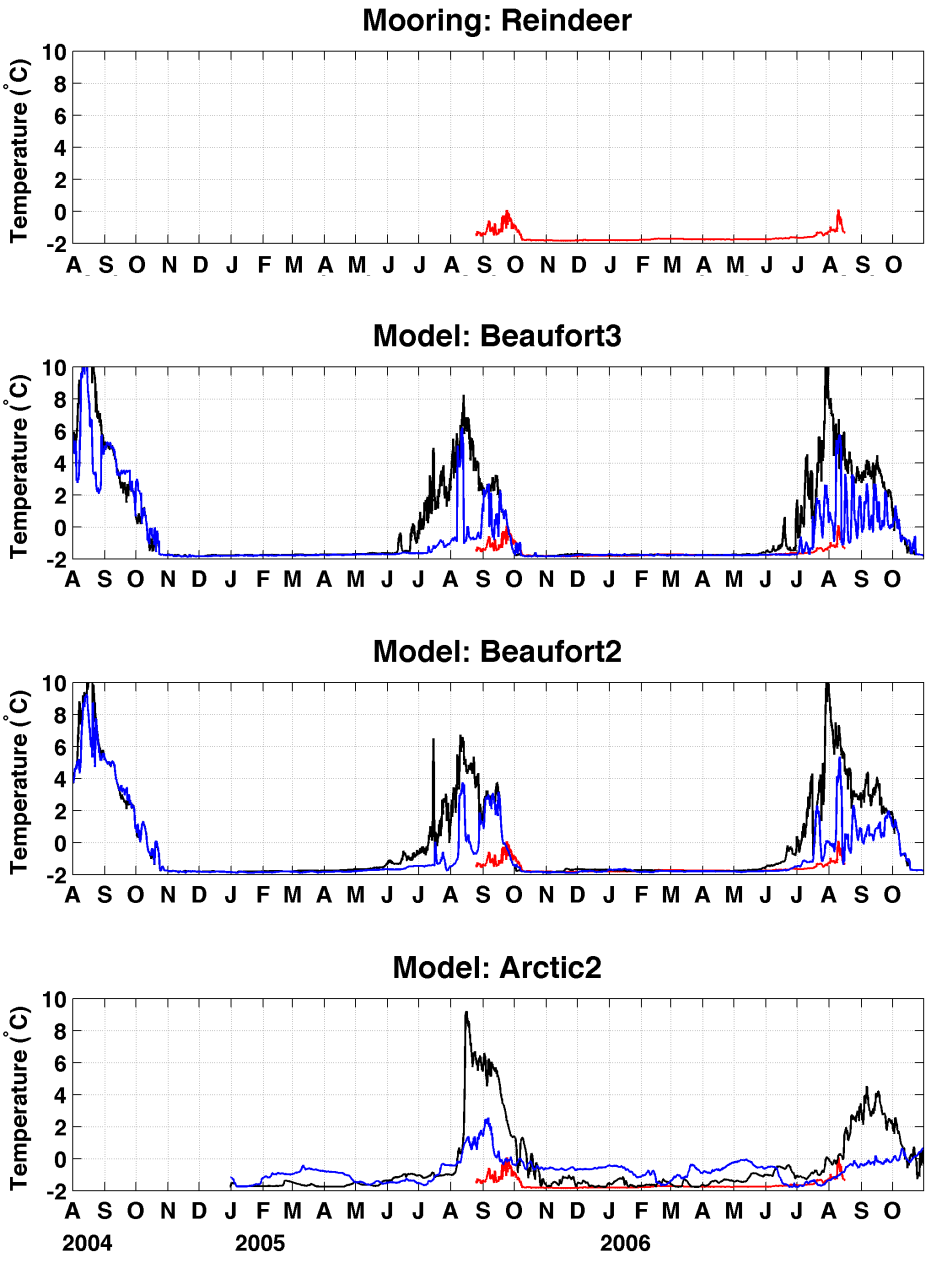

Figure 39: Comparison of observed (red, all rows) and modeled temperature at the Reindeer mooring site. Model traces show temperature at the sea surface (black) and at the seafloor (blue) for the Beaufort2 (second row), Beaufort3 (third row) and Arctic2 (bottom row) models. The observed temperature is measured within one meter of the seafloor. All fields have been smoothed with a 35-hour low-pass Butterworth filter to remove tides and other high-frequency fluctuations.

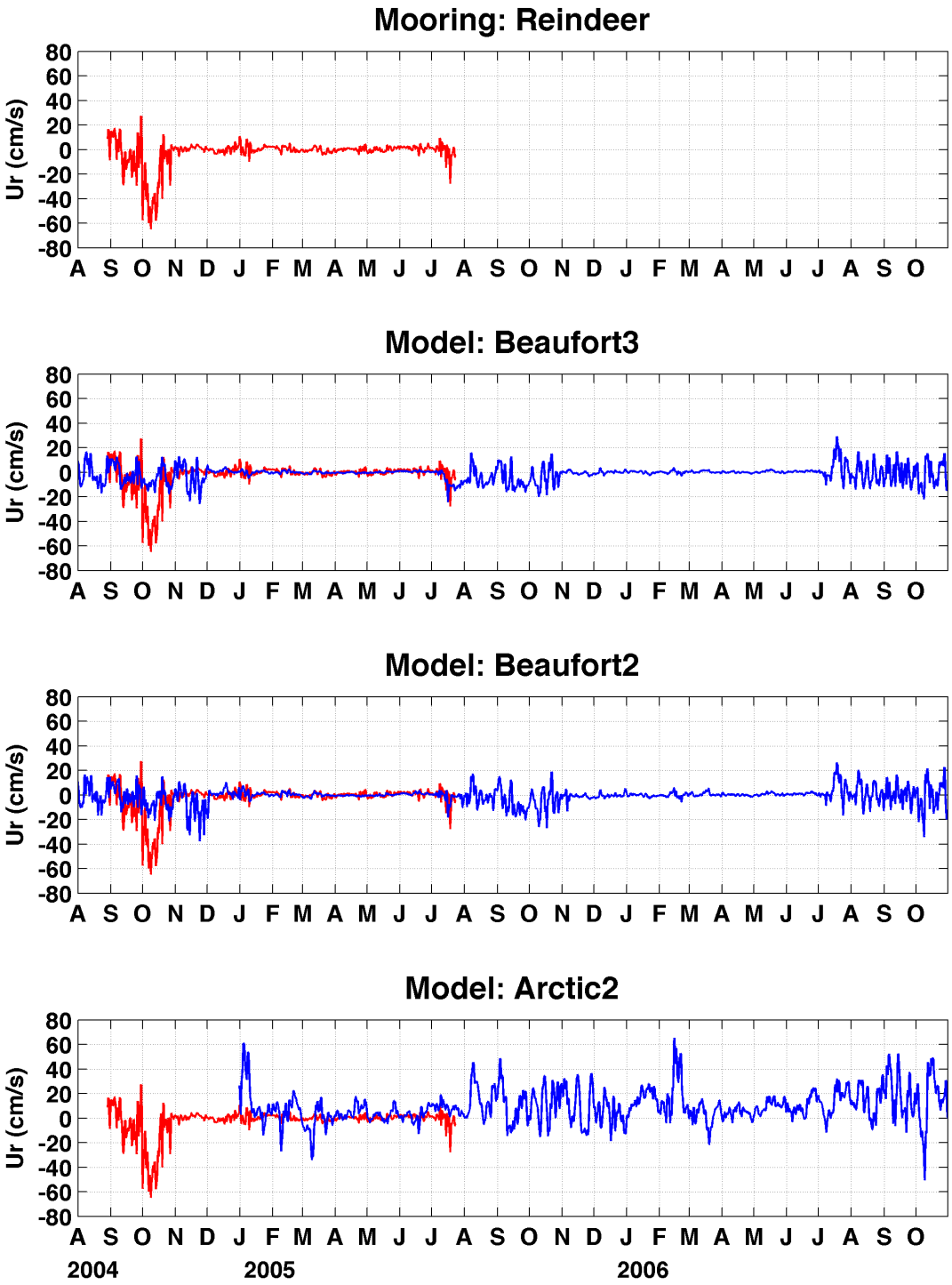

Figure 40: Comparison of observed (red, all rows) and modeled (blue) water column averaged along-shelf currents at the Reindeer mooring site for the Beaufort2 (second row), Beaufort3 (third row) and Arctic2 (bottom row) models. All fields have been smoothed with a 35-hour low-pass Butterworth filter to remove tides and other high-frequency fluctuations.

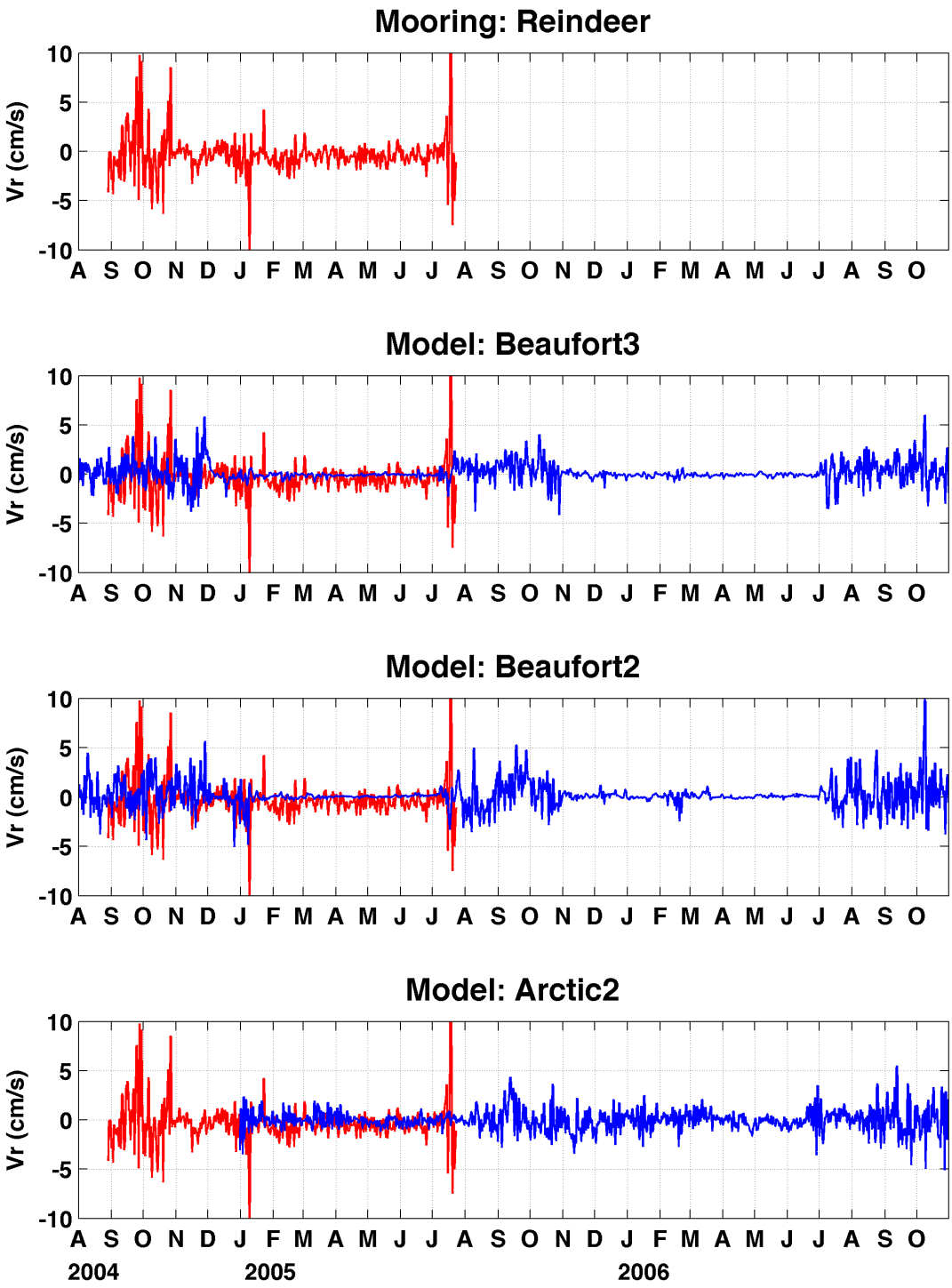

Figure 41: Comparison of observed (red, all rows) and modeled (blue) water column averaged cross-shelf currents at the Reindeer mooring site for the Beaufort2 (second row), Beaufort3 (third row) and Arctic2 (bottom row) models. All fields have been smoothed with a 35-hour low-pass Butterworth filter to remove tides and other high-frequency fluctuations.

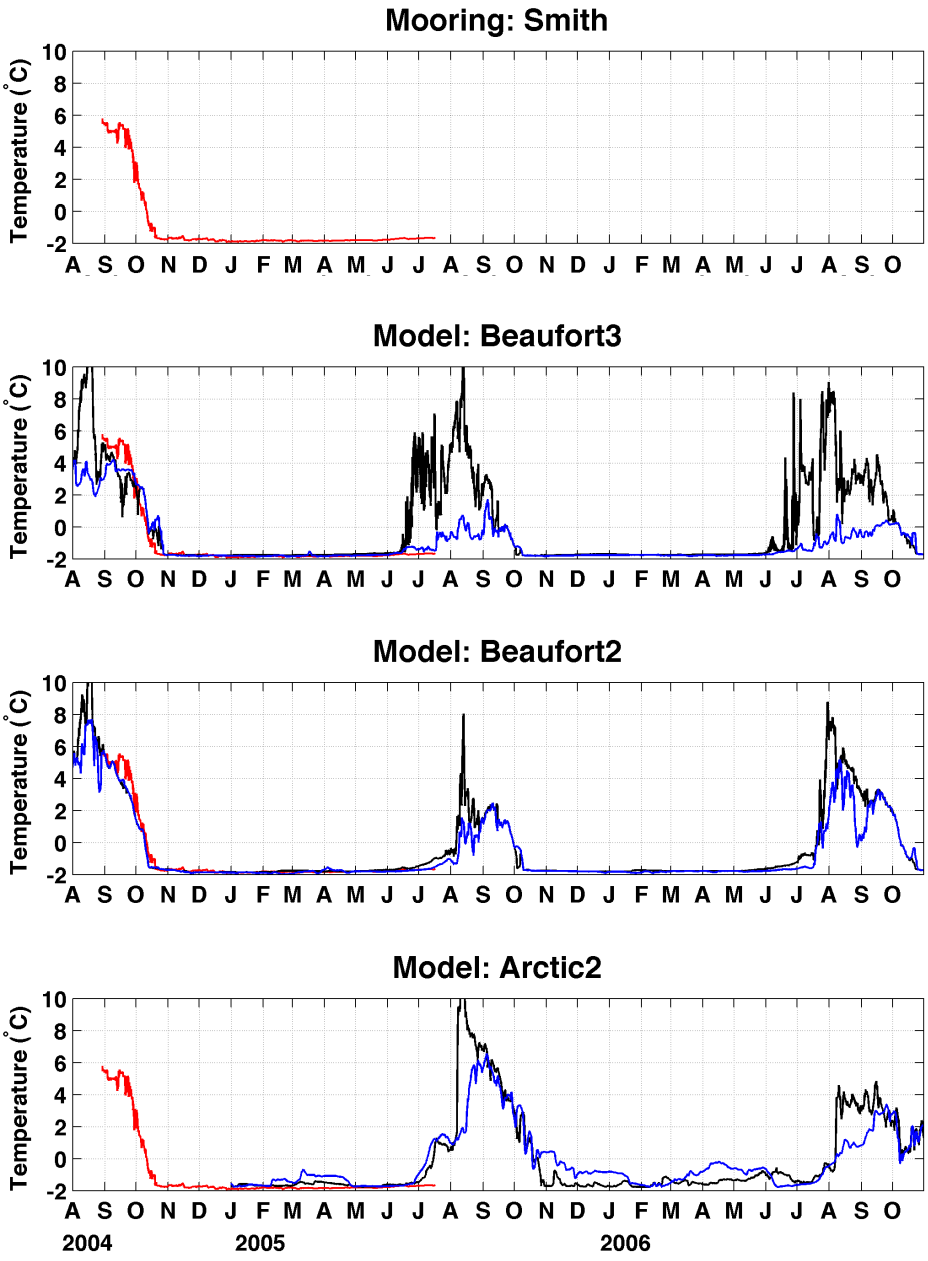

Figure 42: Comparison of observed (red, all rows) and modeled temperature at the Smith Bay mooring site. Model traces show temperature at the sea surface (black) and at the seafloor (blue) for the Beaufort2 (second row), Beaufort3 (third row) and Arctic2 (bottom row) models. The observed temperature is measured within one meter of the seafloor. All fields have been smoothed with a 35-hour low-pass Butterworth filter to remove tides and other high-frequency fluctuations.

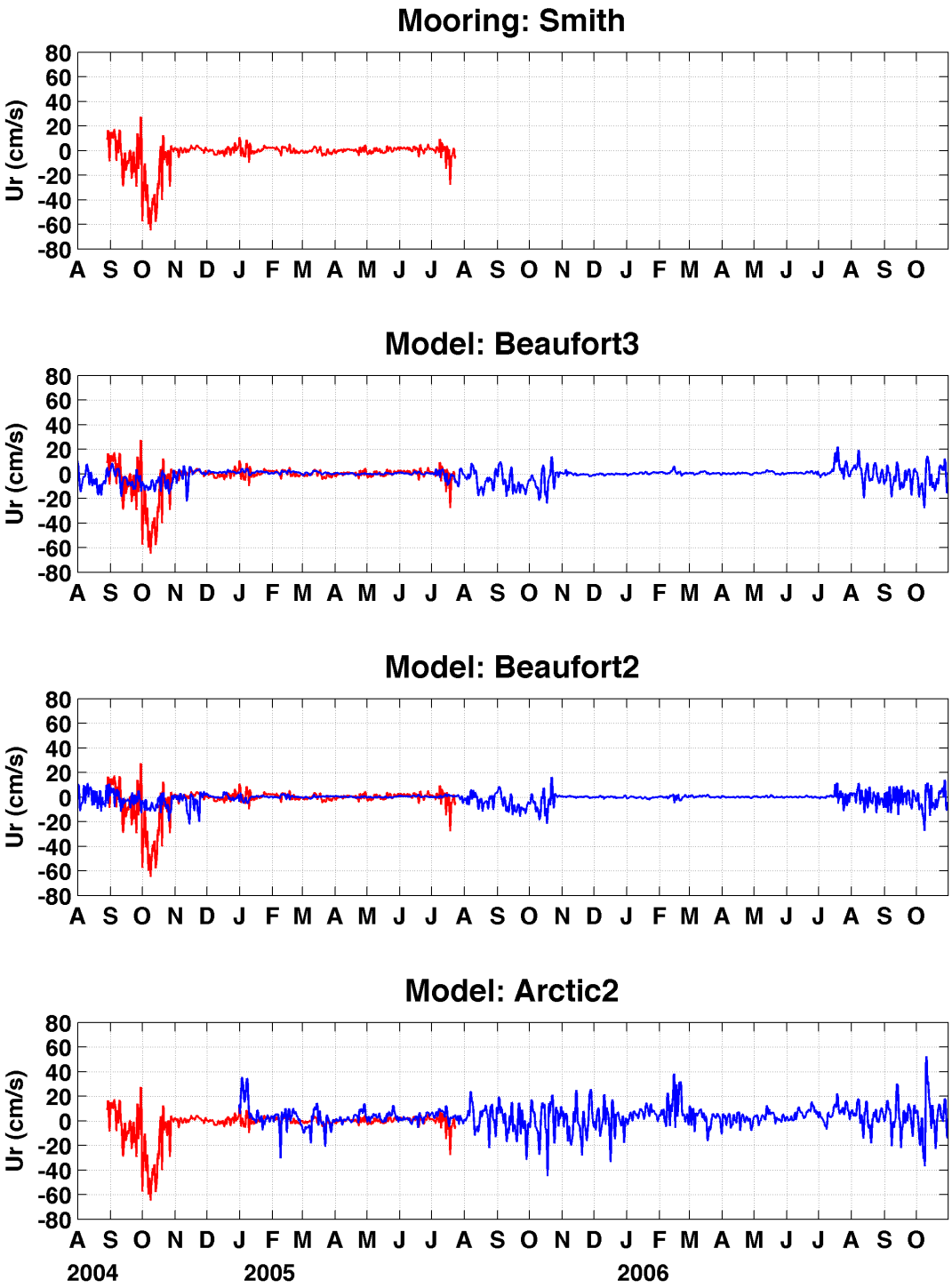

Figure 43: Comparison of observed (red, all rows) and modeled (blue) water column averaged along-shelf currents at the Smith Bay mooring site for the Beaufort2 (second row), Beaufort3 (third row) and Arctic2 (bottom row) models. All fields have been smoothed with a 35-hour low-pass Butterworth filter to remove tides and other high-frequency fluctuations.

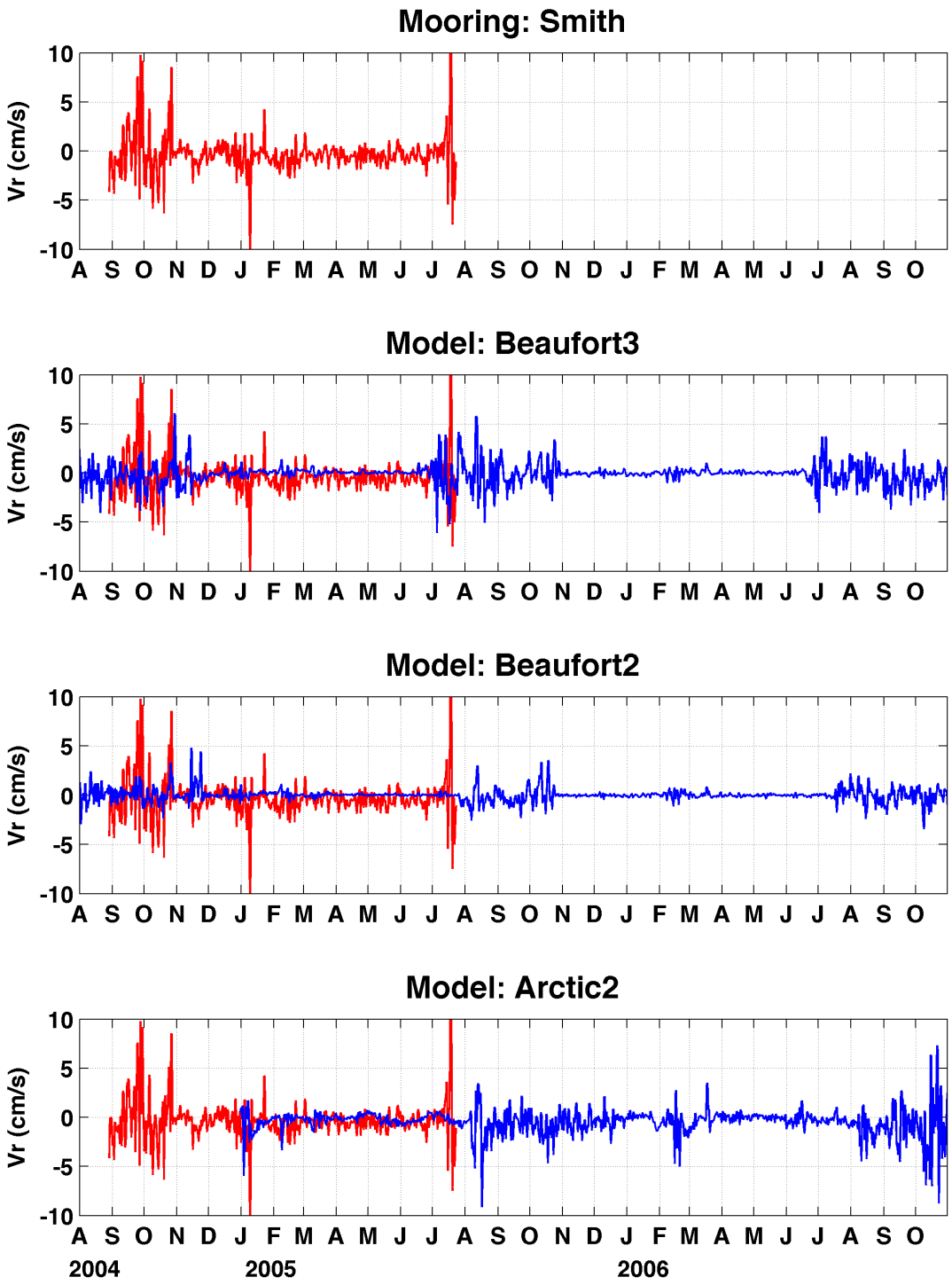

Figure 44: Comparison of observed (red, all rows) and modeled (blue) water column averaged cross-shelf currents at the Smith Bay mooring site for the Beaufort2 (second row), Beaufort3 (third row) and Arctic2 (bottom row) models. All fields have been smoothed with a 35-hour low-pass Butterworth filter to remove tides and other high-frequency fluctuations.

of these could be related to features such as river plumes, which the model is capable of reproducing only in a statistical sense as the river forcing fields provide a climatology and not an inter-annually varying discharge field. The PAROMS model provides a salinity time series at the mooring sites that approximates the annual average, but the amplitude of the this model's salinity is appreciably reduced in comparison to the observations and the two nested models. The model's surface salinity shows freshening events during summer and fall months that are much fresher than the near-bottom salinity measurements reveal; we lack suitable time series of salinity at the surface to adequately evaluate the model's behavior for this field. The temperature comparisons (Figures 32, 36, 42 and 39) show an observed annual cycle that is tracked relatively closely by all of the models, though like the salinity field, the higher-resolution nested models perform better than the coarser Pan-Arctic model. The observed water column cooling that occurs each fall is reproduced with a synchronous decline of temperature in each of the models, although the Pan-Arctic model for the farther offshore mooring (Reindeer) remains somewhat stratified whereas the observations and the nested models suggest an isothermal water column at the freezing point. This behavior of the Pan-Arctic model is directly related to the less accurate bathymetry employed by this model's configuration.

Examination of the velocity figures (Figures 33, 34, 37, 38, 40, 41, 43, nad 44) reveals that the nested models produce a materially useful improvement of the predictions in comparison to the Pan-Arctic model, but in general the velocity magnitudes are slightly underestimated by all of the models. Like the observations, the models reveal a strongly two-season character of the flow field: weak currents during winter months when landfast ice is present, and energetic with relatively large amplitude current fluctuations when the landfast ice is absent.

Ship-based hydrography from the BOEM-funded 2011 Beaufish study provides data for comparing the temperature and salinity fields at the surface and near the seafloor. Upwelling-favorable winds during this month may have been responsible for relatively cool and salty water observed on the eastern and inshore side of the observed stations.

The models used in this project tend to compute temperatures that are similar to those observed within the bounds of the data collected (Figure 45). Close to shore and outside of the station grid of the ship samples, the models all exhibit temperatures at the surface and the seafloor that are warmer than farther offshore. In this region the higher-resolution models (Beaufort 2 and 3) depict temperatures that are appreciably warmer than those computed by the Pan-Arctic model. We note that some broad-scale features seen in the data also appear to be represented in the modeled fields. For example, the surface temperatures are cooler closer to the coast and in the eastern portion of the domain. This feature also appears in the model, although with a diminished offshore extent. The warmest waters observed, and modeled, are in the far west of the domain near Barrow Canyon,

The near-bottom salinities on the shelf as depicted by the models are a bit saltier than those observed (Figure 46). In the case of the Pan-Arctic model, the on-coast displacement of the shelf break is partly responsible for the mis-match. In the case of the nested models, it appears that some freshwater is held close to the coast by a frontal system. At the surface, the

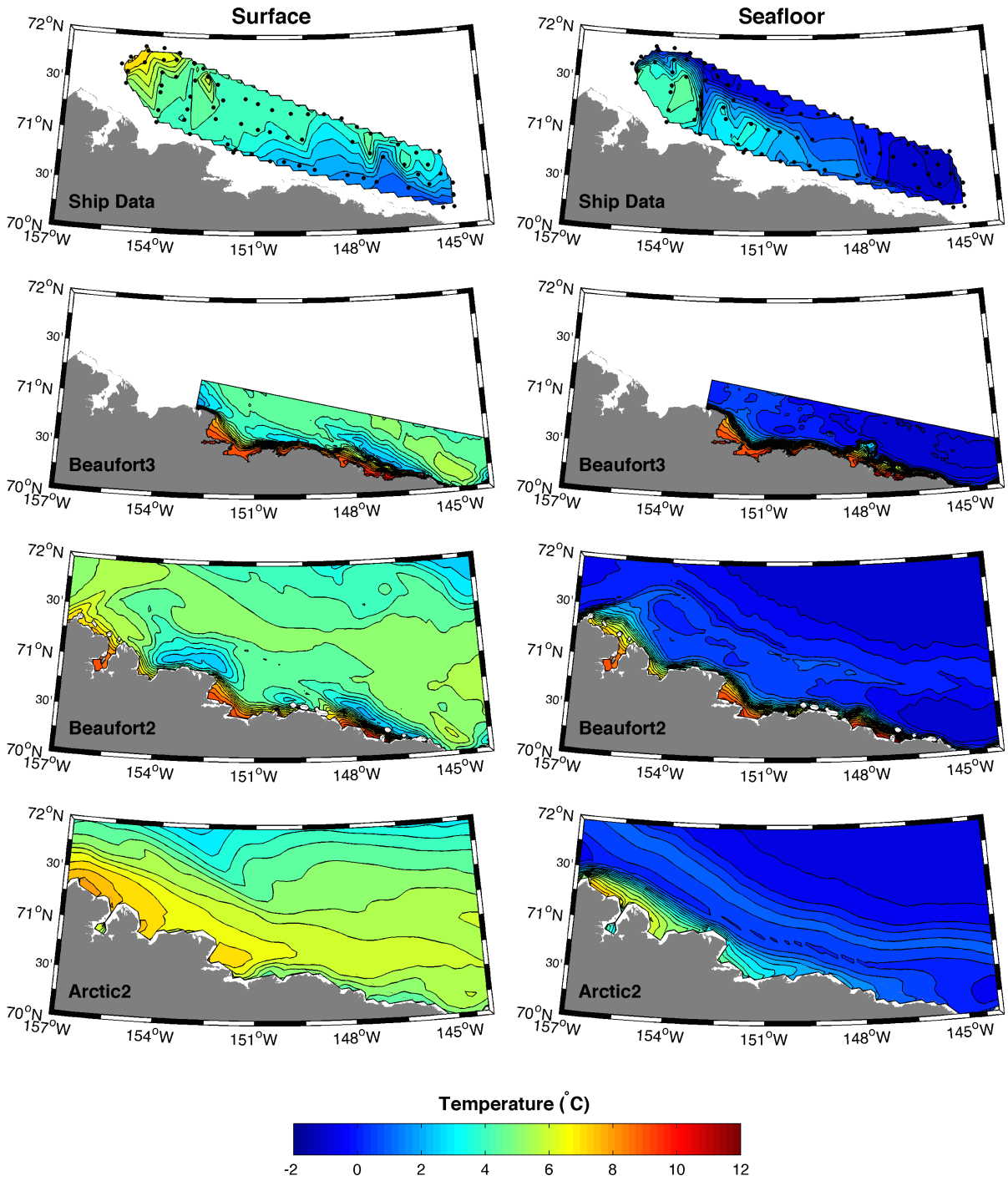

Figure 45: Comparison of ship observations (top row) of temperature to modeled ocean temperature at the sea surface (left column) and the seafloor (right column). The Beaufort2, Beaufort3 and Arctic2 models are in rows 2, 3 and 4, respectively. Circles in the top row panels denote CTD cast locations.

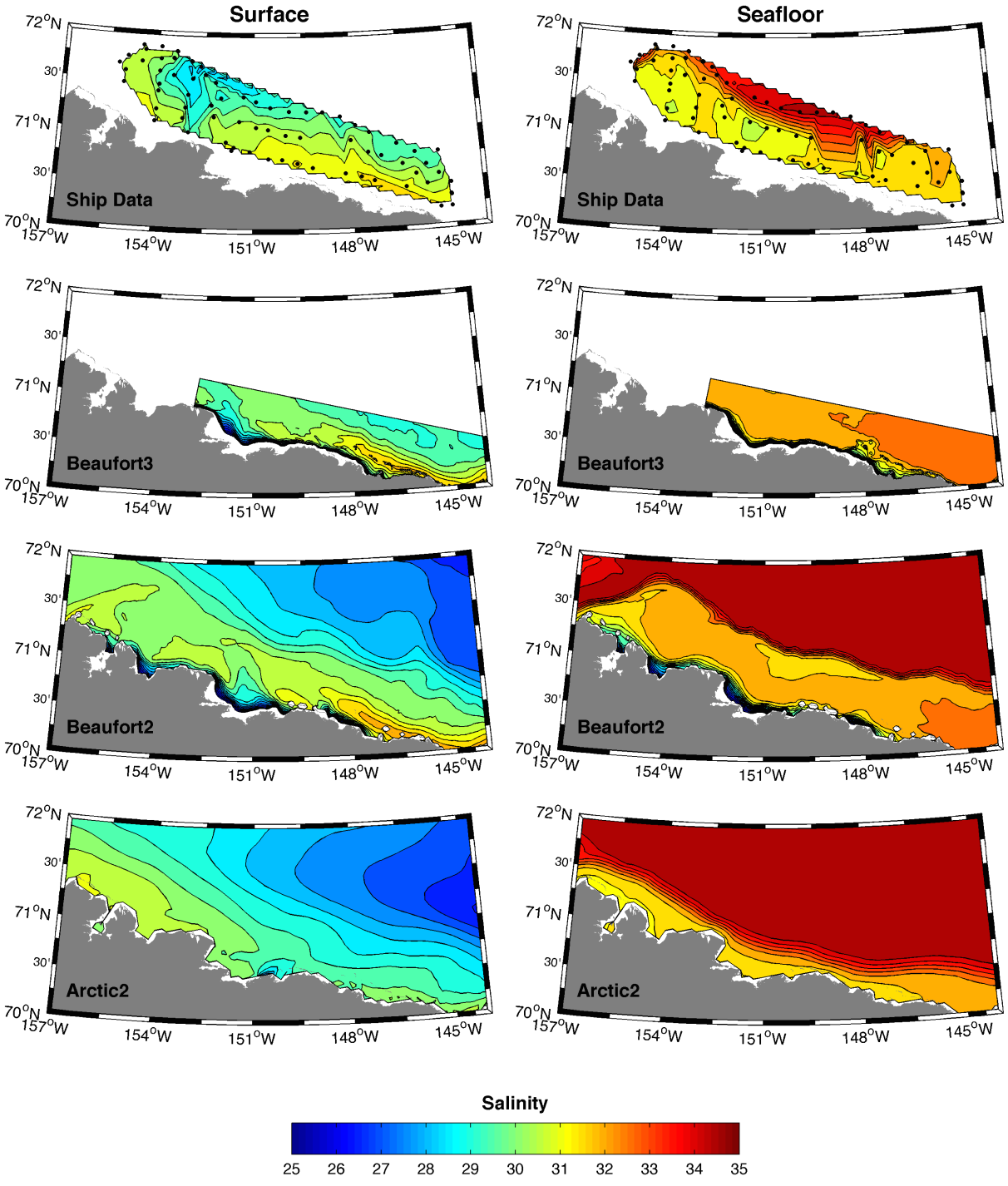

Figure 46: Comparison of ship observations (top row) of salinity to modeled ocean salinity at the sea surface (left column) and the seafloor (right column). The Beaufort2, Beaufort3 and Arctic2 models are in rows 2, 3 and 4, respectively. Circles in the top row panels denote CTD cast locations.

modeled salinities are extremely close to those observed, especially in the eastern portion of the domain (including the upwelling signal noted above). The models predict fresher waters offshore, and a hint of such waters are visible in the western portion of the observed grid.

Comparison of observed and modeled sea ice concentrations show that the Arctic2 Pan-Arctic model (Figures 47 and 48) reproduces 58% of the ice area variance across the Pan-Arctic domain as a whole, 88% of the variance in the Beaufort2 domain, and 64% in the nearshore Beaufort3 domain. In contrast, the Beaufort2 model captures 61% of the variance of the ice area variance across its entire domain and the Beaufort3 model captures 44% of the variance. We note that the resolution of the satellite data (25 km) is coarser than any of the models and this characteristic of the passive satellite ice concentration measurements provides a limit to our ability to assess the fidelity of the model's ice field. This latter point is illustrated by the panels shown in Figure 49, which clearly shows the difference between the pixel size of the observations in relation to the ice model resolution. Figure 50 provides a high-resolution thermal satellite image in the Chukchi-Beaufort region in order to illustrate some of the fine-scale ice features that are fully unresolved by the passive microwave sensor.

The newly implemented landfast ice parameterization provides a means by which the models can dynamically grow and destroy extensive regions of landfast ice. Initial comparisons show that the models can reproduce the timing and magnitude of landfast ice extent.

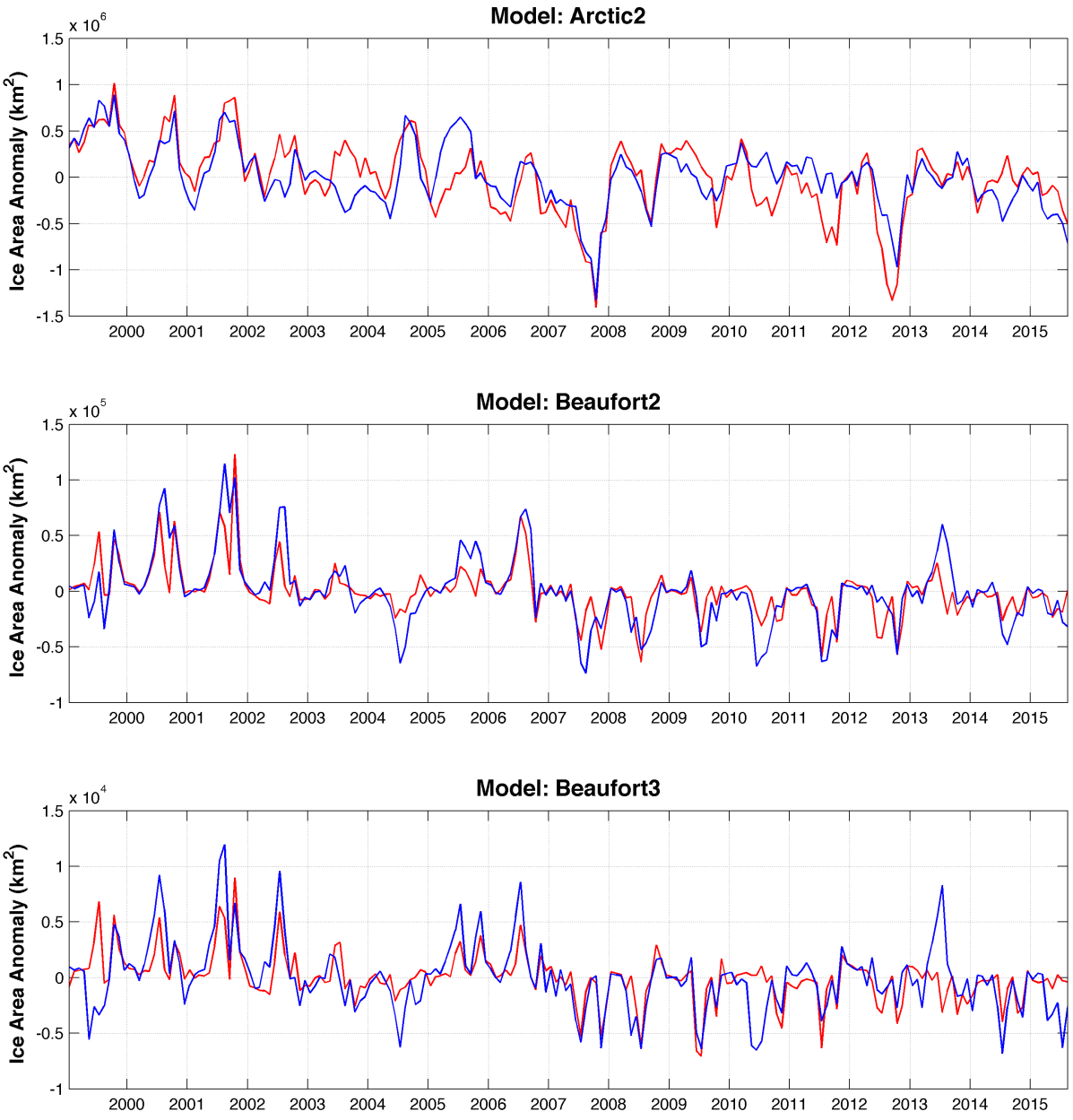

Figure 47: Time series of the Arctic2 (top), Beaufort2 (middle) and Beaufort3 (bottom) models in reproducing the mean ice area anomalies for each of their respective grids.

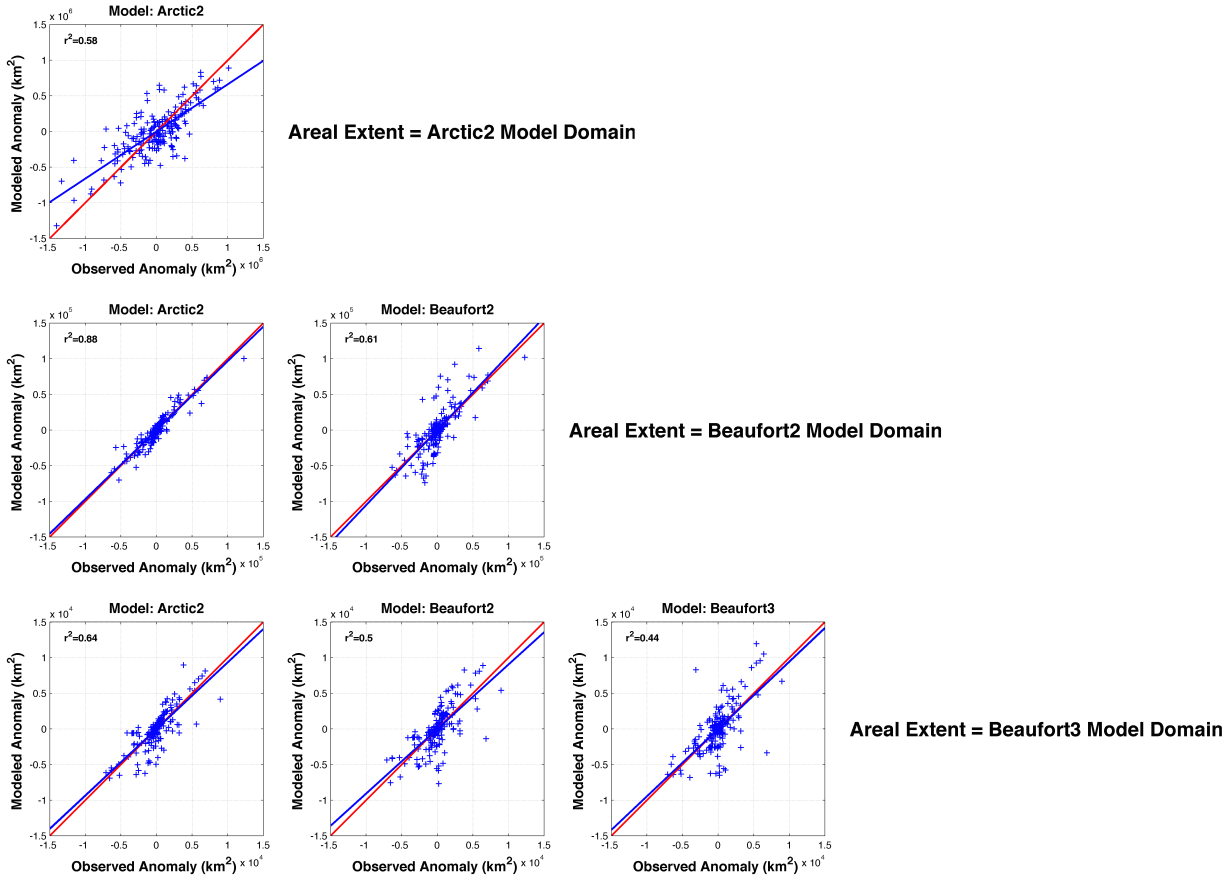

Figure 48: Correlation matrix of ice area anomalies for each of the three model for the Pan-Arctic model domain (top), the Beaufort2 model domain (middle) and Beaufort3 model domain (bottom). The model data that comprise the comparisons are the coarse Pan-Arctic model (left), the medium-resolution Beaufort2 model (center) and the fine-resolution Beaufort3 model (right).

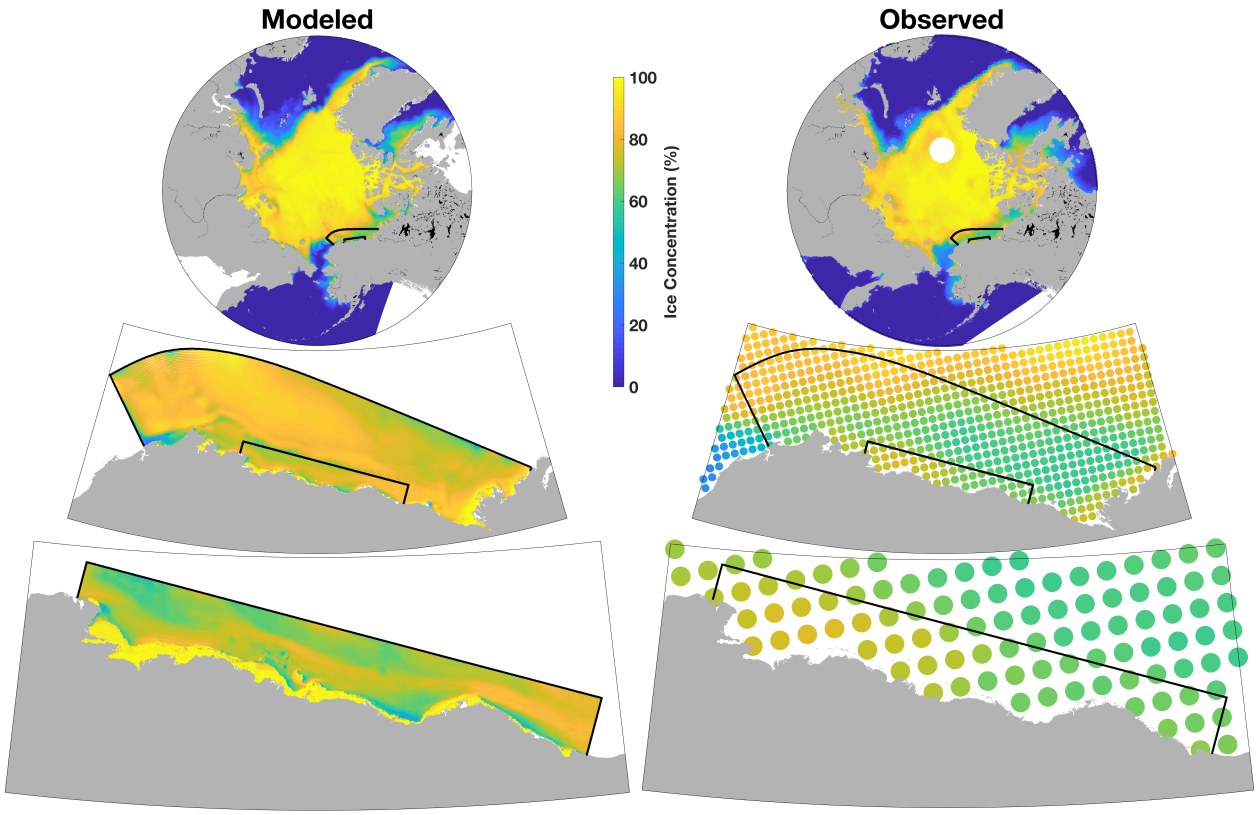

Figure 49: Comparison of modeled (left) and observed (right) ice concentration for the coarse (top), medium-resolution (middle) and fine-resolution (bottom) models.

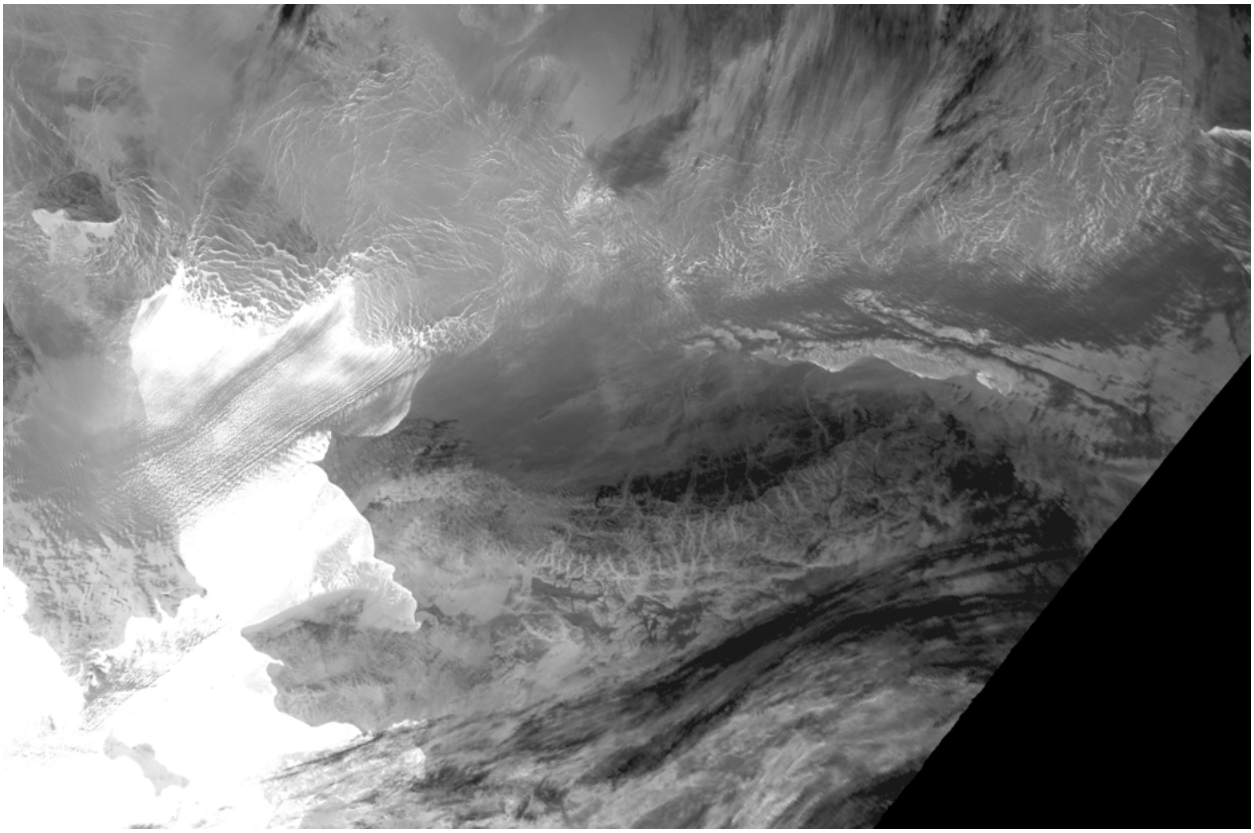

Figure 50: Thermal satellite image from 14 November 2012. Dark colors represent relatively cold temperatures, white colors show relatively warm (e.g., ocean water). The figure extends from Banks Island in the upper right to St Lawrence Island in the lower left. Leads in the ice pack show as thin bright lines between the light grey ice pack floes. Fog and clouds are dark grey smears that extend across land/ocean boundaries.

5 Summary remarks

This project has advanced our ROMS modeling capabilities in the Beaufort Sea, and more broadly, across the entire Arctic. Particular achievements include:

- Success at nesting high-resolution grids into a coarser model domain for a model setup that includes sea ice crossing the model interface boundary.
- Incorporation of a landfast ice field that grows and contracts with changing wind, ice, and oceanographic conditions.
- Forcing of the terrestrial river discharges through the sidewall boundaries with full momentum, heat, tracer and freshwater fluxes.

Evaluation of the models' performance show that the nested grids can provide an appreciably more accurate depiction than the coarser Pan-Arctic model, although even the broad-scale model is able to provide statistically significant predictive capacities for the sea surface elevation and ice fields and the heat, volume and freshwater fluxes. Performance of the highest-resolution model may be hampered by the lack of an accurate bathymetric elevation model for the nearshore Beaufort Sea. However, we note that even at 500 m resolution many of the barrier islands are not sufficiently resolved. The temporal and spatial resolution of datasets that are available for making robust model-data comparisons continues to be a limiting factor in assessing all aspects of the model's fidelity to the real ocean.

The results of this study suggest a number of avenues for further improving our ability to model the Beaufort shelf and for improving our understanding of the ocean currents and sea ice here. Recommendations for future advances for the circulation modeling of the Arctic seas include:

- Development of a high-resolution coastal discharge forcing field that specifies the terrestrial discharge at sub-km resolution in space and at daily or hourly resolution in time. Present options for coastal runoff forcing lag behind our ability to incorporate such datastreams in a realistic fashion.
- Collection of shelf-wide high-resolution bathymetric data for improving the underlying digital elevation model. Data in waters shoreward of the 20m isobaths, particularly those in and around the barrier islands should be the highest priorities.
- Additional experiments with the landfast ice algorithms are warranted in order to further optimize the suite of settings that result in the most realistic ice field.
- Despite the number and location limitations of available datasets for model evaluation, there are always additional analyses that hold promise for revealing physical processes that are important to a full understanding of the Beaufort shelf circulation. We recognize extensive opportunities for case-study investigations of individual events (e.g.

discrete storms) and processes (e.g., coastal upwelling) that would benefit from focused study.

Finally, we highlight the approach taken here, namely that of multiple nests starting with the relatively coarse basin scale model and ending in a very high-resolutoin coastal domain. This first clear advantage of this approach is the ability to integrate the circulation and sea ice dynamics in the region of interest at a very high-resolution for decadal timescales. This is simply not feasible for extended domains. Furthermore, by integrating the physics at different resolutions, this methodology, in effect, concentrates the effort and cost of the simulation where it is needed for particular objectives. The Pan-Arctic model is useful to generate the large-scale context–from storms to interannual and decadal variability–which is then successively passed on to the more regional models through the boundaries. At the higher resolutions, local details of the coastline and circulation (e.g., barrier islands, ocean turbulence) can then be integrated in the context provided by the large-scale model. The challenge is always the treatment of the dynamics at the model interfaces allowing the propagation of information, from shelf waves to moving ice. In this project, we made significant advances for nested modeling of coupled circulation-sea ice systems, which creates opportunity for the investigation of the physics and the ecosystems in this region.

References

K. Aagaard. The beaufort undercurrent. In P.W. Barnes, D.M. Schell, and E. Reimnitz, editors, *The Alaskan Beaufort Sea: Ecosystems and Environments*, pages 47–71. Academic Press, Orlando, Florida, 1984.

P. W. Barnes, D. M. Schell, E. Reimnitz, Jr., J. L .Wise, and L.D. Leslie, editors. *The Alaskan Beaufort Sea: Ecosystems and Environments*. Academic Press, Inc., 1984. 466 pp.

W.P. Budgell. Numerical simulation of ice-ocean variability in the barents sea region: Towards dynamical downscaling. *Ocean Dynamics*, 2005. doi:10.1007/s10236-005-0008-3.

E. C. Carmack, R. W. Macdonald, and J. E. Papdakis. Water mass structure and boundaries in the mackenzie shelf estuary. *J. Geophys. Res.*, 94:18043–19055, 1989.

J. A. Carton, B. S. Giese, and S. A. Grodsky. Sea level rise and the warming of the oceans in the soda ocean reanalysis. *J. Geophys. Res.*, 110, 2005. doi:10.1029/2004JC002817.

A. Dai, T. Qian, K. E. Trenberth, and J. D Milliman. Changes in continental freshwater discharge from 1948–2004. *J. CLimate*, 22:2773–2791, 2009. doi:10.1175/2008JCLI2592.1.

S. L. Danielson, E. N. Curchitser, K. S. Hedstrom, T. Weingartner, and P. Stabeno. On ocean and sea ice modes of variability in the bering sea. *jgr*, 116(C12034), 2011. doi:doi:10.1029/2011JC007389.

S. L. Danielson, E. L. Dobbins, M. Jakobsson, M. J. Johnson, T. J. Weingartner, W. J. Williams, and Y. Zarayskaya. Sounding the northern seas. *Eos*, 96, 2016. doi:10.1029/2015EO040975.

G. D. Egbert and S. Y. Erofeeva. Efficient inverse modeling of barotropic ocean tides. *J. Atmos. Ocean. Tech.*, 19:183–204, 2002.

C. W. Fairall, E. F. Bradley, J. E. Hare, A. A. Grachev, and J. B. Edson. Bulk parameterization of air-sea fluxes: Updates and verification for the coare algorithm. *J. Climate*, 16: 571–591, 2003.

C. K. Guay and K. K. Falkner. A survey of dissolved barium in the estuaries of major arctic rivers and adjacent seas. *Cont. Shelf Res.*, 8:859–882, 1998.

K. S. Hedstrom. Technical manual for a coupled sea-ice/ocean circulation model (version 5). Technical Report OCS Study BOEM 2018-007, U.S. Department of Interior, Bureau of Ocean Energy Management, Alaska OCS Region, Anchorage, Alaska, 2018.

E. C. Hunke. Viscous-plastic sea ice dynamics with the evp model: linearization issues. *J. Comp. Phys.*, 170:18–38, 2001.

E. C. Hunke and J. K. Dukowicz. An elastic-viscous-plastic model for sea ice dynamics. *J. Phys. Oceanogr.*, 27:1849–1868, 1997.

M. Jakobsson, L. A. Mayer, B. Coakley, J. A. Dowdeswell, S. Forbes, B. Fridman, H. Hodnesdal, R. Noormets, R. Pedersen, M. Rebesco, H.-W. Schenke, Y. Zarayskaya, A. D. Accettella, A. Armstrong, R. M. Anderson, P. Bienhoff, A. Camerlenghi, I. Church, M. Edwards, J. V. Gardner, J. K. Hall, B. Hell, O. B. Hestvik, Y. Kristoffersen, C. Marcussen, R. Mohammad, D. Mosher, S. V. Nghiem, M. T. Pedrosa, P. G. Travaglini, and P. Weatherall. The international bathymetric chart of the arctic ocean (ibcao) version 3.0. *Geophys. Res. Lett.*, 2012. doi:10.1029/2012GL052219.

T. L. Kozo. Mountain barrier baroclinicity efects on surface winds along the alaskan arctic coast. *Geophys. Res. Lett.*, 7(5):377–380, 1980.

T. L. Kozo. An observational study of sea breezes along the alaska beaufort sea coast. *J. Appl. Meteor.*, 21:891–905, 1982a.

T. L. Kozo. A mathematical model of sea breezes along the alaska beaufort sea coast. *J. Appl. Meteor.*, 21:906–924, 1982b.

T. L. Kozo. Short term prediction (newcasting) of net daily sea ice movement in the bering strait with a mesoscale meteorological network. Technical report, U.S. Dep. of COmmer., NOAA, OCSEAP Final Rep., 1984.

W. G. Large and S. G. Yeager. The global climatology of an interannually varying air-sea flux data set. *Clim. Dyn.*, 33:341–364, 2009. DOI 10.1007/s00382-008-0441-3.

W. G. Large, J. C. McWilliams, and S. C. Doney. Oceanic vertical mixing: a review and a model with a nonlocal boundary layer parameterization. *Rev. Geophys.*, 32:363–403, 1994.

J.-F. Lemieux, B. Tremblay, F. Dupont, M. Plante, G. C. Smith, and D. Dumont. A basal stress parameterization for modeling landfast ice. *J. Geophys. Res.*, 120:3157–3173, 2015. doi:10.1002/2014JC010678.

R. W. Macdonald and E. C. Carmack. The role of large-scale under-ice topography in separating estuary and ocean on an arctic shelf. *Atmosphere-Ocean*, 29:37–51, 1991.

R. W. Macdonald, E. C. Carmack, F. A. McLaughlin, K. Iseki, D. M. Macdonald, and M. C. OBrien. Composition and modification of water masses in the mackenzie shelf estuary. *J. Geophys. Res.*, 94:18057–18070, 1989.

R. W. Macdonald, E. C. Carmack, F. A. McLaughlin, K. K. Falkner, and J. H. Swift. Composition and modification of water masses in the mackenzie shelf estuary. *Geophys. Res. Lett.*, 26(15):2223–2226, 1999.

A.R. Mahoney, H. Eicken, A.G. Gaylord, and R. Gens. Landfast sea ice extent in the chukchi and beaufort seas: The annual cycle and decadal variability. *Cold Regions Science and Technology*, 103:41–56, 2014.

P. Marchesiello, J. C. McWilliams, and A. Shchepetkin. Open boundary conditions for long-term integration of regional oceanic models. *Ocean Modelling*, 3:1–20, 2001.

J. A. Maslanik, M. C. Serreze, and T. Agnew. On the record reduction in 1998 western arctic sea-ice cover. *Geophys. Res. Lett.*, 26, 1999. doi:10.1029/1999GL900426.

G. L. Mellor and L. Kantha. An ice-ocean coupled model. *J. Geophys. Res.*, 94:10,937–10,954, 1989.

A. M. Moore, H. G. Arango, E. DiLorenzo, B. D. Cornuelle, A. J. Miller, , and D. J. Neilsen. A comprehensive ocean prediction and analysis system based on the tangent linear and adjoint of a regional ocean model. *Ocean Modelling*, 7:227–258, 2004.

D. G. Mountain, L. K. Coachman, and K. Aagaard. On the flow through barrow canyon. *J. Phys. Oceanogr.*, 6:461–470, 1976.

A. Nikolopoulos, R. S. Pickart, P. S. Fratantoni, K. Shimada, D.J. Torres, , and E. P. Jones. The western arctic boundary current at 152°w: Structure, variability, and transport. *Deep Sea Res. II*, 56:1164–1181, 2009.

R. S. Pickart. Shelfbreak circulation in the alaskan beaufort sea: Mean structure and variability. *J. Geophys. Res.*, 109, 2004. doi:10.1029/2003JC001912.

R. S. Pickart, T. J. Weingartner, S. Zimmermann, D. J. Torres, and L. J. Pratt. Flow of winter-transformed water into the western arctic. *Deep Sea Res. II*, 52:3175–3198, 2005.

M. M. Rienecker, M. J. Suarez, R. Gelaro, R. Todling, J. Bacmeister, E. Liu, M. G. Bosilovich, S. D. Schubert, L. Takacs, G.-K. Kim, S. Bloom, J. Chen, D. Collins, A. Conaty, and A. da Silva. Merra: Nasa's modern-era retrospective analysis for research and applications. *J. Climate*, 24:3624–3648, 2011. doi:10.1175/JCLI-D-11-00015.1.

A. F. Shchepetkin and J. C. McWilliams. The regional ocean modeling system (roms): A split-explicit, free-surface, topography-following coordinates oceanic model. *Ocean Modeling*, 9:347–404, 2005.

M. Steele, G. L. Mellor, and M. G. McPhee. Role of the molecular sublayer in the melting or freezing of sea ice. *J. Phys. Oceanogr.*, 19:139–147, 1989.

L. Umlauf and H. Burchard. A generic length-scale equation for geophysical turbulence models. *J. Marine Res.*, 61:235–265, 2003.

J. C. Warner, C. R. Sherwood, H. G. Arango, and R. P. Signell. Performance of four turbulence closure models implemented using a generic length scale method. *Ocean Modelling*, 8:81–113, 2005.

T. J. Weingartner, D. J. Cavalieri, K. Aagaard, and Y. Sasaki. Circulation, dense water formation, and outflow on the northeast chukchi shelf. *J. Geophys. Res.*, 103:7647–7661, 1998.

T. J. Weingartner, K. Aagaard, R. Woodgate, S. Danielson, Y. Sasaki, and D. Cavalieri. Circulation on the north central chukchi sea shelf. *Deep Sea Res. II*, 52:3150–3174, 2005.

T. J. Weingartner, S. L. Danielson, J. L. Kasper, and S. R. Okkonen. Circulation and water property variations in the nearshore alaskan beaufort sea. Final Report, OCS Study MMS 2005-028, 155pp., 2009.

T. J. Weingartner, S. L. Danielson, R. A. Potter, J. H. Trefry, A. Mahoney, M. Savoie, C. Irvine, and L. Sousa. Circulation and water properties in the landfast ice zone of the alaskan beaufort sea. *Cont. Shelf Res.*, 148:185–198, 2017. doi:10.1016/j.csr.2017.09.001. ISSN 0278-4343.

Jonathan Whitefield, Peter Winsor, James W. McClelland, and Dimitris Menemenlis. A new river discharge and river temperature climatology data set for the pan-arctic region. *Ocean Modelling*, 2015. doi:10.1016/j.ocemod.2014.12.012.

R. A. Woodgate. Increases in the pacific inflow to the arctic from 1990 to 2015, and insights into seasonal trends and driving mechanisms from year-round bering strait mooring data. *Progress in Oceanography*, 2017. doi:10.1016/j.pocean.2017.12.007.

R. A. Woodgate, K. Aagaard, and T. Weingartner. Monthly temperature, salinity, transport variability for the bering strait throughflow. *Geophys. Res. Lett.*, 32, L04601, 2005. doi:10.1029/2004GL021880.

R. A. Woodgate, T. Weingartner, and R. Lindsay. Observed increases in bering strait oceanic fluxes from the pacific to the arctic from 2001 to 2011 and their impacts on the arctic ocean water column. *Geophys. Res. Lett.*, 39, 2012. doi:10.1029/2012GL054092.

The Department of the Interior Mission

As the Nation's principal conservation agency, the Department of the Interior has responsibility for most of our nationally owned public lands and natural resources. This includes fostering the sound use of our land and water resources, protecting our fish, wildlife and biological diversity; preserving the environmental and cultural values of our national parks and historical places; and providing for the enjoyment of life through outdoor recreation. The Department assesses our energy and mineral resources and works to ensure that their development is in the best interests of all our people by encouraging stewardship and citizen participation in their care. The Department also has a major responsibility for Americal Indian reservation communities and for people who live in island communities.

The Bureau of Ocean Energy Management

The Bureau of Ocean Energy Management (BOEM) works to manage the exploration and development of the nation's offshore resources in a way that appropriately balances economic development, energy independence, and environmental protection through oil and gas leases, renewable energy development and environmental reviews and studies.

www.boem.gov